ABSTRACT

Title of Dissertation: THE LIQUID ACETONITRILE/SILICA INTERFACE: A MODEL SYSTEM FOR REINTERPRETING THE VIBRATIONAL SUM-FREQUENCY GENERATION (VSFG) SPECTRA OF LIQUID/SOLID INTERFACES

Amanda Jane Souna,
Doctor of Philosophy, 2018

Dissertation directed by: Professor John T. Fourkas, Department of Chemistry and Biochemistry

The interfacial properties of liquid acetonitrile at solid surfaces play an essential role in processes that occur in applications such as heterogeneous catalysis, chromatography, and batteries. In this thesis, the acetonitrile liquid/silica (LS) interface is used as a model system to develop a more complete approach to the interpretation of vibrational sum-frequency generation (VSFG) spectroscopy, a nonlinear optical technique that is indispensable for exploring interfacial organization and dynamics.

VSFG experiments, in combination with molecular dynamics (MD) simulations, indicate that the acetonitrile structure at this interface has properties similar to a supported lipid bilayer. In the first part of this thesis, I use this system to explore the influence of dynamics and intermolecular vibrational coupling on VSFG spectra of the methyl stretch. Time-resolved experiments examine the spectral

contribution of the more dynamic second sublayer upon introducing an IR-probe delay. The resulting spectra could not be fit with a static line shape, indicating that there is a time-dependent vibrational frequency that results from reorientation-induced spectral diffusion (RISD), a phenomenon in which molecules experience different dielectric environments as they reorient. The temperature dependence of VSFG spectra was consistent with the influence of more rapid reorientation and an earlier onset of RISD.

Close proximity and specific intermolecular configurations can allow transition dipoles to couple, allowing vibrational energy to be shared collectively between nearest neighbors via an excitonic mechanism. The influence of this coupling on VSFG spectra was quantified by performing an isotopic dilution study on the acetonitrile LS interface.

In the last part of this thesis, VSFG spectral trends are shown to predict the onset and degree of ion current rectification in electrolyte solutions in acetonitrile through glass nanopores. VSFG studies on $LiClO_4$, $LiBF_4$, $NaClO_4$, and $LiPF_6$ solutions in acetonitrile at an LS interface indicate how ions are incorporated into and modify the bilayer structure. The conclusion that charge distributions at the structured interfaces of nonaqueous electrolyte solutions cannot be interpreted using the standard models for charged interfaces will have wide-ranging applications and guide us in the interpretation of third-order contributions to VSFG spectra.

THE LIQUID ACETONITRILE/SILICA INTERFACE: A MODEL SYSTEM FOR REINTERPRETING THE VIBRATIONAL SUM-FREQUENCY GENERATION (VSFG) SPECTRA OF LIQUID/SOLID INTERFACES

by

Amanda Jane Souna

Dissertation submitted to the Faculty of the Graduate School of the
University of Maryland, College Park, in partial fulfillment
of the requirements for the degree of
Doctor of Philosophy
2018

Advisory Committee:
Professor John T. Fourkas, Chair
Professor Amy S. Mullin
Professor Zhihong Nie
Professor John D. Weeks
Professor Silvina R. Matysiak

Dedication

To my family.

Acknowledgements

There are many people I would like to thank, without whom I may never have been able to reach this point in my career.

First, I would like to thank my advisor, Prof. John Fourkas. His endless scientific knowledge and his ability to explain difficult concepts has always inspired me to work harder to become an expert myself. What I appreciate most, however, is John's supportiveness. The balance of graduate school and motherhood during the middle years of graduate school was extremely challenging, and his encouragement helped push me through this period.

I would also like to thank my committee members: Professor Amy S. Mullin, Professor Zhihong Nie, Professor John D. Weeks, and Professor Silvina R. Matysiak. I sincerely appreciate their willingness to serve on my committee and provide feedback on my thesis.

Next, I would like to thank former and current group members: Dr. Chris Rivera, Dr. Farah Dawood, Dr. Xiaoyu Sun, Dr. John Bender, Chris Hernandez, Samuel Cohen, Dan Jovinelli, Dr. Nikos Liaros, Shirl Phelps, Sandra Gutierrez Razo, Jason Tran, Matt Hourwitz, Renee Stover, Tylar Clark, and Andrea Dai. I am lucky to have had such brilliant and hardworking lab mates. I also want to thank Sandra and Matt for being such good listeners, and Sandra for her generous gifts of free babysitting. I should also include Hannah Ogden from the Mullin group as an honorary group member. I deeply appreciate her feedback on practice talks and her ideas in the laser lab. Finally, I'm grateful to Dr. Chris Rivera for being a meticulous and patient mentor on the VSFG setup.

Next, I would like to thank my family. My parents have always been patient and supportive of me throughout the twists and turns of this unusual path I have taken. I also want to thank my brother who has been tough on me, but always supportive. My son, Kamal, is one of the funniest people I know, and has been a wonderful distraction on some of the darker days of graduate school. Finally, I would like to thank my husband, Alhassan. He is the most diligent person I know, and I could not have achieved this without his hard work doing everything else, and without his faith in me.

Table of Contents

List of Tables

List of Figures

Figure 4.4. TIC of acetone left in an LDPE squirt bottle for one month. Many of the small peaks matched branched alkanes.

Figure 4.5. VSFG spectra of the silica/air interface after deposition of different solvents that had been in contact with an HDPE squirt bottle for two weeks.

Figure 4.6. VSFG spectra of the silica/air interface after deposition of different solvents after contact with the rubber bulb from a glass medicine bottle for 5 s.

Figure 4.7. VSFG spectra of the silica/air interface after deposition of acetone in contact with a rubber bulb for 5 s and 24 h.

Figure 4.8. TIC of acetone in which a rubber medicine-dropper bulb had been submerged inside for 24 hours. Mass spectral analysis of the 14.99 min peak indicates that it arises from 2,2'-methylenebis[6-(1,1-dimethylethyl)-4-ethyl-phenol]. Although the presence of this species in the liquid does not necessarily signify presence in the residue, and its IR spectrum does not distinguish it from other organic components,[17] the large size of this molecules suggests that it would remain on the silica surface rather than evaporating.

Figure 4.9. VSFG spectra of the silica/air interface after deposition of acetone and methanol left in contact with (A) LDPE and (B) rubber. Solid lines show signal of residue after the surface dried, and dashed lines show signal after the sample is left sitting for one day.

Figure 4.10. VSFG spectra of the silica/air interface after deposition of acetone and methanol left in contact with the rubber bulb from a medicine dropper vs. pouring the solvent directly on the surface.

Figure 5.1. The dependence of the IR transition dipole and the isotropic and anisotropic portions of the polarizability tensor on the instantaneous direction of a resonant IR field for a totally symmetric vibrational mode as a function of initial orientation. The plots of the changes in dipole and polarizability are not on the same scale as the other plots. In the plots of changes in the portions of polarizability tensor, red denotes a negative change and black denotes a positive change.

Figure 5.2. Schematic depiction of interfacial molecules with a totally symmetric vibrational mode at the initial time that a vibrational coherence is created (a) and after the molecular orientations have randomized completely via orientational diffusion (b). Red groups initially pointed toward the interface, blue groups initially pointed away from the interface, and white groups initially pointed roughly parallel to the interface. See text for a discussion of the molecules labeled 1 through 4.

Figure 5.3. (a) Orientational distribution of methyl groups in the second sublayer of acetonitrile at the LS interface based on the simulations of Hu and Weeks, ref. 33. (b) Distribution of vibrational coherences created by a *P*-polarized excitation pulse. Red

Figure 8.6. VSFG peak intensities of four electrolyte solutions in acetonitrile relative to the peak intensity of neat acetonitrile. The dotted line indicates the peak intensity of dry acetonitrile. The dashed line indicates the peak intensity of acetonitrile that was briefly exposed to ambient air while filling the sample cuvette. The electrolyte solutions were similarly exposed to ambient air, so relative intensity points are normalized to the wet acetonitrile.

Figure 8.7. FWHM for VSFG spectra of four electrolyte solutions in acetonitrile. The black dashed line indicates the FWHM of neat acetonitrile. The FWHM does not change significantly when dry acetonitrile is exposed to ambient water.

Figure 8.8. Shift in peak frequency for VSFG spectra of electrolyte solutions relative to neat acetonitrile. The peak frequency does not change significantly when dry acetonitrile is exposed to ambient water.

Figure 8.9. Acetonitrile charge density at a silica interface as calculated by Hu and Weeks in Reference 13. The charge density generated by the surface silicon, oxygen, and hydrogen atoms is shown in the inset. Within 1 Å of the silica surface the charge density is dominated by the partial charges on the surface atoms in the silica. Because the surface has no net charge, the charge density of the acetonitrile becomes more important at distances greater than 1 Å.

Figure 8.10. Cartoons of the organization of acetonitrile at the silica interface in different concentration regimes of lithium perchlorate: (A) neat acetonitrile (B) very low concentration ($\leq 10^{-6}$ M) (C) low concentration (10^{-6} M $\leq$ concentration $\leq 10^{-3}$ M) (D) intermediate concentration (10^{-3} M $\leq$ concentration $\leq 10^{-2}$ M) (E) high concentration ($\geq 10^{-2}$).

List of Abbreviations

BB	Broadband
EDL	Electrical double layer
FID	Free induction decay
FWHM	Full width at half maximum
GC-EI-MS	Gas chromatography-electron ionization-mass spectrometry
HDPE	High-density polyethylene
HILIC	Hydrophilic interaction chromatography
IR	Infrared
LBL	Lipid bilayer-like
LDPE	Low-density polyethylene
LS	Liquid/silica
MD	Molecular dynamics
NDFG	Noncollinear difference frequency generation
NRB	Non-resonant background
OKE	Optical Kerr effect
OPA	Optical parametric amplifier
RISD	Reorientation-induced spectral diffusion
RNCE	Raman noncoincidence effect
SAP	Surface-associated potential
SFG	Sum-frequency generation
TCF	Time correlation function
TIC	Total ion chromatogram

VSFG	Vibrational sum-frequency generation

Chapter 1: Introduction

1.1 Background

Vibrational sum-frequency generation (VSFG) spectroscopy was first described theoretically by Bloembergen and Pershan in the 1960s,[1] and the first successful experiments were performed by Shen's group in the late 1980s.[2-3] This technique has become an indispensable tool for exploring the molecular organization, interactions, and dynamics that occur at interfaces. This thesis explores new methods of interpreting VSFG spectra, based on experiments performed using liquid acetonitrile, CH_3CN at a fused silica interface as a model system. This system offers an opportunity to develop a more complete method of analysis that examines not only molecular organization, but also reorientational dynamics, energy transfer, and the influence of an electric potential. With these new tools for interpreting spectra, we can develop a detailed picture of systems of great practical importance for applications such as separations, nanofluidics, and energy storage.

In a VSFG experiment, a mid-infrared (IR) laser beam and a visible, or near-infrared, probe laser beam are overlapped spatially and temporally at a sample, generating a signal with a photon energy equal to the sum of the photon energies of the two incident beams. The signal becomes resonantly enhanced when the mid-IR beam can drive a dipole-allowed vibrational transition. Sum-frequency generation (SFG) is a second-order nonlinear optical process. Therefore, under the electric dipole approximation, SFG is forbidden in media with inversion symmetry, including isotropic bulk media. At the interface between two isotropic media, however, inversion symmetry is broken. VSFG is therefore a surface-sensitive technique, capable of

probing a region that is only one or a few molecular layers thick, even as this region is surrounded by far more numerous bulk molecules. By controlling the polarization of the incident and signal beams, information can be obtained regarding the average orientation of molecules at the surface.

VSFG spectroscopy can be used to study any interface at which centrosymmetry is broken, including liquid/solid, gas/solid, liquid/vapor and liquid/liquid interfaces. This thesis will focus on liquid/solid interfaces. The importance of understanding liquid/solid interfaces can be seen from the ubiquity of applications that involve such systems, such as heterogeneous catalysis, lubrication, environmental chemistry, and separations.[4-8] Buried liquid interfaces are difficult to study experimentally because they require high sensitivity and specificity, as well as nonvacuum conditions.[9] Scanning tunneling microscopy and atomic force microscopy meet these criteria, but they can only be used on thin films of liquids on a solid surface, and necessarily apply a force to the system. Other techniques that can be used to study surfaces have large probing depths. X-ray spectroscopy and neutron reflectivity measure regions greater than 1 nm thick, and attenuated total reflection and total internal reflection FTIR spectroscopies measure regions thicker than 100 nm.[10]

A number of different implementations have been used for VSFG spectroscopy. The mid-IR source can be broadband or narrowband. With the advent of reliable ultrafast laser sources, broadband IR pulses have made spectral acquisition much more rapid, eliminating the need to scan through IR wavelengths.[11] The probe source can be continuous-wave or pulsed. Typical probe pulses for frequency-domain experiments are either several picoseconds or more in length (narrowband), or tens to hundreds of

femtoseconds (for time-domain experiments). The superior spectral resolution of the former is required when vibrational modes are closely spaced.[12] Time-domain VSFG, also known as free-induction-decay (FID) VSFG, can better resolve inhomogeneous broadening and provide insight into time-dependent processes.[13] Experimental geometries include either the co- or counter-propagation of incident beams, and the detection of either the reflected or transmitted signal.[14] Reflection geometries are more common, although transmission geometries are useful when the refractive indices of the two adjacent media are similar,[15] or when there is interference generated by charged interfaces.[16] More advanced approaches include heterodyne-detected (phase-sensitive) measurements,[17] or employ more than two incident beams, such as in pump-SFG-probe experiments.[18] The research that comprises this thesis was performed with a homodyne, broadband-IR, narrowband-probe, counter-propagating implementation.[19] The probe pulses are long enough to achieve high-resolution spectra but short enough, relative to the length of the sample's vibrational response, to gather information in the time domain.[20]

One strength of VSFG spectroscopy lies in its capability of determining molecular organization and orientation. However, VSFG spectra are influenced by a variety of factors besides orientation, several of which will be considered in this thesis. Reorientation, intermolecular vibrational coupling, and the presence of an electric field are all factors that can complicate conventional orientational analysis. Orientational motion, such as tumbling and internal rotation, of small molecules in the liquid phase can occur in picoseconds or less, which is on the same time scale as both the vibrational dephasing time and the probing time of the measurement.[21-22] The sensitivity of VSFG

to reorientation depends on the polarization configuration used, the vibrational mode being probed, and the timing of the incident pulses.[23] Symmetric modes tend to be dominated by an isotropic polarizability, and thus have less sensitivity to reorientation.[23-25] There are some situations, however, in which even highly isotropic modes are sensitive to reorientation. In a process known as reorientation-induced spectral diffusion (RISD), vibrational frequencies can become time-dependent when molecules reorient such that oscillators enter a different dielectric environment.[20, 26-28]

Energy transfer, which can include intra- or intermolecular transfer, can occur between molecules in close proximity, especially molecules with large transition dipole moments that can undergo transition dipole-transition dipole coupling.[29-33] In Förster vibrational energy transfer, energy can hop between oscillators, acting as a dephasing mechanism and potentially mimicking the effects of reorientation.[25] In some cases, the interfacial geometry can induce a strong enough coupling that, rather than an energy transfer between molecules, the excitation is shared coherently over multiple molecules.[25] These vibrational excitonic effects cause VSFG spectra to change in ways that depend on the specific molecular configurations at the interface. One manifestation of excitonic coupling is known as the Raman noncoincidence effect (RNCE), which induces a shift between the first moments of the IR, isotropic Raman, and anisotropic Raman spectra. The RNCE has been detected in linear Raman measurements,[34-36] but the influence of such coupling on VSFG spectra is just beginning to be investigated.[25]

Another factor that can have a dramatic influence on VSFG spectra is the presence of an electric field at or near a surface. This scenario is ubiquitous, yet its effects are poorly understood. To date, the majority of the work on charged interfaces

has involved aqueous systems, exploring topics such as pH and salt concentration effects at a silica interface[37-42] and at a liquid/vapor interface populated with charged surfactants.[43] For the silica case, silanol groups become deprotonated, and negatively charged, in aqueous solutions. Therefore, for both the liquid water/silica and the water/surfactant/vapor interface, the charged surface introduces a third, DC electric field, which may generate a third-order ($\chi^{(3)}$) response.[42, 44-47] There are two parts of this third-order contribution. One part is generated by molecules oriented by the electric field (and therefore having an induced anisotropy). There is also an isotropic contribution from the purely third-order susceptibility of the bulk molecules.[16, 41, 45-47] The total VSFG signal in aqueous systems is influenced both by the interference between photons generated at different depths and the presence of dissolved ions that shield molecules in the bulk from the DC field.[16] The dependence of VSFG spectra of nonaqueous liquids on local charge distribution is relatively unexplored, but based on the results described in Chapter Eight, the theory that describes aqueous interfaces may not be appropriate for organic liquids.

In seeking to make better interpretations of VSFG spectra and to contribute to the characterization of an interface of great practical importance, I chose to examine liquid acetonitrile at a silica interface. In many ways, this system is an ideal model for exploring these phenomena. Acetonitrile is a small, relatively simple molecule with amphiphilic character, and has an organization at the silica interface that has been studied in great detail with experiments[48-54] and simulations.[54-58] Acetonitrile also has wide applications as a solvent in heterogeneous catalysis[59-60] and chromatographic separations.[6] As a good solvent for many electrolytes, acetonitrile is a representative

liquid that can be used to improve our understanding of electrochemical systems. Acetonitrile's low viscosity makes it well-suited for studying dynamics as well.

Acetonitrile at the silica interface has a completely different organization than in the bulk liquid. In the bulk, acetonitrile's cyano groups have some tendency for antiparallel dipole pairing.[61-65] However, its properties have been reproduced successfully with a model that does not include attractive interactions,[66] and another model finds that an antiparallel methyl-methyl pairing dominates.[67] Some degree of antiparallel ordering is suggested by a dielectric constant that is lower than would be predicted based on acetonitrile's sizable dipole moment (3.92 D).[68-70] In contrast, at the silica interface, acetonitrile organizes itself into a structure reminiscent of a lipid bilayer.[54-58] The cyano groups accept hydrogen bonds from the surface silanol groups, forming a well-ordered first sublayer. The second sublayer orients with the methyl groups directed toward the nonpolar environment created by the methyl groups of the first sublayer. However, this sublayer has a broader orientational distribution, with methyl groups directed in both directions.

Insight into the driving forces underlying this organization can be gained from molecular dynamics (MD) simulations. For example, simulations of acetonitrile in silica pores show that the formation of the first sublayer can be driven by electrostatic interactions when hydrogen bonds are not present.[55, 58] Similarly, when hydrogen-bonding interactions are turned off while maintaining the same electrostatic interactions, the rate of reorientation is unchanged.[58] Simulations also indicate the existence of two populations, a bulk-like core population and a surface-associated population.[55] Correlation times are calculated effectively with this two-state model that

includes exchange between populations.[55] In the case of nanoporous silica, confinement also contributes to slower dynamics. Acetonitrile in pores functionalized with nonpolar groups reorients more slowly than in the bulk, but more rapidly than in hydrophilic pores. [71] However, a lipid bilayer-like (LBL) structure also exists at a flat surface, where MD simulations show that the bilayer structure repeats for up to 20 Å.[56]

There is also a large body of experimental work in agreement with the LBL picture. One of the first experiments was an NMR study on liquid acetonitrile in nanoporous silica that found that smaller pores have slower overall dynamics.[51] Because NMR observes dynamics on a time scale longer than that of reorientation, these data were interpreted by taking an average of two populations: one population with a bulk-like spin-lattice relaxation time, and the other with faster spin-lattice relaxational dynamics.[51] Optical Kerr effect (OKE) spectroscopy is an ultrafast pump-probe technique that induces a transient birefringence with a pump pulse and then probes over a timescale of picoseconds, revealing orientational dynamics.[72] In agreement with the NMR results, collective orientation times are dependent on the pore size of nanoporous silica sol gels, and can also be explained with a two-state, or core-shell model.[48, 73-74] For OKE, the time scale of the surface relaxation is slower than the exchange rate between the two populations, and therefore exchange must be included in this interpretation. Indeed, OKE decays could be fit to three exponentials with decay times that include a short, bulk-like reorientation time, a long, surface-like reorientation time, and an intermediate time associated with molecules beginning in the surface population and exchanging with the core population.[48, 73]

Vibrational spectroscopy can also be used to infer the presence of more than one population of acetonitrile molecules due to the sensitivity of vibrational modes to their local environments. The C≡N stretching mode is particularly sensitive to its environment.[75] The nitrogen accepts hydrogen bonds in an end-on configuration, resulting in a withdrawal of electron density from an antibonding molecular orbital. This redistribution causes a shortening and strengthening of the C≡N bond, and a significant blue shift in the IR spectrum.[58, 76] The appearance of a second, red-shifted peak in isotropic Raman[52] and FTIR[50, 53] studies of porous silica in which acetonitrile is undergoing capillary condensation is attributed to a growing number of bulk-like molecules that are not associated with the surface. A VSFG study of acetonitrile/water mixtures looking at the C≡N stretch shows a blue shift attributed to the formation of hydrogen bonds with water, and shows an abrupt structural change at high mole fractions of water.[77] The methyl symmetric stretch is also sensitive to its environment, but to a lesser extent. Using Raman difference spectroscopy, Kitigawa *et al* detected a 4 cm^{-1} blue shift for the symmetric methyl stretch in bulk acetonitrile/water mixtures at infinite dilution.[78] VSFG studies show a smaller blue shift in acetonitrile/water mixtures at the liquid/vapor[79] and liquid/silica interfaces. [80]

VSFG studies of the acetonitrile/silica interface have been interpreted in a manner that is consistent with previous simulations and experiments. Most work is in agreement that the cyano group is oriented toward the silica surface,[54, 81] as well as toward other oxides such as zirconia and alumina,[82] with a large projection of its transition dipole along the surface normal. Results from an early VSFG study by our group are in closer alignment with the LBL picture.[54] Interestingly, the signal generated

from this surface is substantial, which is surprising given that an LBL organization would be nearly centrosymmetric. This result was explained by the fact that the second sublayer is slightly less populated and much more disordered than the first sublayer. In addition, the cyano groups of the first sublayer are hydrogen bonded, which is expected to shift the methyl symmetric stretch frequency slightly. Therefore, the two sublayers have different center frequencies, which shifts their contributions apart and reduces cancellation.[54] More recently, we have started to consider the influence of a $\chi^{(3)}$ contribution, which can be sizable even in centrosymmetric environments.

With detailed knowledge of this interfacial system, we have been able to probe many of the phenomena that influence VSFG spectra. At first, acetonitrile may appear to be a poor candidate for studying dynamics, because molecules in the first sublayer have dynamics that are slower than the time scale of the measurement. Also, the methyl symmetric stretch is a highly isotropic mode, and measurements of isotropic modes using the more common polarization configurations are in some ways insensitive to reorientation.[23] The second sublayer, however, has dynamics that more closely resemble the bulk, with reorientation times of a few picoseconds.[55] In addition, molecules in the second sublayer are in an inhomogeneous environment, with their methyl groups residing either in the nonpolar interior of the bilayer, or in the more polar bulk region. This inhomogeneity, combined with bulk-like dynamics, make molecules in the second sublayer good subjects for studying RISD. I probed the effects of RISD by introducing a delay between the IR and the probe pulses,[20] which is discussed in Chapter Five, and by varying temperature,[83] which influences the reorientational rate, and is discussed in Chapter Six.

In Chapter Seven, I describe our study on the influence of intermolecular resonance coupling on the VSFG spectrum of the acetonitrile/silica interface. Although the transition dipole strength of the methyl symmetric stretch is relatively small (0.05-0.3 × 10^{-30} C-m),[84-87] because acetonitrile molecules are closely aligned, and methyl groups are closely spaced, we may expect to see evidence of intermolecular vibrational coupling. I probed this coupling by diluting acetonitrile with its deuterated isotopologue, which increases the separation between CH_3 groups.

An electric field can increase a signal substantially by inducing a third-order response, and can induce shifts in vibrational frequency and line shape. However, this influence is poorly understood, especially for nonaqueous systems. In Chapter Eight, I discuss the use of the methyl symmetric stretch as a probe of both the acetonitrile organization and the concentration of ions at the surface in electrolyte/acetonitrile solutions. I consider the relevance of not only the surface potential, but the potential that originates from the solvent itself because of the arrangement of partial charges within the bilayer. This intrinsic potential of the bilayer not only influences where ions are driven to reside, but can induce a third-order VSFG contribution that cannot be described with the models used to interpret the third-order response of water at charged interfaces.

With these improved tools for interpreting VSFG spectra, we can gain a deeper understanding of the mechanisms that occur in many applications. One such application is hydrophilic interaction chromatography (HILIC). This technique commonly uses mixtures of acetonitrile and water as a mobile phase, and bare silica as a stationary phase, to separate small, polar analytes. The mechanism of retention is not fully

understood, but is thought to involve the partitioning of polar molecules into a water-rich layer adjacent to the silica surface, whereas molecules elute in the more acetonitrile-rich mobile phase.[6] MD simulations show that in water/acetonitrile mixtures water forms a dense, somewhat immobile, monolayer that forms hydrogen bonds with silanol groups, and a water-rich layer exists out to 1.5 nm.[68, 88] Interestingly, however, both simulations[57] and VSFG experiments[80] suggest that patches of the LBL structure of acetonitrile remain even at acetonitrile mole fractions as low as 0.1. Evaluating the influence of a bilayer at a silica stationary phase should be invaluable to the development of this type of chromatography.

In electrochemical and catalytic applications, it is desirable for the acetonitrile to be anhydrous. However, acetonitrile is highly hygroscopic and requires careful drying and storage. Based on simulations of moderately low concentrations of water in acetonitrile, we may imagine that water would form a monolayer even at very low concentrations. Once a monolayer is formed, acetonitrile can accept hydrogen bonds from water as easily as from silanol groups, and water may even increase the concentration of hydrogen bond donors. Because silica becomes deprotonated in an aqueous environment, residual water may also introduce a surface potential and a third-order response. Although it is not feasible to study very low concentrations of water with MD simulations, VSFG is well-suited to explore the influence of residual water on the interfacial structure of acetonitrile. The results of such experiments are discussed in Chapter Eight.

In Chapter Eight, I also discuss VSFG studies on electrolyte solutions in acetonitrile at a silica interface. It is critical to understand this system to understand

electrochemical processes that occur at an interface, particularly in applications where surface interactions dominate, such as nanofluidics and energy storage.[89] To develop a better understanding of the charge transport properties at surfaces typical of lithium ion batteries, which typically include lithium salts in aprotic solvents, acetonitrile can serve as a representative system. The conventional theory on the distribution of ions at surfaces uses an electrical double layer (EDL) model that includes an immobile Stern layer with an exponential decrease in potential in the diffuse layer, the length of which depends on the degree of screening from ions.[90] I will discuss in Chapter Eight that the VSFG spectra measured in solutions of electrolytes in acetonitrile are inconsistent with the EDL model. We will discuss the implications not only for the VSFG community, but for any group interested in understanding how an electrostatic potential is modified near a surface in the presence of a structured nonaqueous liquid.

1.2 Outline

The work described in this thesis has two goals. The first is to improve the fundamental interpretation of VSFG spectroscopy. The second is to develop practical insights into the acetonitrile/silica interface specifically, and nonaqueous solvents at polar interfaces in general, for applications such as separations, heterogeneous catalysis, nanofluidics, and energy storage.

The outline of this thesis is as follows:

- Chapter Two: The theory of VSFG spectroscopy is described. Fundamental theory, non-time-coincident transitions, and modeling of the instrumental and molecular responses will be discussed.

- Chapter Three: The counter-propagating broadband VSFG spectrometer employed for all experiments presented in this thesis is discussed.
- Chapter Four: The importance of proper storage of solvents used to clean optics is discussed. Methanol, acetone, and isopropanol left in contact with low- or high-density polyethylene plastic and rubber were investigated, and VSFG spectra of fused silica flats contaminated with solvent residue are presented.
- Chapter Five: Reorientation-induced spectral diffusion (RISD) of the methyl symmetric stretch of acetonitrile at the silica interface is investigated by introducing a delay between the IR and probe pulses. Simulated spectra are used to analyze trends that occur as acetonitrile reorients, assuming a range of shifts in center frequency from 1 to 6 cm^{-1}. VSFG spectra are presented with a delay between 0 and 3.5 ps and fits that account for the instrument response. A static line shape cannot reproduce the spectra, which is attributed to the influence of RISD.
- Chapter Six: The temperature dependence of the liquid acetonitrile/silica interface is investigated from 25 °C to 60 °C. VSFG spectra show a blue shift and decreased intensity with an increase in temperature. The lower intensity at higher temperature is attributed to greater disorder in the first sublayer. Also, the second sublayer reorients more rapidly, which causes the blue shift due to earlier onset of RISD.
- Chapter Seven: An isotopic dilution study of acetonitrile at the silica interface is performed to examine the influence of intermolecular vibrational coupling on VSFG spectra of the methyl symmetric stretch. The spectra exhibit a blue shift,

a decrease in linewidth, and an intensity higher than expected based on the number of oscillators with dilution. Isotropic Raman, IR, and anisotropic Raman shifts are evaluated for five different relative configurations of two acetonitrile molecules.[36] The shifts qualitatively describe both Raman and FTIR experiments of bulk acetonitrile and the present VSFG spectra.

- Chapter Eight: Electrolyte solutions in acetonitrile with concentrations ranging over 10 orders of magnitude at the silica interface are investigated. Electrolytes commonly used in lithium ion batteries with high solubility in acetonitrile were selected, including lithium perchlorate, lithium tetrafluoroborate and lithium hexafluorophosphate. Sodium perchlorate was also examined to identify the influence of the type of cation. VSFG spectra were compared to the results from ion transport experiments through glass pipettes using the same concentrations of electrolyte solutions. VSFG spectral trends could be used to predict the onset of ion current rectification through nanopores, which is an effect that arises from a surface charge on nanopore walls. Therefore, VSFG can pinpoint the distribution of ions at an acetonitrile/silica interface as surface charge develops.
- Chapter Nine: Conclusions and future work.

1.3 References

1. Bloembergen, N.; Pershan, P. S., Light waves at the boundary of nonlinear media *Phys. Rev.* **1962,** *128* (2), 606-&.

2. Hunt, J. H.; Guyotsionnest, P.; Shen, Y. R., Observation of C-H stretch vibrations of monolayers of molecules. Optical sum-frequency generation. *Chem. Phys. Lett.* **1987,** *133* (3), 189-192.

3. Zhu, X. D.; Suhr, H.; Shen, Y. R., Surface vibrational spectroscopy by infrared-visible sum frequency generation *Phys. Rev. B* **1987,** *35* (6), 3047-3050.

4. Shultz, M. J.; Schnitzer, C.; Simonelli, D.; Baldelli, S., Sum frequency generation spectroscopy of the aqueous interface: ionic and soluble molecular solutions. *Int. Rev. Phys. Chem.* **2000,** *19* (1), 123-153.

5. Richmond, G. L., Molecular bonding and interactions at aqueous surfaces as probed by vibrational sum frequency spectroscopy. *Chem. Rev.* **2002,** *102* (8), 2693-2724.

6. Hemström, P.; Irgum, K., Hydrophilic interaction chromatography. *J. Sep. Sci.* **2006,** *29* (12), 1784-1821.

7. Schofer, J.; Rehbein, P.; Stolz, U.; Lohe, D.; Zum Gahr, K. H., Formation of tribochemical films and white layers on self-mated bearing steel surfaces in boundary lubricated sliding contact. *Wear* **2001,** *248* (1-2), 7-15.

8. Geiger, F. M., Second harmonic generation, sum frequency generation, and $\chi^{(3)}$: Dissecting environmental interfaces with a nonlinear optical Swiss army knife. *Annu. Rev. Phys. Chem.* **2009,** *60*, 61-83.

9. Buck, M.; Himmelhaus, M., Vibrational spectroscopy of interfaces by infrared-visible sum frequency generation. *J. Vac. Sci. Technol. A* **2001,** *19* (6), 2717-2736.

10. Shen, Y. R.; Ostroverkhov, V., Sum-frequency vibrational spectroscopy on water interfaces: Polar orientation of water molecules at interfaces. *Chem. Rev.* **2006,** *106* (4), 1140-1154.

11. Richter, L. J.; Petralli-Mallow, T. P.; Stephenson, J. C., Vibrationally resolved sum-frequency generation with broad-bandwidth infrared pulses. *Opt. Lett.* **1998,** *23* (20), 1594-1596.

12. Wang, H. F.; Velarde, L.; Gan, W.; Fu, L., Quantitative sum-frequency generation vibrational spectroscopy of molecular surfaces and interfaces: lineshape, polarization, and orientation. *Annu. Rev. Phys. Chem.* **2015,** *66*, 189-216.

13. Bonn, M.; Ueba, H.; Wolf, M., Theory of sum-frequency generation spectroscopy of adsorbed molecules using the density matrix method—broadband vibrational sum-frequency generation and applications. *J. Phys.-Condens. Mat.* **2005,** *17*, S201-S220.

14. Dick, B.; Gierulski, A.; Marowsky, G.; Reider, G. A., Determination of the nonlinear optical susceptibility $\chi^{(2)}$ of surface layers by sum and difference frequency generation in reflection and transmission. *Appl. Phys. B-Photo.* **1985,** *38* (2), 107-116.

15. Messmer, M. C.; Conboy, J. C.; Richmond, G. L., Observation of molecular ordering at the liquid-liquid interface by resonant sum-frequency generation. *J. Am. Chem. Soc.* **1995,** *117* (30), 8039-8040.

16. Gonella, G.; Lütgebaucks, C.; de Beer, A. G. F.; Roke, S., Second harmonic and sum-frequency generation from aqueous interfaces is modulated by interference. *J. Phys. Chem. C* **2016,** *120* (17), 9165-9173.

17. Shen, Y. R., Phase-sensitive sum-frequency spectroscopy. *Annu. Rev. Phys. Chem.* **2013,** *64*, 129-50.

18. Ghosh, A.; Smits, M.; Bredenbeck, J.; Dijkhuizen, N.; Bonn, M., Femtosecond time-resolved and two-dimensional vibrational sum frequency spectroscopic

instrumentation to study structural dynamics at interfaces. *Rev. Sci. Instrum.* **2008,** *79* (9).

19. Ding, F.; Zhong, Q.; Brindza, M. R.; Fourkas, J. T.; Walker, R. A., Ti:sapphire, broadband vibrational sum-frequency generation spectrometer with a counter-propagating geometry. *Optics Exp.* **2009,** *17*, 14665-75.

20. Rivera, C. A.; Souna, A. J.; Bender, J. S.; Manfred, K.; Fourkas, J. T., Reorientation-induced spectral diffusion in vibrational sum-frequency-generation spectroscopy. *J. Phys. Chem. B* **2013,** *117* (49), 15875-85.

21. Vinaykin, M.; Benderskii, A. V., Orientational dynamics in sum frequency spectroscopic line shapes. *J. Phys. Chem. B* **2013,** *117* (49), 15833-15842.

22. Wei, X.; Shen, Y. R., Motional effect in surface sum-frequency vibrational spectroscopy. *Phys. Rev. Lett.* **2001,** *86*, 4799-4802.

23. Fourkas, J. T.; Walker, R. A.; Can, S. Z.; Gershgoren, E., Effects of reorientation in vibrational sum-frequency spectroscopy. *J. Phys. Chem. C* **2007,** *111*, 8902-8915.

24. Liu, S. L.; Fourkas, J. T., Orientational time correlation functions for vibrational sum-frequency generation. 1. Acetonitrile. *J. Phys. Chem. A* **2013,** *117* (29), 5853-5864.

25. Rivera, C. A.; Fourkas, J. T., Reexamining the interpretation of vibrational sum-frequency generation spectra. *Int. Rev. Phys. Chem.* **2011,** *30* (4), 409-443.

26. Steel, W. H.; Walker, R. A., Measuring dipolar width across liquid-liquid interfaces with 'molecular rulers'. *Nature* **2003,** *424* (6946), 296-299.

27. Stein, A. D.; Fayer, M. D., Spectral diffusion in liquids. *J. Chem. Phys.* **1992,** *97* (5), 2948-2962.

28. Fenn, E. E.; Wong, D. B.; Giammanco, C. H.; Fayer, M. D., Dynamics of water at the interface in reverse micelles: Measurements of spectral diffusion with two-dimensional infrared vibrational echoes. *J. Phys. Chem. B* **2011,** *115* (40), 11658-11670.

29. Smit, W. J.; Versluis, J.; Backus, E. H. G.; Bonn, M.; Bakker, H. J., Reduced near-resonant vibrational coupling at the surfaces of liquid water and ice. *J. Phys. Chem. Lett.* **2018,** *9* (6), 1290-1294.

30. Schaefer, J.; Backus, E. H. G.; Nagata, Y.; Bonn, M., Both inter- and intramolecular coupling of O-H groups determine the vibrational response of the water/air interface. *J. Phys. Chem. Lett.* **2016,** *7* (22), 4591-4595.

31. Yamamoto, S.; Ghosh, A.; Nienhuys, H. K.; Bonn, M., Ultrafast inter- and intramolecular vibrational energy transfer between molecules at interfaces studied by time- and polarization-resolved SFG spectroscopy. *Phys. Chem. Chem. Phys.* **2010,** *12* (40), 12909-12918.

32. Bonn, M.; Hess, C.; Wolf, M., The dynamics of vibrational excitations on surfaces: CO on Ru(001). *J. Chem. Phys.* **2001,** *115* (16), 7725-7735.

33. Woutersen, S.; Bakker, H. J., Resonant intermolecular transfer of vibrational energy in liquid water. *Nature* **1999,** *402* (6761), 507-509.

34. Giorgini, M. G.; Torii, H.; Musso, M., The influence of alkaline earth ions on the structural organization of acetone probed by the noncoincidence effect of the

ν(C=O) band: experimental and quantum chemical results. *Phys. Chem. Chem. Phys.* **2010,** *12* (1), 183-192.

35. Giorgini, M. G.; Torii, H.; Musso, M.; Venditti, G., Influence of ions on the structural organization of dipolar liquids probed by the noncoincidence effect: Experimental and quantum chemical results. *J. Phys. Chem. B* **2008,** *112* (25), 7506-7514.

36. Giorgini, M. G., Raman noncoincidence effect: A spectroscopic manifestation of the intermolecular vibrational coupling in dipolar molecular liquids. *Pure Appl. Chem.* **2004,** *76* (1), 157-169.

37. Rehl, B.; Li, Z. G.; Gibbs, J. M., Influence of high pH on the organization of acetonitrile at the silica/water interface studied by sum frequency generation spectroscopy. *Langmuir* **2018,** *34* (15), 4445-4454.

38. Lis, D.; Backus, E. H. G.; Hunger, J.; Parekh, S. H.; Bonn, M., Liquid flow along a solid surface reversibly alters interfacial chemistry. *Science* **2014,** *344* (6188), 1138-1142.

39. Miranda, P. B.; Shen, Y. R., Liquid Interfaces : A Study by Sum-Frequency Vibrational Spectroscopy. *J. Phys. Chem. B* **1999,** *103*, 3292-3307.

40. Schaefer, J.; Backus, E. H. G.; Bonn, M., Evidence for auto-catalytic mineral dissolution from surface-specific vibrational spectroscopy. *Nat. Commun.* **2018,** *9*.

41. Jena, K. C.; Covert, P. A.; Hore, D. K., The effect of salt on the water structure at a charged solid surface: differentiating second- and third-order nonlinear contributions. *J. Phys. Chem. Lett.* **2011,** *2* (9), 1056-1061.

42. Schaefer, J.; Gonella, G.; Bonn, M.; Backus, E. H. G., Surface-specific vibrational spectroscopy of the water/silica interface: screening and interference. *Phys. Chem. Chem. Phys.* **2017,** *19* (25), 16875-16880.

43. Gragson, D. E.; Richmond, G. L., Investigations of the structure and hydrogen bonding of water molecules at liquid surfaces by vibrational sum frequency spectroscopy. *J. Phys. Chem. B* **1998,** *102*, 366-375.

44. Eisenthal, K. B., Liquid interfaces probed by second-harmonic and sum-frequency spectroscopy. *Chem. Rev.* **1996,** *96* (4), 1343-1360.

45. Ohno, P. E.; Wang, H. F.; Geiger, F. M., Second-order spectral lineshapes from charged interfaces. *Nat. Commun.* **2017,** *8*.

46. Pezzotti, S.; Galimberti, D. R.; Shen, Y. R.; Gaigeot, M. P., Structural definition of the BIL and DL: a new universal methodology to rationalize non-linear $\chi^{(2)}(\omega)$ SFG signals at charged interfaces, including $\chi^{(3)}(\omega)$ contributions. *Phys. Chem. Chem. Phys.* **2018,** *20* (7), 5190-5199.

47. Wen, Y. C.; Zha, S.; Liu, X.; Yang, S. S.; Guo, P.; Shi, G. S.; Fang, H. P.; Shen, Y. R.; Tian, C. S., Unveiling microscopic structures of charged water interfaces by surface-specific vibrational spectroscopy. *Phys. Rev. Lett.* **2016,** *116* (1).

48. Loughnane, B. J.; Farrer, R. A.; Scodinu, A.; Fourkas, J. T., Dynamics of a wetting liquid in nanopores: An optical Kerr effect study of the dynamics of acetonitrile confined in sol-gel glasses. *J. Chem. Phys.* **1999,** *111* (11), 5116-5123.

49. Loughnane, B. J.; Scodinu, A.; Farrer, R. A.; Fourkas, J. T.; Mohanty, U., Exponential intermolecular dynamics in optical Kerr effect spectroscopy of small-molecule liquids. *J. Chem. Phys.* **1999,** *111* (6), 2686.

50. Kittaka, S.; Iwashita, T.; Serizawa, A.; Kranishi, M.; Takahara, S.; Kuroda, Y.; Mori, T.; Yamaguchi, T., Low temperature properties of acetonitrile confined in MCM-41. *J. Phys. Chem. B* **2005,** *109* (49), 23162-23169.

51. Zhang, J.; Jonas, J., NMR study of the geometry confinement effects on the anisotropic rotational diffusion of acetonitrile-d3. *J. Phys. Chem.* **1993,** *97* (34), 8812-8815.

52. Nikiel, L.; Hopkins, B.; Zerda, T. W., Rotational and vibrational relaxation of small molecules in porous silica-gels. *J. Phys. Chem.* **1990,** *94* (19), 7458-7464.

53. Tanaka, H.; Iiyama, T.; Uekawa, N.; Suzuki, T.; Matsumoto, A.; Grun, M.; Unger, K. K.; Kaneko, K., Molecular mechanism of capillary condensation of acetonitrile vapor on MCM-41 with the aid of a time-correlation function analysis of IR spectroscopy. *Chem. Phys. Lett.* **1998,** *293* (5-6), 541-546.

54. Ding, F.; Hu, Z.; Zhong, Q.; Manfred, K.; Gattass, R. R.; Brindza, M. R.; Fourkas, J. T.; Walker, R. A.; Weeks, J. D., Interfacial organization of acetonitrile: simulation and experiment. *J. Phys. Chem. C* **2010,** *114* (41), 17651-17659.

55. Cheng, L.; Morrone, J. A.; Berne, B. J., Structure and dynamics of acetonitrile confined in a silica nanopore. *J. Phys. Chem. C* **2012,** *116* (17), 9582-9593.

56. Hu, Z.; Weeks, J. D., Acetonitrile on silica surfaces and at its liquid-vapor interface: structural correlations and collective dynamics. *J. Phys. Chem. C* **2010,** *114* (22), 10202-10211.

57. Mountain, R. D., Molecular dynamics simulation of water-acetonitrile mixtures in a silica slit. *J. Phys. Chem. C* **2013,** *117* (8), 3923-3929.

58. Morales, C. M.; Thompson, W. H., Simulations of infrared spectra of nanoconfined liquids: Acetonitrile confined in nanoscale, hydrophilic silica pores. *J. Phys. Chem. A* **2009,** *113* (10), 1922-1933.

59. Hidalgo-Acosta, J. C.; Scanlon, M. D.; Mendez, M. A.; Peljo, P.; Opallo, M.; Girault, H. H., Enhanced reactivity of water clusters towards oxidation in water/acetonitrile mixtures. *Chemelectrochem* **2016,** *3* (12), 2003-2007.

60. Hidalgo-Acosta, J. C.; Mendez, M. A.; Scanlon, M. D.; Vrubel, H.; Amstutz, V.; Adamiak, W.; Opallo, M.; Girault, H. H., Catalysis of water oxidation in acetonitrile by iridium oxide nanoparticles. *Chem. Sci.* **2015,** *6* (3), 1761-1769.

61. Saito, H.; Tanaka, Y.; Nagata, S.; Nukada, K., C-13 nuclear magnetic resonance studies on molecular association .1. Self-association of dipolar molecules. *Can. J. Chem.* **1973,** *51* (13), 2118-2123.

62. Gorbunova, T. V.; Batalin, G. I., Problem of structure of liquid aliphatic nitriles *J. Struct. Chem.* **1976,** *17* (3), 392-395.

63. Kratochwill, A.; Weidner, J. U.; Zimmermann, H., Investigation of X-ray structure of liquid acetonitrile *Phys. Chem. Chem. Phys.* **1973,** *77* (6), 408-425.

64. Bertagnolli, H.; Zeidler, M. D., Molecular pair correlation function of liquid acetonitrile from x-ray and neutron diffraction studies. *Mol. Phys.* **1978,** *35* (1), 177-192.

65. Bertagnolli, H.; Chieux, P.; Zeidler, M. D., Neutron diffraction study of liquid acetonitrile. 2. $CD_3C^{15}N$. *Mol. Phys.* **1976,** *32* (6), 1731-1736.

66. Hsu, C. S.; Chandler, D., RISM calculation of structure of liquid acetonitrile. *Mol. Phys.* **1978,** *36* (1), 215-224.

67. Pothoczki, S.; Pusztai, L., Intermolecular orientations in liquid acetonitrile: New insights based on diffraction measurements and all-atom simulations. *J. Mol. Liq.* **2017,** *225*, 160-166.

68. Melnikov, S. M.; Holtzel, A.; Seidel-Morgenstern, A.; Tallarek, U., Adsorption of water-acetonitrile mixtures to model silica surfaces. *J. Phys. Chem. C* **2013,** *117* (13), 6620-6631.

69. Jadzyn, J.; Swiergiel, J., On intermolecular dipolar coupling in two strongly polar liquids: dimethyl sulfoxide and acetonitrile. *J. Phys. Chem. B* **2011,** *115* (20), 6623-6628.

70. Srinivasan, K. R.; Kay, R. L., Pressure dependence of dielectric constant and density of acetonitrile at 3 temperatures. *J. Solution Chem.* **1977,** *6* (5), 357-367.

71. Norton, C. D.; Thompson, W. H., Reorientation dynamics of nanoconfined acetonitrile: A critical examination of two-state models. *J. Phys. Chem. B* **2014,** *118* (28), 8227-8235.

72. Zhong, Q.; Fourkas, J. T., Optical Kerr effect spectroscopy of simple liquids. *J. Phys. Chem. B* **2008,** *112* (49), 15529-15539.

73. Loughnane, B. J.; Farrer, R. A.; Fourkas, J. T., Evidence for the direct observation of molecular exchange of a liquid at the solid/liquid interface. *J. Phys. Chem. B* **1998,** *102* (28), 5409-5412.

74. Farrer, R. A.; Fourkas, J. T., Orientational dynamics of liquids confined in nanoporous sol-gel glasses studied by optical Kerr effect spectroscopy. *Accounts Chem. Res.* **2003,** *36* (8), 605-612.

75. Barthel, J.; Buchner, R.; Wismeth, E., FTIR spectroscopy of ion solvation of $LiClO_4$ and LiSCN in acetonitrile, benzonitrile, and propylene carbonate. *J. Solution Chem.* **2000,** *29* (10), 937-954.

76. Fawcett, W. R.; Liu, G.; Kessler, T. E., Solvent-induced frequency shifts in the infrared spectrum of acetonitrile in organic solvents. *J. Phys. Chem.* **1993,** *97* (37), 9293-9298.

77. Zhang, D.; Gutow, J. H.; Eisenthal, K. B.; Heinz, T. F., Sudden structural change at an air/binary liquid interface: Sum-frequency study of the air/acetonitrile-water interface. *J. Chem. Phys.* **1993,** *98* (6), 5099-5101.

78. Kamogawa, K.; Kitagawa, T., Raman difference spectroscopy of the C-H stretching vibrations- Frequency shifts and excess quantities for acetone/water and acetonitrile/water solutions. *J. Phys. Chem.* **1986,** *90* (6), 1077-1081.

79. Kim, J.; Chou, K. C.; Somorjai, G. A., Structure and dynamics of acetonitrile at the air/liquid interface of binary solutions studied by infrared-visible sum frequency generation. *J. Phys. Chem. B* **2003,** *107* (7), 1592-1596.

80. Rivera, C. A.; Bender, J. S.; Manfred, K.; Fourkas, J. T., Persistence of acetonitrile bilayers at the interface of acetonitrile/water mixtures with silica. *J. Phys. Chem. A* **2013,** *117* (46), 12060-6.

81. Henry, M. C.; Piagessi, E. A.; Zesotarski, J. C.; Messmer, M. C., Sum-frequency observation of solvent structure at model chromatographic interfaces: Acetonitrile-water and methanol-water systems. *Langmuir* **2005,** *21* (14), 6521-6526.

82. Strunk, M. R.; Williams, C. T., Aliphatic nitrile adsorption on Al_2O_3 and ZrO_2 as studied by total internal reflection sum-frequency spectroscopy. *Langmuir* **2003,** *19* (22), 9210-9215.

83. Souna, A. J.; Clark, T. L.; Fourkas, J. T., Effect of temperature on the organization of acetonitrile at the silica/liquid interface. *J. Phys. Chem. C* **2017,** *121* (47), 26432-26437.

84. Bertie, J. E.; Apelblat, Y.; Keefe, C. D., Infrared intensities of liquids XXV: Dielectric constants, molar polarizabilities and integrated intensities of liquid toluene at 25 °C between 4800 and 400 cm^{-1}. *J. Mol. Struct.* **2005,** *750* (1-3), 78-93.

85. Biliškov, N., Infrared optical constants, molar absorption coefficients, dielectric constants, molar polarisabilities, transition moments and dipole moment derivatives of liquid N,N-dimethylacetamide-carbon tetrachloride mixtures. *Spectrochim. Acta A Mol. Biomol. Spectrosc.* **2011,** *79* (2), 295-301.

86. Biliškov, N., Infrared optical constants, molar absorption coefficients, dielectric constants, molar polarisabilities, transition moments and dipole moment derivatives of liquid N,N-dimethylformamide-carbon tetrachloride mixtures. *Spectrochim. Acta A Mol. Biomol. Spectrosc.* **2011,** *79* (2), 302-307.

87. Keefe, C. D.; Pickup, J. E., Infrared optical constants, dielectric constants, molar polarizabilities, transition moments, dipole moment derivatives and Raman spectrum of liquid cyclohexane. *Spectrochim. Acta A Mol. Biomol. Spectrosc.* **2009,** *72* (5), 947-953.

88. Melnikov, S. M.; Holtzel, A.; Seidel-Morgenstern, A.; Tallarek, U., Composition, structure, and mobility of water-acetonitrile mixtures in a silica nanopore studied by molecular dynamics simulations. *Anal. Chem.* **2011,** *83* (7), 2569-2575.

89. Plett, T.; Shi, W. Q.; Zeng, Y. H.; Mann, W.; Vlassiouk, I.; Baker, L. A.; Siwy, Z. S., Rectification of nanopores in aprotic solvents - transport properties of nanopores with surface dipoles. *Nanoscale* **2015,** *7* (45), 19080-19091.

90. Schoch, R. B.; Han, J.; Renaud, P., Transport phenomena in nanofluidics. *Rev. Mod. Phys.* **2008,** *80* (3), 839-883.

Chapter 2: Theory

2.1 Introduction to Vibrational Sum-Frequency Generation Theory

Sum-frequency generation (SFG) is a second-order, nonlinear optical process in which a material interacts with two different electric fields, typically from intense laser pulses, to generate a polarization with a frequency component that is at the sum of the two input frequencies. If one or more of the incident fields is tuned to a vibrational or an electronic transition of the sample, SFG becomes resonantly enhanced. In vibrational sum frequency generation (VSFG) spectroscopy a mid-infrared (IR) laser pulse creates a vibrational coherence in a sample. A nonresonant visible, or near-IR, pulse then upconverts the coherence via a Raman transition (Figure 2.1). The probed molecule must therefore be both IR and Raman active, so in theory it must lack a center of inversion. The surface specificity is because, under the electric dipole approximation, a second-order nonlinear optical response is forbidden in media with inversion symmetry. However, an SFG

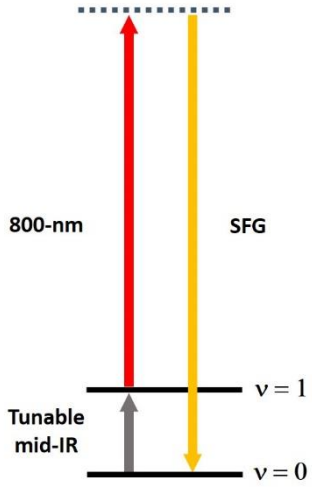

Figure 2.1 Energy diagram for a VSFG process. ν = 0 represents the ground vibrational state, ν = 1 represents the first excited vibrational state, and the dashed line represents a virtual energy state.

response can be generated at an interface where centrosymmetry is broken. Bulk contributions can be neglected unless the bulk structure is either non-centrosymmetric or has a sizable magnetic dipole or quadrupole response.[1-4]

The sum-frequency signal is generated at a phase-matched angle according to the conservation of momentum equation[1]

$$\omega_{sig} \sin\theta_{sig} = -\omega_{IR} \sin\theta_{IR} - \omega_{probe} \sin\theta_{probe}, \quad (2.1)$$

where ω_{sig}, ω_{IR}, and ω_{probe} are the frequencies of the signal, IR, and probe beams respectively, and θ_i is the angle with respect to the surface normal for the beam with frequency ω_i. θ_i is defined as negative when to the left of the surface normal and positive when to the right. The experimental geometry is depicted in Figure 2.2.

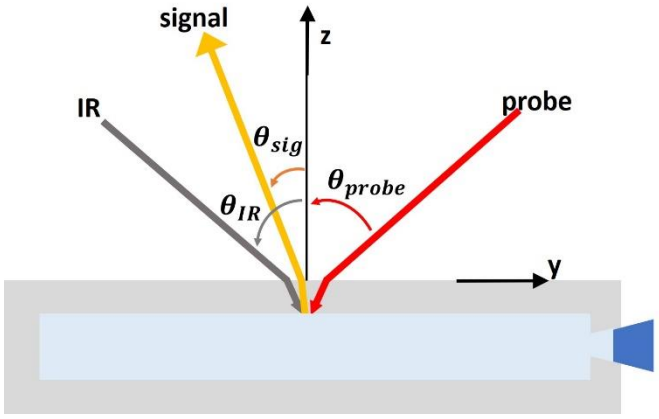

Figure 2.2 VSFG experimental geometry in a counter-propagating configuration.

The intensity of the signal is given by[5-6]

$$I_{sig} = \frac{8\pi^2 \omega_{sig}^2 sec^2(\theta_{sig})}{c^3 n_{sig} n_{probe} n_{IR}} \left|\chi_{eff}^{(2)}\right|^2 I_{probe} I_{IR}, \quad (2.2)$$

where n_i and I_i are the refractive index and intensity of the beam with frequency ω_i, c is the speed of light, and $\chi_{eff}^{(2)}$ is the effective second-order nonlinear susceptibility.

$\chi_{eff}^{(2)}$ is a linear combination of tensor elements of $\chi_{ijk}^{(2)}$, which is a third-rank tensor with the indices representing each electric field in reverse temporal order, and each index having an *x*, *y*, and *z* component in the laboratory frame. In the case of an azimuthally symmetric interface, only seven of the 27 tensor elements are nonzero, four of which are unique: $\chi_{yyz}^{(2)} = \chi_{xxz}^{(2)}$, $\chi_{yzy}^{(2)} = \chi_{xzx}^{(2)}$, $\chi_{zyy}^{(2)} = \chi_{zxx}^{(2)}$, and $\chi_{zzz}^{(2)}$. Therefore, the general expression for $\chi_{eff}^{(2)}$ at an azimuthally symmetric interface is a linear combination of seven tensor elements:[1]

$$\begin{aligned}
\chi_{eff}^{(2)} = {} & sin\Omega_{sig} sin\Omega_{probe} cos\Omega_{IR} L_{xx}(\omega_{sig}) L_{xx}(\omega_{probe}) L_{zz}(\omega_{IR}) sin\,\theta_{IR} \\
& + sin\Omega_{sig} cos\Omega_{probe} sin\Omega_{IR} L_{xx}(\omega_{sig}) L_{zz}(\omega_{probe}) L_{xx}(\omega_{IR}) sin\,\theta_{probe} \chi_{xzx}^{(2)} \\
& + cos\Omega_{sig} sin\Omega_{probe} sin\Omega_{IR} L_{zz}(\omega_{sig}) L_{xx}(\omega_{probe}) L_{xx}(\omega_{IR}) sin\,\theta_{sig} \chi_{zxx}^{(2)} \\
& - cos\Omega_{sig} cos\Omega_{probe} cos\Omega_{IR} L_{yy}(\omega_{sig}) L_{yy}(\omega_{probe}) L_{zz}(\omega_{IR}) cos\,\theta_{sig} cos\,\theta_{probe} sin\,\theta_{IR}\, \chi_{yyz}^{(2)} \\
& + cos\Omega_{sig} cos\Omega_{probe} cos\Omega_{IR} L_{yy}(\omega_{sig}) L_{zz}(\omega_{probe}) L_{yy}(\omega_{IR}) cos\,\theta_{sig} sin\,\theta_{probe} cos\,\theta_{IR} \chi_{yzy}^{(2)} \\
& - cos\Omega_{sig} cos\Omega_{probe} cos\Omega_{IR} L_{zz}(\omega_{sig}) L_{yy}(\omega_{probe}) L_{yy}(\omega_{IR}) sin\,\theta_{sig} cos\,\theta_{probe} cos\,\theta_{IR} \chi_{zyy}^{(2)} \\
& + cos\Omega_{sig} cos\Omega_{probe} cos\Omega_{IR} L_{zz}(\omega_{sig}) L_{zz}(\omega_{probe}) L_{zz}(\omega_{IR}) sin\,\theta_{sig} sin\,\theta_{probe} sin\,\theta_{IR} \chi_{zzz}^{(2)}, \quad (2.3)
\end{aligned}$$

where Ω_i is the angle of polarization and the L_{ii} are nonlinear Fresnel factors. Fresnel factors correct for differences between the incident light and the electric fields at the surface, as well as the difference between the electric field generated in the immediate environment of the interfacial molecules and the emitted signal. Fresnel factors are described in detail in Section 2.2.1.

For experiments in which light is polarized either parallel, *P*, or perpendicular, *S*, to the plane of incidence and reflection, the seven terms reduce further to those shown in equations 2.4-2.7. The only possible polarization configurations are those in which *P* occurs an odd number of times:[1]

$$\chi^{(2)}_{eff,SSP} = L_{xx}(\omega_{sig})L_{xx}(\omega_{probe})L_{zz}(\omega_{IR})sin\,\theta_{IR}\chi^{(2)}_{xxz} \quad (2.4)$$

$$\chi^{(2)}_{eff,SPS} = L_{xx}(\omega_{sig})L_{zz}(\omega_{probe})L_{xx}(\omega_{IR})sin\,\theta_{probe}\chi^{(2)}_{xzx} \quad (2.5)$$

$$\chi^{(2)}_{eff,PSS} = L_{zz}(\omega_{sig})L_{xx}(\omega_{probe})L_{xx}(\omega_{IR})sin\,\theta_{sig}\chi^{(2)}_{zxx} \quad (2.6)$$

and

$$\begin{aligned}\chi^{(2)}_{eff,PPP} = {} & L_{yy}(\omega_{sig})L_{yy}(\omega_{probe})L_{zz}(\omega_{IR})cos\,\theta_{sig}cos\,\theta_{probe}sin\,\theta_{IR}\,\chi^{(2)}_{yyz} \\ & + L_{yy}(\omega_{sig})L_{zz}(\omega_{probe})L_{yy}(\omega_{IR})cos\,\theta_{sig}sin\,\theta_{probe}cos\,\theta_{IR}\chi^{(2)}_{yzy} \\ & + L_{zz}(\omega_{sig})L_{yy}(\omega_{probe})L_{yy}(\omega_{IR})sin\,\theta_{sig}cos\,\theta_{probe}cos\,\theta_{IR}\chi^{(2)}_{zyy} \\ & + L_{zz}(\omega_{sig})L_{zz}(\omega_{probe})L_{zz}(\omega_{IR})sin\,\theta_{sig}sin\,\theta_{probe}sin\,\theta_{IR}\chi^{(2)}_{zzz}\,. \quad (2.7)\end{aligned}$$

The *SSP* polarization configuration is sensitive to vibrational modes that have a transition dipole moment with a projection along the surface normal, whereas the *SPS* configuration is sensitive to modes that have a transition dipole moment with a projection along the surface. The *PPP* configuration is sensitive to modes with transition dipole moments in both orientations. Because the *PPP* configuration is sensitive to four different tensor elements, and because the $\chi^{(2)}_{yyz}$ and the $\chi^{(2)}_{zzz}$ terms are typically of opposite sign, *PPP* data can be challenging to interpret. However, the sensitivity of the *PPP* signal to the experimental geometry enables the adjustment of incident angles to provide information about $\chi^{(2)}_{ijk}$.

2.2 Orientational Analysis

The strength of the $\chi^{(2)}$ response reveals information about the molecular number density and organization via[7]

$$\chi^{(2)}_{ijk} \propto N \sum_{i'j'k'} \langle R_{ii'} R_{jj'} R_{kk'} \rangle \beta^{(2)}_{i'j'k'}, \quad (2.8)$$

where N is the number density of oscillators, $\beta_{i'j'k'}$ is the hyperpolarizability tensor, and the brackets designate an orientational average with $R_{ii'}$ representing an element of the Euler transformation matrix

$$r = \begin{bmatrix} \cos\theta\cos\varphi\cos\chi - \sin\varphi\sin\chi & \cos\theta\sin\varphi\cos\chi + \cos\varphi\sin\chi & \sin\theta\cos\chi \\ -\cos\theta\cos\varphi\sin\chi - \sin\varphi\cos\chi & -\cos\theta\sin\varphi\sin\chi + \cos\varphi\cos\chi & -\sin\theta\sin\chi \\ -\sin\theta\cos\varphi & -\sin\theta\sin\varphi & \cos\theta \end{bmatrix}, \qquad (2.9)$$

which transforms coordinates from the molecular frame to the laboratory frame (see Figure 2.3). $\beta_{i'j'k'}$ depends on the infrared transition dipole moment, μ', and the polarizability tensor, α'. When the IR and probe interactions are not simultaneous, μ' and α' must be considered separately, as described in Section 2.3.

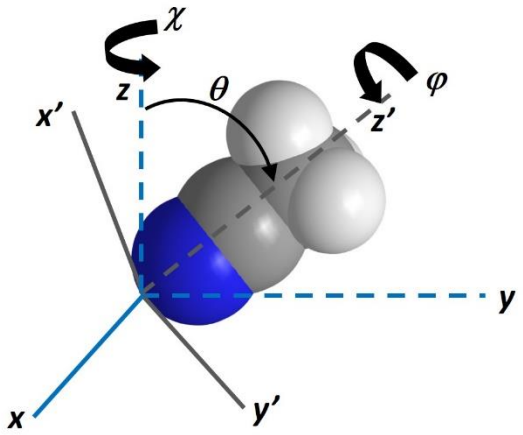

Figure 2.3 Axis system in the laboratory frame (x, y, z) and molecular frame (x', y', z') and the necessary angles (θ, χ, ϕ) required to transform between coordinates.

The strategy for VSFG orientational analysis is first to obtain values for different tensor elements of $\chi^{(2)}_{ijk}$ by measuring $\chi^{(2)}_{eff}$ under different polarization configurations or experimental geometries, and then to calculate $\chi^{(2)}_{ijk}$ using estimated values for the Fresnel factors. Then, expressions for orientational averages, using equation 2.8, can be evaluated using measured or calculated values for μ' and α'. The

appropriate distribution of orientations will need to be assessed, and may be represented, for instance, by a delta function, a Gaussian function, or another distribution.[7] Finally, the different expressions can be combined to solve for the average orientation. There are many methods for performing this analysis, including the polarization null angle method and the polarization intensity ratio method.[7,8] All of these methods involve comparing the relative strength of selected $\chi_{ijk}^{(2)}$ tensor elements.

2.2.1 Fresnel Factors

To calculate the necessary $\chi_{ijk}^{(2)}$ elements accurately, knowledge of the nonlinear Fresnel factors is needed. The Fresnel factors, L_{ii}, are given by

$$L_{xx}(\omega_i) = \frac{2n_1(\omega_i)\cos\beta_i}{n_1(\omega_i)\cos\beta_i + n_2(\omega_i)\cos\gamma_i} \tag{2.10}$$

$$L_{yy}(\omega_i) = \frac{n_1(\omega_i)\cos\gamma_i}{n_1(\omega_i)\cos\gamma_i + n_2(\omega_i)\cos\beta_i} \tag{2.11}$$

and

$$L_{zz}(\omega_i) = \frac{2n_2(\omega_i)\cos\beta_i}{n_1(\omega_i)\cos\gamma_i + n_2(\omega_i)\cos\beta_i}\left(\frac{n_1(\omega_i)}{n'(\omega_i)}\right)^2, \tag{2.12}$$

where n_1 and n_2 are the refractive indices of the first and second media with which the incident beams interact and n' is the refractive index of the interface. β_i is the angle of incidence of the beam with frequency ω_i, and γ_i is the refractive angle into the second medium, where

$$n_1(\omega_i)\sin\beta_i = n_2(\omega_i)\sin\gamma_i. \tag{2.13}$$

There are two areas of uncertainty when attempting to determine Fresnel factors accurately. The first, and most challenging problem, is assessing n', the refractive index of the interface, which can be significantly different from bulk values of the two media.

An interfacial refractive index is dependent on the anisotropy of dielectric properties, and therefore on both the molecular polarizability and organization.[7] Some researchers use an average between the refractive indices of the two adjacent media, the higher refractive index of the two, or another method.[9] In work by Shen and coworkers, the refractive index of the second medium is used, but a local field factor correction is applied.[5, 10]

The second challenge is obtaining refractive indices at mid-IR frequencies, which are difficult to measure when close to resonance. This challenge becomes less problematic for co-propagating setups, because the terms containing $n(\omega_{IR})$ largely cancel out for the equations relevant to this geometry.[7] However, for counter-propagating systems, careful assessment of $n(\omega_{IR})$ is necessary for quantitative orientational analysis. One benefit of this scenario is that a comparison of co-propagating and counter-propagating spectra could potentially be used to deduce the IR refractive index. [7]

2.2.2 Evaluation of hyperpolarizability, β_{ijk}

To evaluate equation 2.8, knowledge of the hyperpolarizability, $\beta_{i'j'k'}$, is required. $\beta_{i'j'k'}$ depends on μ' and α', which can be obtained with spectroscopic measurements or calculations. It is often convenient to work with the isotropic and anisotropic portions of the Raman tensor, α_I and α_I, which are the rotationally invariant isotropic and anisotropic polarizabilities[1]

$$\alpha'_I = \frac{1}{3} Tr\{\boldsymbol{\alpha}'\} \tag{2.14}$$

where $\boldsymbol{\alpha}'$ is the polarizability tensor, and

$$\alpha'_A = \sqrt{\frac{1}{2}(\alpha'_{xx} - \alpha'_{yy})^2 + \frac{1}{2}(\alpha'_{xx} - \alpha'_{zz})^2 + \frac{1}{2}(\alpha'_{yy} - \alpha'_{zz})^2} \qquad (2.15)$$

For cylindrically symmetric functional groups these expressions reduce to

$$\alpha'_I = \frac{1}{3}(2\alpha'_{xx} + \alpha'_{zz}) \qquad (2.16)$$

and

$$\alpha'_A = \alpha'_{xx} - \alpha'_{zz}. \qquad (2.17)$$

The relative signs and strengths of α_I and α_A can often be estimated by using the Raman depolarization ratio, which is an experimentally derived quantity taken from polarized Raman measurements. Typically, the ratio between α_I and α_A from the Raman depolarization ratio is consistent with two possible solutions. VSFG can help determine which solution is correct by identifying the relative sign between $\chi^{(2)}_{xxz}$ and $\chi^{(2)}_{zzz}$. This determination can be made by manipulating the polarization axes of the incident beams, and measuring the intensity of a selected polarization of the signal, as demonstrated by Zhang *et al*.[11] Alternatively, phase-sensitive VSFG measurements can be performed. Other means of obtaining information about $\beta_{i'j'k'}$ include *ab initio* calculations and bond-polarizability-derivative models.[2, 7, 12-13]

2.2.3 Orientational analysis of cylindrically symmetrical molecules

The methyl group of acetonitrile is freely rotating, so the symmetric methyl stretch can be classified as having cylindrical symmetry. For this class of vibrational moiety, the angular average for $\chi^{(2)}_{xxz}$, the tensor element detected with the *SSP* polarization configuration, reduces to[14]

$$\chi^{(2)}_{xxz} \propto \mu'_z \left(\alpha'_I - \frac{1}{6}\alpha'_A\right)\langle\cos\theta\rangle + \frac{1}{2}\mu'_z\alpha'_A\langle\cos^3\theta\rangle \qquad (2.18)$$

The methyl symmetric stretch has a strong IR transition[15] that is directed along the molecular (*z*) axis, so μ'_z is large. The Raman strength is also significant, and α_I is approximately three times the magnitude and of the same sign as α_A, based on the symmetric methyl stretch of a long-chain amphiphile.[11] As a result, an *SSP* VSFG signal generated from acetonitrile at a silica interface is strong. In contrast, the *SPS* signal is extremely weak for this mode, so ratios between different tensor elements are difficult to obtain and quantitative orientational analysis is unreliable. However, equation 2.18 can be used to examine acetonitrile's orientational dependence on various experimental conditions, such as temperature or chemical environment.

The asymmetric methyl stretch also has a strong IR transition, but a weak Raman transition.[15] In part, because of the orientation of the transition dipole of this completely depolarized mode at the silica interface, it is present in *SPS* and *PPP* spectra, but is undetectable in the *SSP* polarization configuration. *SPS* signals can be compared under different experimental conditions with the expression[9]

$$\chi^{(2)}_{xzx} \propto \frac{1}{2}\left(\mu'_x \alpha'_{xz} + \mu'_y \alpha'_{yz}\right)\langle\cos^3\theta\rangle \qquad (2.19)$$

The *PPP* spectrum is sensitive to both the symmetric and asymmetric methyl stretches. The first and last term dominate for the symmetric stretch; the first term contains $\chi^{(2)}_{xxz}$, expressed in equation 2.18, and the last term contains $\chi^{(2)}_{zzz}$:

$$\chi^{(2)}_{zzz} \propto \mu'_z\left(\alpha'_I + \frac{1}{3}\alpha'_A\right)\langle\cos\theta\rangle - \mu'_z\alpha'_A\langle\cos^3\theta\rangle\,. \qquad (2.20)$$

Because these terms are opposite in sign in the counter-propagating geometry, the isotropic terms of 2.18 and 2.20 partially cancel out. Therefore, the *PPP* configuration emphasizes the anisotropic portion of the polarizability tensor.[1] For acetonitrile,

however, *PPP* spectra tend to exhibit trends that are similar to *SSP* spectra for the symmetric stretch and similar to *SPS* spectra for the asymmetric stretch.

2.3 Non-time-coincident transitions

The expressions describing the second-order susceptibility that have been presented thus far are valid when the IR and Raman transitions occur simultaneously. In time-domain VSFG experiments, there are certain conditions in which it is preferable for there to be a short delay (on the order of a few picoseconds) between the IR and probe pulses. Liquids that have relatively low viscosity, such as acetonitrile, may reorient (spin or tumble) on a time scale that is similar to that of other dephasing mechanisms. Therefore, when attempting to extract orientational information from these experiments, it is essential to modify the expressions for $\chi_{ijk}^{(2)}$ for non-simultaneous transitions.

There are several aspects to consider when determining the influence of dynamics on VSFG signal intensity: the vibrational mode, the polarization configuration, the axis about which the molecule reorients, and the local environment of the molecule.[1, 16-20] In equation 2.8, $\chi_{ijk}^{(2)}$ was described as being proportional to an orientational average of the hyperpolarizability, $\beta^{(2)}$. This expression can be modified by expressing $\chi_{ijk}^{(2)}$ in the time domain as $R_{ijk}^{(2)}(\tau)$, and separating the hyperpolarizability into dipole and polarizability derivatives, μ' and α':[18]

$$R_{ijk}^{(2)}(\tau) \propto \langle (\sum_{\beta=1}^{3} R_{\beta,k}(0)\mu'_{\beta})(\sum_{\gamma=1}^{3}\sum_{\delta=1}^{3} R_{\gamma,i}(\tau)R_{\delta,j}(\tau)\alpha'_{\gamma\delta})\rangle, \qquad (2.21)$$

where τ is equal to the time delay between the creation and the probing of the coherence.

2.3.1 Non-time-coincident transitions: symmetric methyl stretch

As in equations 2.18-2.20, when performing an orientational average using equation 2.21, the number of terms can be reduced for highly symmetric molecules or moieties. For the methyl symmetric stretch, $R^{(2)}_{xxz}$ (the element probed under the *SSP* configuration) becomes[18]

$$R^{(2)}_{xxz}(\tau) \propto \mu'_Z \alpha'_I \langle \cos\theta \rangle + \mu'_Z \alpha'_A \left(\frac{1}{12} \langle \cos\theta \rangle + \frac{1}{4} \langle \cos\theta \cos 2\Theta \rangle \right), \tag{2.22}$$

where lowercase Greek letters designate angles at time zero, and uppercase Greek letters designate angles at a later time, τ. Only the terms with orientational averages containing angles at both times will be sensitive to reorientation. These orientational averages are a form of time correlation function (TCF), and can be evaluated with molecular dynamics (MD) simulations. According to equation 2.22, the last term of $R^{(2)}_{xxz}(\tau)$, which depends on the anisotropic polarizability derivative, α'_A, is orientationally sensitive to the tumbling motion in θ. However, for polarized modes such as the symmetric methyl stretch, the isotropic portion of the polarizability dominates, so *SSP* measurements are largely insensitive to reorientation. (A phenomenon that occurs if reorientation also changes the vibrational frequency of an oscillator by changing the local environment will be discussed in Chapter Five.)

SPS measurements of the same class of vibrational mode depend on $R^{(2)}_{xzx}$:

$$R^{(2)}_{xzx}(\tau) \propto -\frac{1}{2} \mu'_Z \alpha'_A \langle \sin\theta \sin 2\Theta \cos\chi \cos \mathrm{X} \rangle. \tag{2.23}$$

This configuration depends only on the anisotropic portion of the polarizability, so *SPS* measurements of the symmetric stretch are nearly undetectable, despite a moderate projection onto the surface plane.

PPP measurements include $R^{(2)}_{zzz}(\tau)$:

$$R^{(2)}_{zzz}(\tau) \propto \mu'_Z\alpha'_l\langle\cos\theta\rangle - \mu'_Z\alpha'_A\left(\frac{1}{6}\langle\cos\theta\rangle + \frac{1}{2}\langle\cos\theta\cos 2\Theta\rangle\right). \quad (2.24)$$

Like $R^{(2)}_{xxz}$ in equation 2.22, $R^{(2)}_{zzz}$ has one term that is sensitive to reorientation in θ. Because *PPP* measurements depend on a weighted difference of $R^{(2)}_{xxz}$ and $R^{(2)}_{zzz}$, they emphasize the anisotropic portion of the Raman polarizability, and therefore are somewhat more sensitive to reorientation than are *SSP* measurements.

2.3.2 Non-time coincident transitions: asymmetric methyl stretch

When delay-dependent orientational averages are performed for the case of an asymmetric methyl stretch, equivalent expressions for the tensor elements shown in equations 2.22-2.24 are dependent on methyl rotation (spinning). For acetonitrile, the methyl group is a free rotor, so these response functions decay to zero on the time scale of the probing step. Therefore, all polarization configurations are sensitive to spinning for the case of the asymmetric methyl stretch.[18]

2.3.3 Environmental influence on reorientation

MD simulations help clarify the influence of environment on the reorientation dependence of VSFG measurements. For example, the P_1 ($\cos\theta$) orientational correlation time of acetonitrile is 3.4 ps in the bulk, 1.9 ps at the liquid acetonitrile/vapor interface, and 24 ps at the liquid acetonitrile/silica interface.[21] This

trend is reflected in VSFG measurements in different interfacial systems. For example, the TCF $\langle \cos\theta \cos 2\Theta \rangle$ that influences *SSP* and *PPP* measurements of the symmetric methyl stretch is shown in Figure 2.4 for different systems. At the liquid/vapor interface, the TCF shows that the system reaches equilibrium in 6 ps, which is on the same time scale as vibrational dephasing. In contrast, at the liquid/silica interface, the dynamics are hindered, and reorientation occurs on a much longer time scale. For more depolarized modes, environmentally-sensitive reorientation becomes an essential consideration.

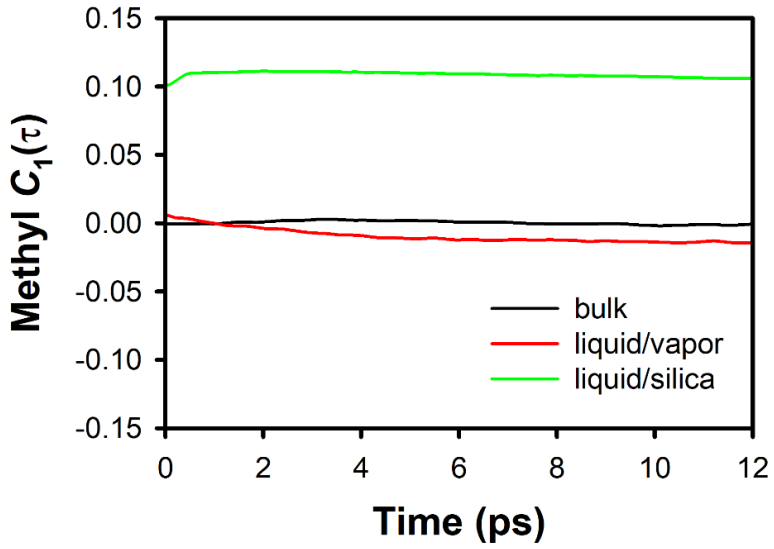

Figure 2.4 Time correlation function, C_1, equivalent to $\langle \cos\theta \cos 2\Theta \rangle$, for acetonitrile in different environments. C_1 influences the $R^{(2)}_{xxz}$ and $R^{(2)}_{zzz}$ tensors measured in *SSP* and *PPP* measurements of the symmetric methyl stretch shown in equations 2.22 and 2.24. Figure is from reference (18).

2.4 Accurate determination of the molecular response

The underlying process that we probe in a VSFG experiment is the vibrational coherence, known as the molecular response, of molecules excited by the IR pulse. In

the frequency domain, the molecular response is typically represented by a sum of Lorentzian functions:

$$\chi^{(2)}(\omega) \propto \sum_k \frac{A_k}{(\omega-\omega_k)+i\Gamma_k}, \tag{2.25}$$

where *k* signifies either a specific vibrational mode or a subset of molecules with the same vibrational mode but different environments, A_k is the amplitude of each contribution and depends on the number of oscillators, orientation, and Fresnel factors as described above, ω_k is the center frequency, and Γ_k is the linewidth of Lorentzian contribution, *k*. The VSFG signal intensity is proportional to the magnitude squared of this sum. Often there is not a unique fit, so inferences are made to determine starting parameters. For example, for acetonitrile, two oppositely oriented sublayers would suggest that spectra composed of two oppositely phased peaks with different, but closely spaced, vibrational frequencies.

With the use of equation 2.25, there is the assumption that the molecular response is best represented by Lorentzian functions, which describe line shapes exhibiting homogeneous broadening. For the case in which the molecular response is inhomogeneously broadened, the spectrum may be better described by a Voigt function, which is a Lorentzian function convolved with a Gaussian function.[22] However, in most cases, Lorentzian functions are a good approximation, and experiments that compare broadband (BB)-SFG (frequency domain) and free-induction decay (FID)-SFG (time domain) spectra show that inhomogeneous broadening detected in FID-SFG often is not apparent in BB-SFG fits.[23-24]

2.4.1 Nonresonant contribution, $\chi_{\mathrm{NR}}^{(2)}$

It is important to mention that equation 2.25 omits any nonresonant SFG contribution. When fitting VSFG spectra, the nonresonant contribution is represented as a constant and inserted into equation 2.25:

$$\chi^{(2)}(\omega) = \chi_{NR}^{(2)} + \chi_{R}^{(2)} \propto \chi_{NR}^{(2)} + \sum_k \frac{A_k}{(\omega - \omega_k) + i\Gamma_k} \tag{2.26}$$

The challenge in assessing the nonresonant contribution is assigning a phase, which can be either in phase with the resonant response, out of phase with the resonant response, or something in between. Because the VSFG intensity is proportional to the magnitude squared of $\chi^{(2)}$, knowing both the magnitude and phase is essential. The nonresonant component depends on the polarizability of molecules, and tends to be relatively small in most liquids but large in metals.[2] However, for buried interfaces, a nonresonant signal is generated from a quadrupole response that can originate from the bulk in any region in which the IR and probe beams propagate together. Therefore, the nonresonant contribution is usually negligible with a counter-propagating geometry because the proximity between the IR and probe is minimized.[25]

2.4.2 Assessing the instrument response

Finally, one must consider the influence of the incident laser pulses on the measured signal. Only in the case of an infinitely long probe pulse will the measured polarization represent the true molecular response. With probe pulses of practical lengths, additional broadening and spectral shifts can occur when overlap between the molecular response and the probe pulse is incomplete. These artifacts do not always hinder data interpretation, if it is understood that the peak width is somewhat

overestimated. Optimization of the overlap of the molecular response and the probe pulse can be achieved by introducing a short delay (on the order of 1 ps) between the IR and probe pulses. The optimal delay depends on the length of the probe pulse and the time scale of the molecular response.[14, 26]

For studies that examine reorientation and other dynamic processes, the instrument response can be considered precisely by simulating spectra using functions that model well-characterized laser pulses.[14, 22, 24, 26] The necessary functions include the molecular response, $R(t)$, the electric field of the IR pulse, $E_{IR}(t)$, and the electric field of the probe pulse, $E_{probe}(t-\tau)$. The representations of these functions, and the simulation of VSFG spectra, are adapted from a procedure described in Stiopkin *et al*.[26]

We represent the molecular response with a sum of exponential functions in the time domain (which is equivalent to a sum of Lorentzians in the frequency domain)

$$R(t-t_0) = -i\Phi(t-t_0)\sum A_k\, e^{-i\omega_k(t-t_0)-\Gamma_k(t-t_0)}\,, \qquad (2.27)$$

where t_0 is the zero time point, typically the time at which the peak of the IR pulse arrives, Φ is a step function imposing causality on the excitation of the molecular response by the IR pulse, and A_k is the amplitude, ω_k is the center frequency, and Γ_k is the width of the kth Lorentzian mode.

The IR pulse can be measured in the time domain directly with a cross-correlation technique, or converted from the frequency domain using a nonresonant SFG spectrum obtained from a gold substrate. Here we use a pulse with a single Gaussian time envelope:

$$E_{IR}(t) = A_{IR} e^{-\frac{(t-t_0)^2}{2(\tau_{IR})^2} - i\omega_{IR}(t-t_0)}\,. \qquad (2.28)$$

A_{IR} is the amplitude of the pulse, the first term of the exponent is the Gaussian envelope of the pulse, τ_{IR} is related to the width of the pulse, and ω_{IR} is the center frequency of the spectrum.

For the probe pulse, the spectrum is first measured by directing scatter from a gold substrate into a spectrometer. The spectrum is fit to a Gaussian, or a sum of Gaussians, and then converted into the time domain with the form (showing only one Gaussian):

$$E_{probe}(t-\tau) = A_{probe} e^{-\frac{(t-t_0-\tau)^2}{2\left(\tau_{probe}\right)^2} - i\omega_{probe}(t-t_0-\tau)}, \qquad (2.29)$$

where τ is the delay between the IR and the probe pulse, A_{probe} is the amplitude of the pulse, the first term of the exponent is the Gaussian envelope of the pulse, τ_{probe} depends on the width of the pulse, and ω_{probe} is the center frequency of the spectrum.

To simulate VSFG spectra, a coherence is first modeled as $P^{(1)}$, which is represented as a convolution of the molecular response with the IR pulse:

$$P^{(1)}(t) = \int_{-\infty}^{+\infty} R(t_0) E_{IR}(t-t_0) dt_0 = R(t_0) \circ E_{IR}(t) . \qquad (2.30)$$

$P^{(1)}$ is depicted in Figure 2.5a, showing the response of a low-viscosity liquid with a typical dephasing time of one to ten picoseconds and illustrating the asymmetry arising from its creation by the IR pulse at t = 0.[26] The upconversion of $P^{(1)}$ by the probe pulse generates $P^{(2)}$, which is the VSFG signal in the time domain, and is equal to the product of $P^{(1)}$ and the electric field of the probe pulse:

$$P^{(2)}(t,\tau) \propto P^{(1)}(t) E_{vis}(t-\tau) . \qquad (2.31)$$

The VSFG intensity is equal to the Fourier transform of $P^{(2)}$:

$$\tilde{E}_{VSFG}(\omega,\tau) \propto \int_{-\infty}^{+\infty} P^{(2)}(t,\tau) e^{i\omega t} dt, \qquad (2.32)$$

where τ is the delay between the IR and probe pulse. Therefore, $P^{(2)}$, and hence E_{VSFG}, is highly dependent on the overlap between the first-order polarization and the electric field of the probe pulse. Figure 2.5b illustrates how with a τ of zero, even though the most intense part of the pulse upconverts the most intense part of $P^{(1)}$, half of the probe pulse is "wasted" because it arrives before $P^{(1)}$ has been generated. In contrast, with a τ of 1 ps, a longer region of $P^{(1)}$ is overlapped with the higher amplitude region of the probe pulse. The effect of this enhancement can be seen in Figure 2.5c, which illustrates how by using an appropriate delay, the VSFG spectrum can increase in intensity, as well as resolution, affording a closer representation of the molecular response.

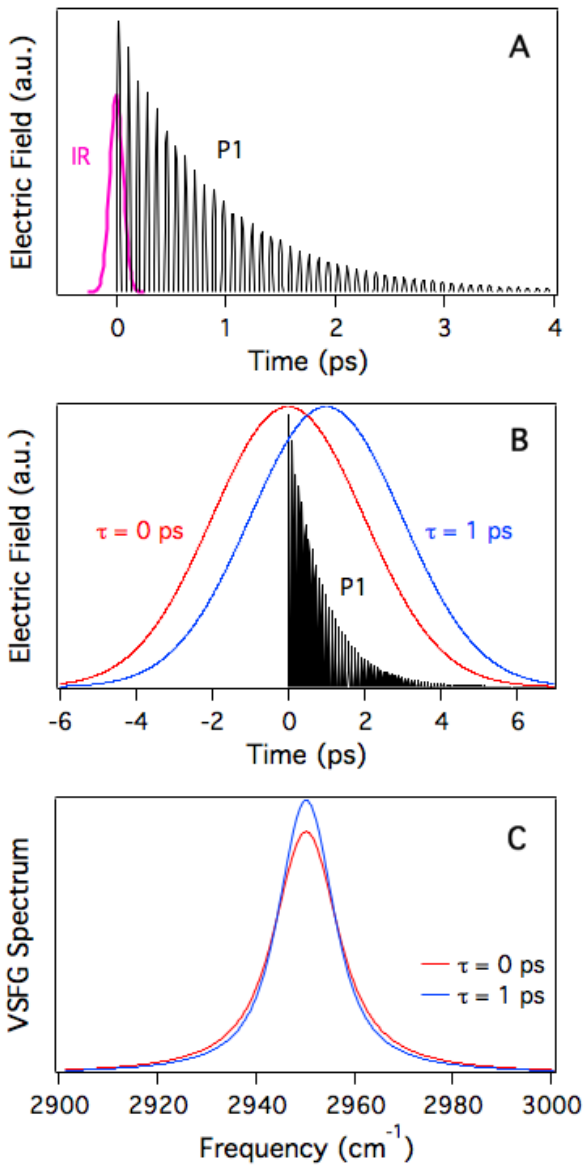

Figure 2.5 Simulated representation of the steps in generating a VSFG signal. a) A first-order polarization, $P^{(1)}$, is generated by an ultrashort IR pulse, shown in magenta (with envelope shown only). b) A probe pulse with length on the order of picoseconds (envelope shown only) overlaps with $P^{(1)}$ to generate the second-order polarization, $P^{(2)}$ (not shown). A probe pulse delayed by 1 ps (blue) increases the amount of overlap between $P^{(1)}$ and the probe pulse. c) Comparison of the VSFG spectra in the frequency domain for IR probe delays of 0 and 1 ps. A delay of 1 ps improves both resolution and intensity of the spectrum.

2.5 References

1. Rivera, C. A.; Fourkas, J. T., Reexamining the interpretation of vibrational sum-frequency generation spectra. *Int. Rev. Phys. Chem.* **2011,** *30* (4), 409-443.

2. Richmond, G. L., Molecular bonding and interactions at aqueous surfaces as probed by vibrational sum frequency spectroscopy. *Chem. Rev.* **2002,** *102* (8), 2693-2724.

3. Buck, M.; Himmelhaus, M., Vibrational spectroscopy of interfaces by infrared-visible sum frequency generation. *J. Vac. Sci. Technol. A* **2001,** *19* (6), 2717-2736.

4. Tian, C. S.; Shen, Y. R., Recent progress on sum-frequency spectroscopy. *Surf. Sci. Rep.* **2014,** *69* (2-3), 105-131.

5. Zhuang, X.; Miranda, P. B.; Kim, D.; Shen, Y. R., Mapping molecular orientation and conformation at interfaces by surface nonlinear optics. *Phys. Rev. B* **1999,** *59* (19), 12632-12640.

6. Zheng, D. S.; Wang, Y.; Liu, A. A.; Wang, H. F., Microscopic molecular optics theory of surface second harmonic generation and sum-frequency generation spectroscopy based on the discrete dipole lattice model. *Int. Rev. Phys. Chem.* **2008,** *27* (4), 629-664.

7. Wang, H. F.; Gan, W.; Lu, R.; Rao, Y.; Wu, B. H., Quantitative spectral and orientational analysis in surface sum frequency generation vibrational spectroscopy (SFG-VS). *Int. Rev. Phys. Chem.* **2005,** *24* (2), 191-256.

8. Wang, J.; Paszti, Z.; Even, M. A.; Chen, Z., Measuring polymer surface ordering differences in air and water by sum frequency generation vibrational spectroscopy. *J. Amer. Chem. Soc.* **2002,** *124*, 7016-23.

9. Souna, A. J.; Clark, T. L.; Fourkas, J. T., Effect of temperature on the organization of acetonitrile at the silica/liquid interface. *J. Phys. Chem. C* **2017,** *121* (47), 26432-26437.

10. Wei, X.; Hong, S. C.; Zhuang, X.; Goto, T.; Shen, Y. R., Nonlinear optical studies of liquid crystal alignment on a rubbed polyvinyl alcohol surface. *Phys. Rev. E* **2000,** *62*, 5160-72.

11. Zhang, D.; Gutow, J.; Eisenthal, K. B., Vibrational spectra, orientations, and phase transitions in long-chain amphiphiles at the air/water interface: probing the head and tail groups by sum frequency generation. *J. Phys. Chem.* **1994,** *98* (51), 13729-13734.

12. Guyot-Sionnest, P.; Hunt, J. H.; Shen, Y. R., Sum-frequency vibrational spectroscopy of a Langmuir film: Study of molecular orientation of a two-dimensional system. *Phys. Rev. Lett.* **1987,** *59* (14), 1597-1600.

13. Fredkin, D. R.; Komornicki, A.; White, S. R.; Wilson, K. R., *Ab initio* infrared and Raman spectra. *J. Chem. Phys.* **1983,** *78* (12), 7077-7092.

14. Rivera, C. A.; Souna, A. J.; Bender, J. S.; Manfred, K.; Fourkas, J. T., Reorientation-induced spectral diffusion in vibrational sum-frequency-generation spectroscopy. *J. Phys. Chem. B* **2013,** *117* (49), 15875-85.

15. Henry, M. C.; Piagessi, E. A.; Zesotarski, J. C.; Messmer, M. C., Sum-frequency observation of solvent structure at model chromatographic interfaces: Acetonitrile-water and methanol-water systems. *Langmuir* **2005,** *21* (14), 6521-6526.

16. Wei, X.; Shen, Y. R., Motional effect in surface sum-frequency vibrational spectroscopy. *Phys. Rev. Lett.* **2001,** *86*, 4799-4802.

17. Fourkas, J. T.; Walker, R. A.; Can, S. Z.; Gershgoren, E., Effects of reorientation in vibrational sum-frequency spectroscopy. *J. Phys. Chem. C* **2007,** *111*, 8902-8915.

18. Liu, S. L.; Fourkas, J. T., Orientational time correlation functions for vibrational sum-frequency generation. 1. Acetonitrile. *J. Phys. Chem. A* **2013,** *117* (29), 5853-5864.

19. Liu, S.; Hu, Z.; Weeks, J. D.; Fourkas, J. T., Structure of liquid propionitrile at interfaces. 1. Molecular dynamics simulations. *J. Phys. Chem. C* **2012,** *116*, 4012-4018.

20. Liu, S.; Fourkas, J. T., Orientational time correlation functions for vibrational sum-frequency generation. 3. Methanol. *J. Phys. Chem. C* **2015,** *119*, 5542-5550.

21. Ding, F.; Hu, Z.; Zhong, Q.; Manfred, K.; Gattass, R.; Brindza, M. R.; Fourkas, J. T.; Walker, R. A.; Weeks, J. D., Interfacial organization of acetonitrile: simulation and experiment. *J. Phys. Chem. C* **2010,** *114* (41), 17651-17659.

22. Wang, H. F.; Velarde, L.; Gan, W.; Fu, L., Quantitative sum-frequency generation vibrational spectroscopy of molecular surfaces and interfaces: lineshape, polarization, and orientation. *Annu. Rev. Phys. Chem.* **2015,** *66*, 189-216.

23. Roke, S.; Kleyn, A. W.; Bonn, M., Femtosecond sum frequency generation at the metal-liquid interface. *Surf. Sci.* **2005,** *593* (1-3), 79-88.

24. Bonn, M.; Ueba, H.; Wolf, M., Theory of sum-frequency generation spectroscopy of adsorbed molecules using the density matrix method—broadband vibrational sum-frequency generation and applications. *J. Phys.- Condens. Mat.* **2005,** *17*, S201-S220.

25. Ding, F.; Zhong, Q.; Brindza, M. R.; Fourkas, J. T.; Walker, R. A., Ti:sapphire, broadband vibrational sum-frequency generation spectrometer with a counter-propagating geometry. *Opt. Express* **2009,** *17* (17), 14665-14675.

26. Stiopkin, I. V.; Jayathilake, H. D.; Weeraman, C.; Benderskii, A. V., Temporal effects on spectroscopic line shapes, resolution, and sensitivity of the broad-band sum frequency generation. *J. Chem. Phys.* **2010,** *132,* 234503.

Chapter 3: Experimental Apparatus

3.1 Introduction

The experiments described in the following chapters employ a broadband, counter-propagating VSFG spectrometer. The broadband approach, developed by Richter and coworkers,[1] uses a high bandwidth (~250 cm^{-1} in our case) IR pulse, allowing for rapid data acquisition by eliminating the need to scan over IR wavelengths. At the sample, a counter-propagating geometry simplifies changing samples and reduces the nonresonant background signal.[2]

3.2 VSFG Experimental Setup

A schematic of the VSFG experimental apparatus is shown in Figure 3.1. The laser source is a 1 kHz, Ti-sapphire regenerative amplifier (Coherent Legend Elite), which generates 3 W of 800-nm, 80-fs pulses. The amplifier is seeded with 800-nm, mode-locked pulses from a 76-MHz, Ti-sapphire oscillator (Coherent Mira) and pumped with a Q-switched, frequency-doubled, neodymium-doped yttrium lithium fluoride (Nd:YLF), 1 kHz, 532-nm (Coherent Evolution) laser. Before entering the Legend, the Mira output is modified with a pulse shaper using a MIIPS algorithm to ensure a nearly transform-limited pulse at the sample.[3] The oscillator is pumped by a 5.2-W, continuous wave, 532-nm (Coherent Verdi-12) laser. The amplifier output is directed through a 30/70 beam splitter, after which the 30% is sent to the mid-IR generating path and the 70% to the 800-nm probe path. The probe path is divided again with a 50/50 beam splitter, with 50% going to the sample and the remaining 50% sent to a beam dump (omitted from Figure 3.1). The mid-IR pulses are generated with an optical parametric amplifier (OPA) with a noncollinear difference frequency

generation (NDFG) module (TOPAS, Light Conversion) and have a pulse energy of ~15 μJ. The IR wavelength is tuned with the WinTOPAS software, which controls the rotation of three nonlinear crystals, the translation of delay stages to control temporal overlap, and orientation of a mirror that improves overlap between the signal and idler beam at the NDFG crystal. The NDFG output passes through a half-wave plate and polarizer that control the polarization of the beam at the sample.

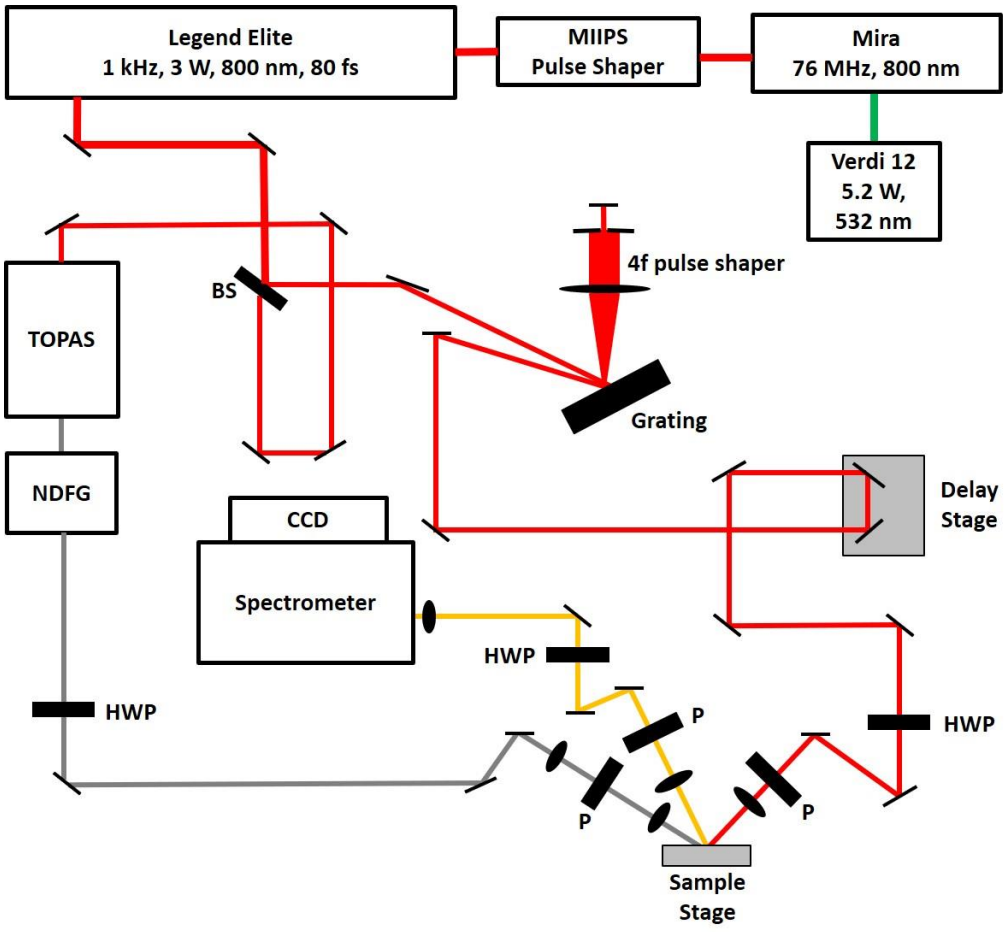

Figure 3.1. Schematic of VSFG spectrometer. BS = beam splitter; HWP = half-wave plate; P = polarizer; and CCD = charge-coupled device. Beam frequency is indicated as follows: green = 532 nm; red = 800 nm; grey = mid-IR (~3000 cm^{-1}); and yellow = sum frequency (~ 650 nm).

The probe pulse is directed through a folded 4*f*-pulse shaper, which selects a narrow portion (4-10 cm^{-1}) of the 800-nm spectrum using a grating (1800 lines/mm, Spectrogon) and a movable slit. A motorized delay stage controls temporal overlap of the probe and IR pulses at the sample. The probe pulse traverses a half-wave plate and polarizer that control the polarization at the sample.

The angles of incidence of the IR and probe beams are -58º and 61º from the surface normal in the counter-propagating geometry shown in Figure 2.2. (A negative angle designates an angle directed to the left of the surface normal.) According to the phase-matching condition, the sum- frequency signal is generated from the sample surface at -32.8º. The polarization of the signal is selected with a polarizer, and a half-wave plate ensures that the light is always *S*-polarized when it enters the spectrometer, which is polarization-sensitive. The signal is directed through the entrance slit of a spectrometer (Acton, SP2300i) and detected with a 100 × 1340 pixel CCD array (Spec-10:100, Roper Science) with a resolution of 0.02 nm/pixel.

3.3 Alignment

The alignment procedure includes optimization of the mid-IR pulse, pulse-shaping to ensure a transform-limited pulse, temporal and spatial alignment at the sample, and signal alignment into the spectrometer.

3.3.1 Mid-IR pulse optimization

Mid-IR generation and tuning is performed with the WinTOPAS software, which automatically adjusts the necessary motorized optics. However, manual adjustments are necessary within the first and second pass of the OPA and in the NDFG

module to maximize power and bandwidth. The "signal" that is pumped by the 800-nm light in the first pass of the OPA is a white- light continuum that is generated by focusing a small portion of the 800-nm beam through a sapphire plate. The quality of the white-light continuum is improved by optimizing pulse compression in the amplifier by adjusting a motorized mirror. Then the spatial and temporal overlap are adjusted at each of the nonlinear crystals: the first and second pass of the OPA and the $AgGaS_2$ crystal in the NDFG module. In the first pass of the OPA, and in the NDFG unit, the beams overlap noncollinearly, and therefore the interacting beams must be at the optimal angle from each other and from the surface of the crystal.

3.3.2 MIIPS Pulse-shaping

To generate a VSFG signal effectively, both the IR and probe pulses should be close to the transform limit. To attain a nearly transform-limited pulse we implement a pulse shaping procedure using MIIPS algorithm-based software.[3] The unstretched probe pulse (with the slit removed) is focused through a barium borate crystal positioned within several centimeters of the sample stage to generate 400-nm light. The 400-nm spectrum is collected with a fiber optic cable and analyzed by the MIIPS software in real time. The software compares the 800-nm spectrum to the 400-nm spectrum and simultaneously adjusts the phase of each frequency component of the seed pulse using a grating and a spatial light modulator positioned immediately before the amplifier. The program will iterate until the calculated τ/τ_{TL} is less than 1.02, where τ is the calculated pulse length and τ_{TL} is the length of a transform-limited pulse.

3.3.3 Alignment at the sample

The IR beam is first aligned to the sample using a HeNe tracer. To overlap the IR and probe pulses at the sample spatially and temporally, a ZnSe substrate is used. The focused IR and 800-nm beams each generate a blue luminescence that can be easily overlapped by eye. Once spatial overlap is achieved, temporal overlap is found by changing the path length of the 800-nm beam in 167 fs increments using a motorized delay stage, until an orange glow is observed coming from the ZnSe. The orange light is then focused and directed into the entrance slit of the spectrometer. The alignment and overlap are fine-tuned by replacing the ZnSe with a gold substrate, the surface of which generates a strong nonresonant SFG response.

3.4 Data Collection

The gold spectrum also serves to normalize sample spectra. The nonresonant response is independent of wavelength in the methyl stretch region, and the signal is proportional to the IR intensity only. A gold spectrum is therefore representative of the spectrum of the IR pulse, which eliminates the need to measure this spectrum directly.[4] If the vibrational modes of interest are far apart in energy, the IR wavelength can be tuned in increments of 50-100 nm throughout a range sufficient to excite the necessary vibrational modes. A gold spectrum is collected at each of these wavelength settings. The symmetric stretch of acetonitrile can be measured with one setting only. Calibration is performed by placing a thin sheet of polystyrene in the path of the IR beam while collecting a gold spectrum (see below).

Prior to performing sample scans, the delay between the IR and probe pulses is adjusted to optimize the overlap between the molecular response generated by the IR

and the electric field of the probe pulse.[5] The sample stage height is adjusted in increments of approximately 6 μm while maximizing the intensity. With the IR beam blocked, a background spectrum is first measured for an acquisition time equal to that used for the sample. The background spectrum will be subtracted automatically from any subsequent sample scan. Sample scans are repeated at least three times with an acquisition time that depends on the strength of the signal. This time is generally in the range of 30-480 s.

3.5 Data Analysis

All spectra are calibrated and normalized using a LabVIEW program. Four absorption lines are selected from the polystyrene calibration spectrum, as shown in Figure 3.2. After checking for a linear correspondence with literature IR absorption values, the frequency points from the measured spectra are calibrated by interpolation. A normalization range is chosen for the gold spectrum at each wavelength, only selecting data points with greater than a threshold of 10,000 counts, relative to a noise level of 30 counts. Sample scans are averaged together before normalizing and calibrating.

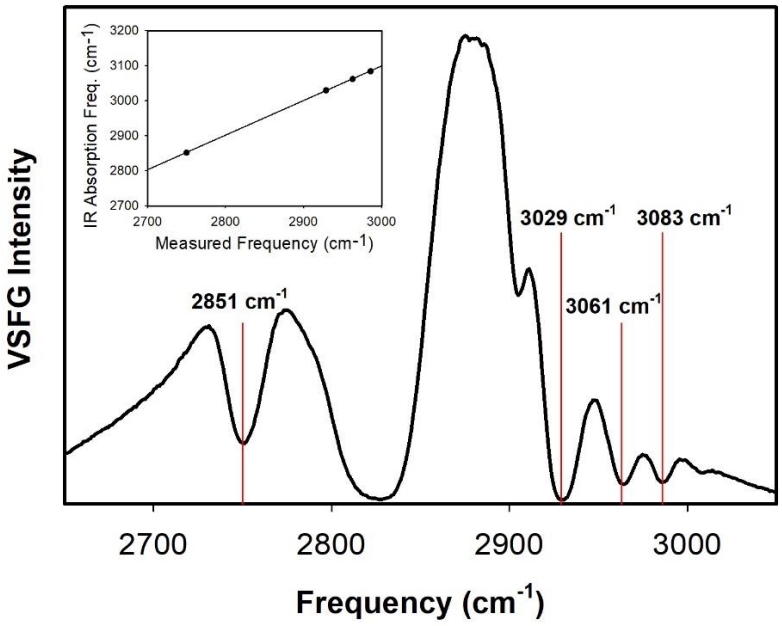

Figure 3.2. VSFG spectrum of a nonresonant gold substrate with a polystyrene film placed in the IR path. The red lines indicate the four peaks used to calibrate the VSFG spectra. The inset indicates the expected linear relationship between the measured frequency and the IR absorption peaks for polystyrene. (The 800-nm probe frequency has been subtracted from the actual measured frequency values to arrive at the frequencies for the *x*-axes.)

Spectral fitting is performed using a combination of LabVIEW, SigmaPlot, and Igor Pro fitting algorithms and using Lorentzian functions, as described in Section 2.4 and equation 2.24. Alternatively, as in the studies described in Chapter Seven and Eight, acetonitrile spectra are analyzed as a single peak (without fitting to Lorentzian functions). Instead, the maximum three points are fit to a parabola, with the peak of the parabola representing both the maximum intensity and peak frequency. The FWHM is calculated by interpolating between points at half of the peak of the parabola.

3.6 References

1. Richter, L. J.; Petralli-Mallow, T. P.; Stephenson, J. C., Vibrationally resolved sum-frequency generation with broad-bandwidth infrared pulses. *Opt. Lett.* **1998,** *23* (20), 1594-1596.

2. Ding, F.; Zhong, Q.; Brindza, M. R.; Fourkas, J. T.; Walker, R. A., Ti:sapphire, broadband vibrational sum-frequency generation spectrometer with a counter-propagating geometry. *Opt. Express* **2009,** *17* (17), 14665-14675.

3. Lozovoy, V. V.; Pastirk, I.; Dantus, M., Multiphoton intrapulse interference. IV. Ultrashort laser pulse spectral phase characterization and compensation. *Opt. Lett.* **2004,** *29,*
775-7.

4. Liebsch, A., Theory of sum frequency generation from metal surfaces. *Appl. Phys. B-Lasers O.* **1999,** *68*, 301-304.

5. Stiopkin, I. V.; Jayathilake, H. D.; Weeraman, C.; Benderskii, A. V., Temporal effects on spectroscopic line shapes, resolution, and sensitivity of the broad-band sum frequency generation. *J. Chem. Phys.* **2010,** *132*, 234503.

Chapter 4: How Clean Is the Clean Solvent You Use to Clean Your Optics? A Vibrational Sum-Frequency-Generation Study

Adapted from: Souna, A. J.; Bender, J. S.; Fourkas, J. T. *Appl. Opt.*, 2017, 56(13), 3875-3878.
Research designed and conducted by: Amanda J. Souna and John S. Bender
Authored by: Amanda J. Souna

4.1 Introduction

When working with optics, it is of utmost importance that all surfaces be pristine. Dust, dirt and oils can cause scattering and power loss, debris can burn or fuse to surfaces, and residue can absorb light, potentially altering experimental measurements. It is well understood that optics may be cleaned properly with appropriate solvents, but there is less awareness of the importance of correct solvent storage and transfer. Many optics manufacturers give guidelines on cleaning optics, but these guidelines generally focus on technique and choice of solvent, while giving solvent storage and transfer little mention.

Here I focus on three of the solvents most commonly used to clean optics: acetone, methanol, and isopropanol. Even high-purity grades of these solvents contain small amounts of impurities that may remain behind as residue if they have a low vapor pressure and a high affinity for the surface being cleaned. For example, acetone readily condenses to form mesityl oxide and other related compounds such as diacetone alcohol and phorone.[1-3] Methanol often contains dimethoxyalkanes,[4] and isopropanol contains similar impurities as acetone, such as mesityl oxide.[5] Issues with these contaminants are typically minimized by using the purest grade of solvent available.

Although the importance of using high-purity solvents for cleaning optics is widely understood, the role that the methods of solvent storage and use play in

subsequent contamination is not as well appreciated. Solvents may come into contact with any number of surfaces, such as plastic squirt bottles, medicine droppers, plastic pipettes, rubber septa, and syringes, before being deposited on optics.

I examined the influence of materials used in storage containers and solvent transfer devices that are commonly used in optics laboratories on the purity of the solvents used to clean optics. Low-density polyethylene (LDPE) and high-density polyethylene (HDPE) are noted for their high chemical resistance to solvents.[6] As such, these polymers are often materials of choice for squirt bottles and plastic pipettes. Rubber is used for medicine-dropper bulbs, syringes and septa. To study the influence of these materials on solvents used to clean optics, vibrational sum-frequency-generation (VSFG) spectroscopy was used to examine fused silica surfaces that have been cleaned with exposed solvents. The results indicate that even brief contact of the solvents with plastic or rubber can result in a persistent residue being left on an optic after cleaning.

4.2. Methods

The VSFG spectrometer used to collect these spectra was described in Chapter Three in sections 3.1-3.3. The bandwidth for the 800-nm probe pulse was 6 cm^{-1}, and the IR-probe delay was 667 fs for optimized spectral resolution and signal intensity. The solvents used were HPLC-grade (Fisher Chemical) and 99.6% ACS reagent-grade (ACROS) acetone, HPLC-grade methanol (Chromasolv, Sigma-Aldrich), and ACS reagent-grade isopropanol (Ricca). Control solvents were stored in new, glass scintillation vials for the duration of experiments within one day, with fresh solvent poured from the original bottle into a new vial on a different day. The control solvents

were never stored in a bottle with a medicine dropper, in which the solvent vapor would have access to the dropper bulb. For experiments with polyethylene, approximately 10 mL of solvent was stored in either an LDPE squirt bottle for up to one month or an HDPE container for up to two weeks. For experiments with rubber, the solvents were drawn up into the dropper and, with the dropper inverted, allowed to rest inside the rubber bulb for approximately five seconds. For comparison, the rubber bulb was also separated from the dropper, and submerged in acetone for 24 hours. In addition, the effect of using an LDPE plastic pipette or a polypropylene medical syringe with a rubber seal was considered.

To reduce the number of experimental variables, for the initial trials, no lens paper was used and there was no variation in application technique. Approximately 0.5 mL of solvent was poured directly from a vial onto the top a 23.6 mm × 47.5 mm fused silica flat (Hellma). The flat was first rinsed with acetone, methanol, and then water consecutively, oven-dried, and oxygen-plasma-cleaned. The cell was held at a nearly vertical angle while pouring, so that the solvent quickly ran across the cell without pooling. In another set of measurements, an equal volume of solvent was poured onto lens paper that was then used to wipe the optic. For all measurements, the optic was allowed to dry for at least five minutes after solvent exposure. Additionally, to measure the persistence of any residue on the surface, the signal was measured one day after applying the solvent.

All measurements included three 2-minute scans with the infrared beam centered at 2900 cm^{-1}, which is in the C-H stretching region of the infrared spectrum, and therefore should reveal the presence of most organic contaminants on optics. Scans

were taken of the optic prior to contact with solvents to ensure contaminants were not already present. All spectra were normalized and calibrated with the procedure described in Chapter Three, sections 3.4 and 3.5.

To identify contaminants, gas chromatography-electron ionization-mass spectrometry (GC-EI-MS) measurements (JEOL JMS-700 MStation) were also performed on acetone contained in an LDPE bottle for one month and on acetone in which a rubber bulb had been submerged overnight.

4.3. Results and discussion

4.3.1 Solvent purity

As a control, I first tested whether the solvents left any detectable residue if they had only been in contact with glass, and if there was any significant difference among the solvents (Figure 4.1). I was careful to prevent the solvent from resting or pooling before drying on the surface, which would increase the likelihood of leaving a residue. With the exception of isopropanol, the weak VSFG signals in Figure 4.1 indicate that an organic residue left from the solvents is minimal. The small signal from the bare silica (black) indicates a nonresonant response from the silica. The signal originating from methanol (blue) is slightly larger than acetone (red), but unlikely to be of practical concern, based on comparison with other data (see below). It should be noted, however, that for methanol, if the region of the flat measured is an area towards the edge where the methanol has accumulated, then the intensity is several times greater than that shown in Figure 4.1, similar in intensity to isopropanol.

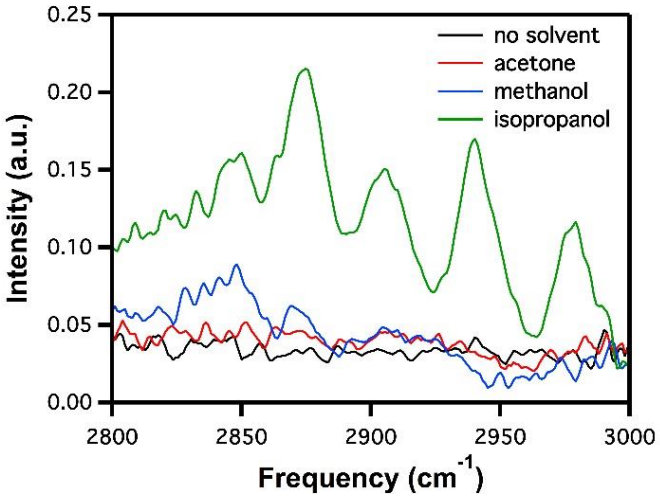

Figure 4.1. VSFG spectra of the silica/air interface after deposition of different clean solvents compared to a bare silica surface. All spectra presented below are on the same intensity scale.

Isopropanol tends to leave a residue throughout the region with which it comes in contact. I also checked to see if the residue remained the following day, and the signal did not diminish. The spectrum from isopropanol's residue resembles that of isopropanol itself, but because the residue remains on the surface over time, it is likely a mixture of impurities with vapor pressures lower than isopropanol.

4.3.2 Solvent contamination: LDPE

In striking contrast to the control spectra, VSFG spectra of solvents that have been in contact with LDPE are intense, indicating the presence of substantial quantities of organics on the silica surface (Figure 4.2). All three solvents left a substantial residue after only 1 h of exposure to LDPE. The similarity of all the spectra indicates that all of the solvents have a common contaminant or contaminants, and that the spectra do not arise from the solvents themselves, as is also confirmed by spectra of acetone, methanol, and isopropanol that were measured at the silica/vapor interface (not shown). Although isopropanol can leave a residue on its own, after contact with LDPE,

isopropanol leaves an increased residue with different spectral features. Methanol also can leave moderate residue if it accumulates, but after contact with LDPE, it leaves substantially more residue and leaves it throughout the area with which it comes into contact.

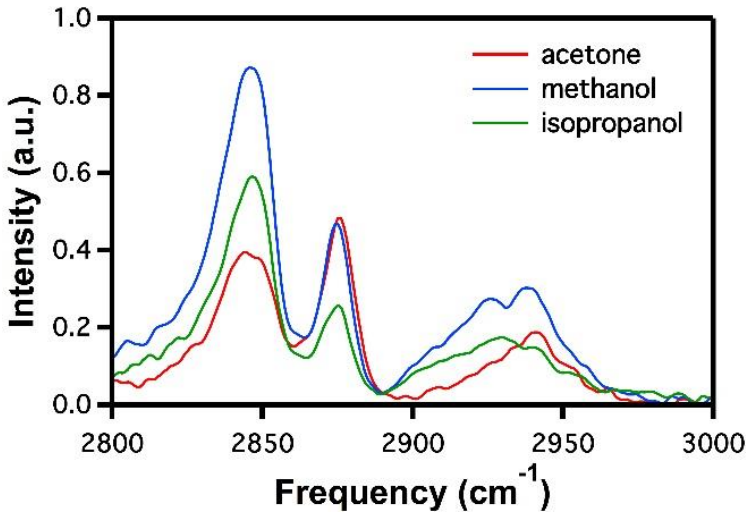

Figure 4.2. VSFG spectra of a silica/air interface after deposition of different solvents after 1 h of contact with LDPE.

VSFG spectra were measured for optics that had been cleaned with solvents that had remained in the LDPE bottle for up to one month. Spectra are shown for acetone in Figure 4.3, but similar results were found for methanol and isopropanol. Quantitative comparison of the signal intensity is impractical due to the heterogeneous surface coverage, but within the measurement error there is no systematic increase in signal for exposure times of greater than 1 h. These results suggest that the solvents become saturated with contaminants in less than 1 h of exposure. Because the VSFG signal is only sensitive to interfaces, it is also possible that 1 h of exposure to LDPE is sufficient to create a contaminant layer on the optic that is a monolayer or more thick, such that adding more contaminant will not increase the VSFG signal.

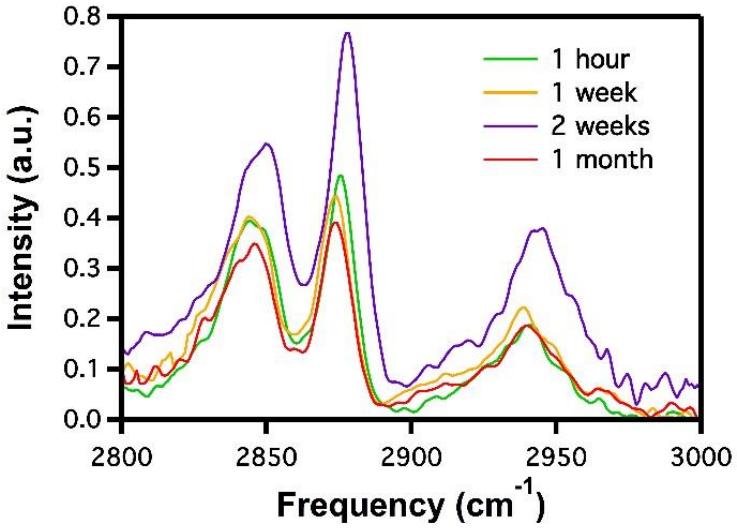

Figure 4.3. VSFG spectra of the silica/air interface after deposition of acetone left in an LDPE squirt bottle for different lengths of time.

GC-EI-MS analysis was performed in an attempt to identify the contaminants. The total ion chromatogram (TIC) of acetone stored in an LDPE bottle for one month is shown in Figure 4.4. The mass spectra of 12 of the small peaks shown reveal the presence of a variety of branched, long-chain alkanes. These contaminants may arise from degradation of LDPE, which is more likely to occur at branching sites,[7] by the solvents. Another possibility is that the degradation products are already present as a result of processing at high temperatures, and then leach from the surface by the solvents.[8] The contaminants could also include plasticizers, which are often used in polyethylene products and typically are not chemically bonded to the polymer matrix and therefore leach easily.[9] Common plasticizers such as phthalates often contain alkyl groups, which would give the same spectral signature as the branched alkanes identified in the GC-EI. Plasticizers are likely low in concentration, however, because they do not present as a dominant peak in the TIC.

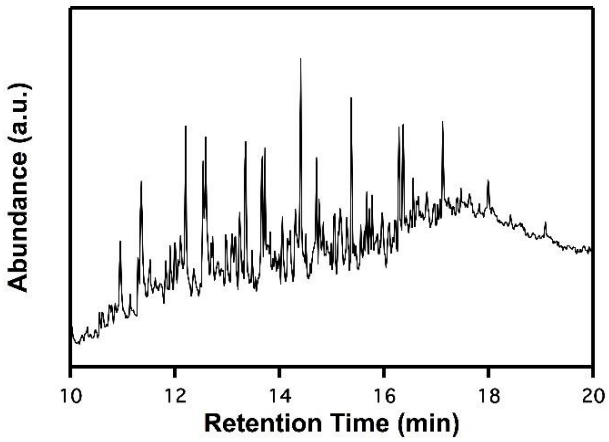

Figure 4.4. TIC of acetone left in an LDPE squirt bottle for one month. Many of the small peaks matched branched alkanes.

The VSFG spectrum is also consistent with the presence of branched alkanes. Previous VSFG studies of medium- and long-chain alkanes and alcohols show similar peaks with peak assignments including a methylene symmetric stretch at 2850 cm^{-1}, a methyl symmetric stretch at 2875 cm^{-1}, a methylene asymmetric stretch at 2920 cm^{-1}, a Fermi resonance of the methyl symmetric stretch and an overtone of a bending mode at 2940 cm^{-1}, and a methyl asymmetric stretch at 2960 cm^{-1}.[10,11] Other studies suggest that the peak at 2920 cm^{-1} is a methylene Fermi resonance, because this peak is in phase with the 2850 cm^{-1} symmetric stretch peak, whereas symmetric and asymmetric modes should be of opposite phase.[12-14] The spectra are also similar to those of LDPE films,[15] with the exception of the 2875 cm^{-1} methyl stretch peak, which confirms the presence of segments of small hydrocarbon chains.

An orientational analysis of such a complex mixture of components is challenging, and is well beyond the scope of this work. However, qualitative comparisons can be made with previous studies, including a VSFG study showing that medium-chain alkanes at the silica/vapor interface have a tendency to lie parallel to the

surface.[11] Our VSFG spectra have similar structure, suggesting that the peaks arise from branched alkanes lying with their long axes parallel to the surface and branches extending into the air at various angles.

4.3.3 Solvent contamination: HDPE

Contamination originating from HDPE bottle occurs more slowly than that from LDPE. HDPE is known to be more chemically resistant than LDPE, due to less branching and a more crystalline structure.[6] Even in HDPE, however, all three solvents are likely contaminated substantially after a 2-week exposure, as shown in Figure 4.5; however, this can be said with less certainty in the case of methanol and isopropanol, due to the impurities already present in these solvents. GCMS was not performed on these samples because the VSFG spectral peaks lie in similar positions to those from the LDPE bottles, and therefore the contaminants are likely to be chemically similar in both cases.

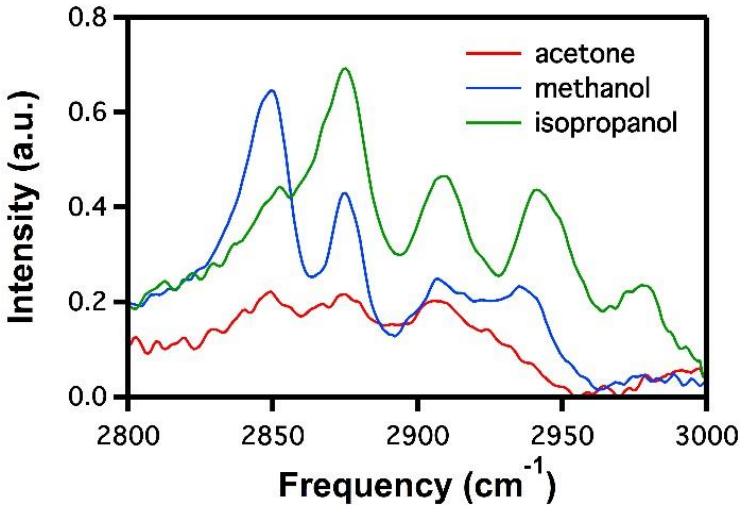

Figure 4.5. VSFG spectra of the silica/air interface after deposition of different solvents that had been in contact with an HDPE squirt bottle for two weeks.

4.3.4 Solvent contamination: rubber

Rubber medicine droppers commonly are used in the cleaning of optics, and it is generally assumed that the liquid solvent only comes into contact with glass. Our data show, however, that if the liquid solvent comes into contact with the rubber bulb even for a few seconds, significant contamination can occur. Figure 4.6 shows spectra from all three solvents after contact with the rubber bulb for only 5 s. The spectra are all quite intense, particularly in the case of acetone and methanol. The evidence is less clear for isopropanol, because the peaks are not as intense, and the signal does not differ substantially from the residue already left behind by isopropanol. The substantial vapor pressures of these solvents suggest that contaminants will be extracted from the rubber over time even without direct contact with the liquid.

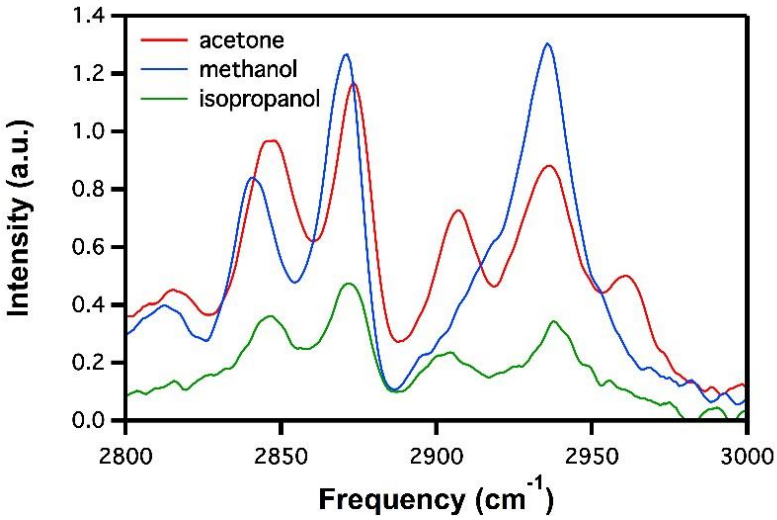

Figure 4.6. VSFG spectra of the silica/air interface after deposition of different solvents after contact with the rubber bulb from a glass medicine bottle for 5 s.

Figure 4.7 compares spectra of acetone left in contact with the rubber bulb for 5 s and 24 h. As was the case for LDPE, the intensity of the spectra is essentially unchanged after continued exposure, suggesting that the optic surface is saturated

rapidly with contaminants. In this case, the acetone is not likely saturated with contaminants after 5 s, because after 24 h the acetone is visibly different, with a pinkish color, and the residue on the optic is white. The fact that the spectrum changes with time may indicate that one or more contaminants is extracted from the rubber more on a time scale longer than 5 s.

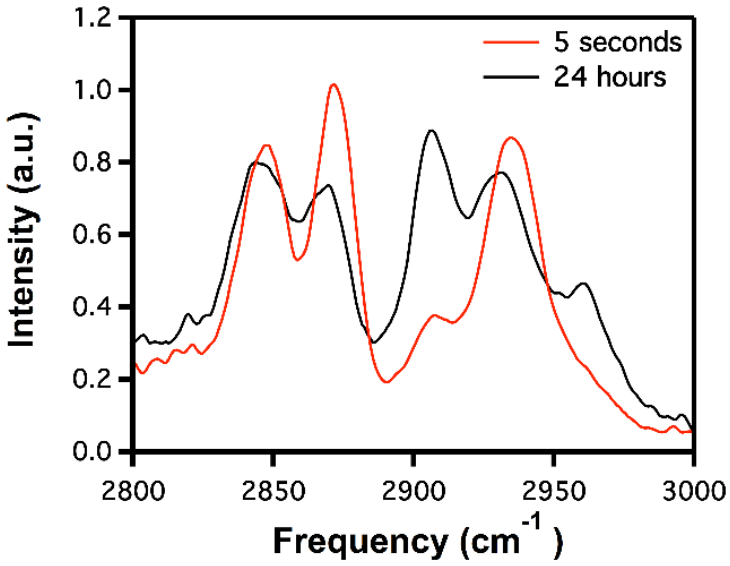

Figure 4.7. VSFG spectra of the silica/air interface after deposition of acetone in contact with a rubber bulb for 5 s and 24 h.

The TIC from the GCMS analysis of acetone left in contact with the rubber dropper bulb for 24 h is shown in Figure 4.8. The chromatogram shows an abundance of small peaks with a retention time between 13 and 19 minutes, similar to the LDPE-acetone sample, signifying the presence of long-chain hydrocarbons that may arise from degraded rubber. In contrast to LDPE, there is the distinctive presence of a single large peak at 14.99 minutes. Mass spectral analysis of this peak indicated that it arises from 2,2'-methylenebis[6-(1,1-dimethylethyl)-4-ethyl-phenol], a rubber additive used as a stabilizer and antioxidant.[16] Its IR spectrum contains a broad band from 2800 to 3000 cm^{-1},[17] which corresponds to the VSFG spectra of the residue.

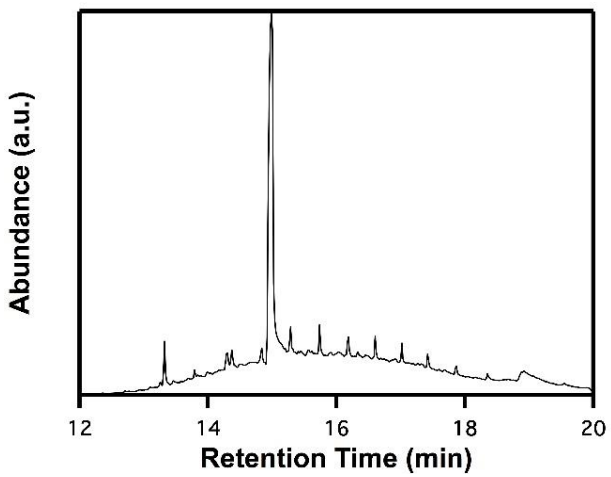

Figure 4.8. TIC of acetone in which a rubber medicine-dropper bulb had been submerged inside for 24 hours. Mass spectral analysis of the 14.99 min peak indicates that it arises from 2,2'-methylenebis[6-(1,1-dimethylethyl)-4-ethyl-phenol]. Although the presence of this species in the liquid does not necessarily signify presence in the residue, and its IR spectrum does not distinguish it from other organic components,[17] the large size of this molecules suggests that it would remain on the silica surface rather than evaporating.

4.3.5 Persistence of contaminants

Having determined that exposure to polyethylene and rubber leads to substantial deposition of contaminants on optics, the persistence of these species was next examined. A previous VSFG study showed that adsorption of alkanes on silica is reversible,[12] and alkanes will desorb in approximately 1 min if the surface is exposed to a flow of pure helium. However, this study was based on short-chain, unbranched alkanes. To measure contaminant persistence, I compared spectra obtained several minutes after contact with solvent to spectra obtained after 24 h. For both LDPE (Figure 4.9a) and rubber (Figure 4.9b) the VSFG signal from contaminants is essentially unchanged after 24 h. The VSFG signal increased slightly with time in most cases, which may be due to surface heterogeneity or may arise from reconstruction of the contaminant layer over time.

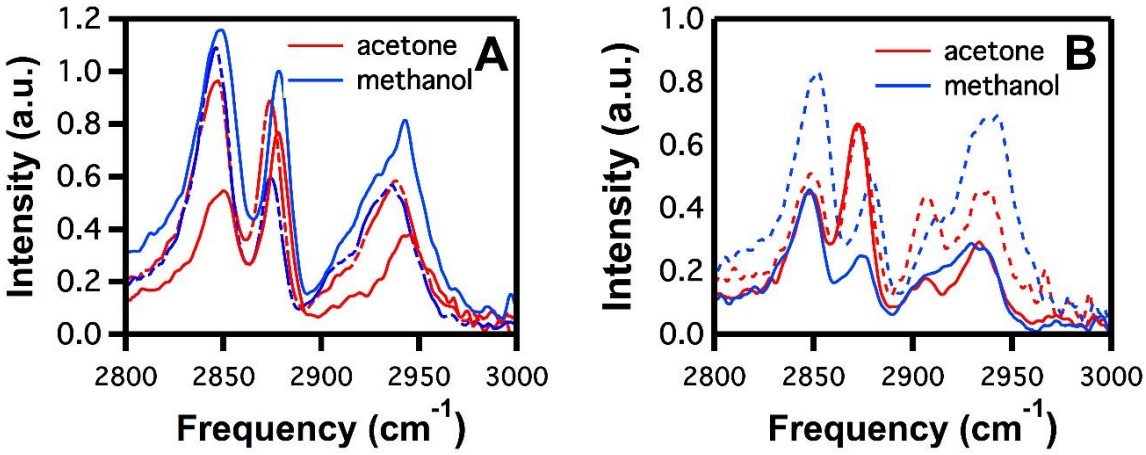

Figure 4.9. VSFG spectra of the silica/air interface after deposition of acetone and methanol left in contact with (A) LDPE and (B) rubber. Solid lines show signal of residue after the surface dried, and dashed lines show signal after the sample is left sitting for one day.

4.3.6 Lens paper

Due to the variability in the manner in which lens paper is used to clean optics (e.g., folding style, degree of saturation, and 'drop and drag' versus 'brush' technique), in the above experiments I chose to emphasize solvent contamination alone. To investigate any potential role of lens paper, two additional experiments were performed. First, optics were cleaned with two different brands of lens paper (Thor Labs and Tiffen) using HPLC grade and 99.6% ACS Reagent Grade acetone that had only been exposed to glass. Virtually no VSFG signal was observed with either brand of lens paper with either type of acetone.

I next examined whether lens paper influences the amount of residue deposited by a contaminated solvent. As shown in Figure 4.10, lens paper saturated with solvent leaves less residue on fused silica than does solvent deposited directly on the substrate. However, even when lens paper is used for cleaning, a substantial residue is left on the optics when the solvent is contaminated.

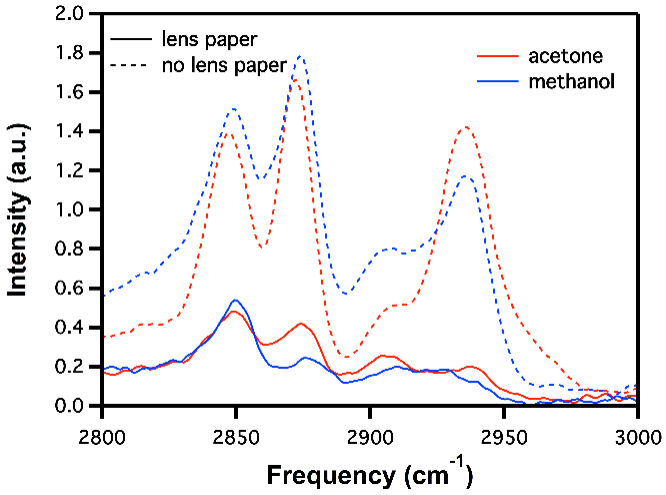

Figure 4.10. VSFG spectra of the silica/air interface after deposition of acetone and methanol left in contact with the rubber bulb from a medicine dropper vs. pouring the solvent directly on the surface.

4.3.7 Other sources of contamination

In addition to polyethylene bottles and rubber medicine droppers, I also investigated other sources of contamination including two brands of disposable plastic pipettes and disposable medical syringes. Both brands of plastic pipettes were composed of LDPE, and resulted in a strong signal after contact with all three solvents, with a similar spectrum and intensity as that originating from the LDPE bottles. The contamination imparted to the solvent was substantial after only seconds of contact, most likely because the volume of solvent exposed to the LDPE surface was small. A few seconds of contact of acetone and methanol with a disposable medical syringe with a rubber seal results in a similarly substantial residue. The spectra resulting from contact with the syringe bear strong resemblance to spectra measured from monolayers of poly(dimethylsilane) suggesting the presence of degraded or incompletely polymerized polysiloxane rubber.[18] The medical syringe experiment was not performed using isopropanol.

4.4. Conclusion

Strong solvents can be used to clean optics effectively. However, that same solvent strength allows contaminants to be introduced by materials with which the solvents come into contact. Here it was shown that acetone and methanol quickly become contaminated enough from exposure to LDPE, HDPE and rubber to leave a persistent residue on a fused silica surface. Isopropanol leaves a residue on its own, which worsens after exposure to LDPE, and potentially HDPE and rubber. In the case of LDPE, 1 h of exposure is sufficient to leave a film that can saturate the surface. HDPE is more resistant to solvent, but may also leave a saturated contaminant film on fused silica after 2 weeks of exposure to solvent. In the case of rubber, 5 s of exposure is sufficient to leave a saturated layer of contaminant on a fused-silica optic. With the exception of isopropanol, if the solvents are not contaminated during storage, they leave minimal residue. It should be pointed out, however, that in this experiment the surfaces exposed to the solvents were already clean. Therefore, the results do not speak to the solvents' ability to remove debris from an optic, but only to their tendency to become contaminated during storage.

This work indicates that when using strong solvents to clean optics, it is essential that these solvents come in contact with glass only. Even the use of bottles capped by a glass medicine dropper is not advised, due to the risk of the bottle being unwittingly inverted or of the solvent vapor extracting contaminants over time. Based on these results, the best practice is to store solvents for optics cleaning in a glass container with a glass stopper, and to use a long, disposable glass pipette to transfer the solvent to lens paper or the optic to be cleaned.

4.5 References

1. Coetzee, J. F. and Chang, T.-H., "International Union of Pure and Applied Chemistry, Analytical Chemistry Division, Commission on Electroanalytical Chemistry. Recommended Methods for the Purification of Solvents and Tests for Impurities, Acetone," *Pure & Appl. Chem.* **1986,** 58(11), 1541–1545.

2. Agilent Technologies, Inc., "Solvents: Analysis of impurities in acetone," https://www.agilent.com/cs/library/applications/A00170.pdf.

3. Wahl, K. L.; Wahl, J. H.; Wahl, J. H.; and Bolz, C. D., "Investigating Solvent Purity Using Comprehensive Gas Chromatography: A Study of Acetones," *LCGC Europe* **2010,** 23(4).

4. Guella, G.; Ascenzi, D.; Franceschi, P.; and Tosi, P., "The intriguing case of organic impurities contained in synthetic methanol: a mass spectrometry based investigation," *Rapid Commun. Mass Spectrom.* **2007,** 21, 3337–3344.

5. Agilent Technologies, Inc. "Solvents: Analysis of impurities in pharmaceutical grade isopropanol," http://www.agilent.com/cs/library/applications/A01419.pdf.

6. Ibeh, C. C., Thermoplastic Materials: Properties, Manufacturing Methods, and Applications (CRC Press, 2011).

7. Allen, N.S. and Edge, M., Fundamentals of Polymer Degradation and Stabilization (Springer Science & Business Media, 1992).

8. Andersson, T.; Stålbom, B.; and Wesslén, B., "Degradation of polyethylene during extrusion. II. Degradation of low-density polyethylene, linear low-density polyethylene, and high-density polyethylene in film extrusion," *J. Appl. Polym. Sci.* **2004,** 91, 1525–1537.

9. Fasano, E.; Bono-Blay, F.; Cirillo, T.; Montuori, P.; and Lacorte, S., "Migration of phthalates, alkylphenols, bisphenol A and di(2-ethylhexyl)adipate from food packaging." *Food Control* **2012,** 27, 132–138.

10. Miranda, P. B. and Shen, Y. R., "Liquid Interfaces: A Study by Sum-Frequency Vibrational Spectroscopy," *J. Phys. Chem. B* **1999,** 103, 3292–3307.

11. Brindza, M. R.; Ding, F.; Fourkas, J. T.; and Walker, R. A. "N-Alkane Adsorption To Polar Silica Surfaces," *J. Chem. Phys.* **2010,** 132, 114701.

12. Buchbinder, A. M.; Weitz, E.; and Geiger, F. M. "Pentane, Hexane, Cyclopentane, Cyclohexane, 1-Hexene, 1-Pentene, cis-2-Pentene, Cyclohexene, and Cyclopentene at Vapor/α-Alumina and Liquid/α-Alumina Interfaces Studied by Broadband Sum Frequency Generation," *J. Phys. Chem. C* **2010,**114, 554–566.

13. Esenturk O. and Walker, R. A. "Surface Structure at Hexadecane and Halo-hexadecane Liquid/Vapor Interfaces," *J. Phys. Chem. B* **2004,** 108, 10631–10635.

14. Lu, R.; Gan, W.; Wu, B.; Chen, H.; and Wang, H., "Vibrational Polarization Spectroscopy of CH Stretching Modes of the Methylene Group at the Vapor/Liquid Interfaces with Sum Frequency Generation," **2004,** *J. Phys. Chem. B* 108, 7297–7306.

15. Zhang, D.; Shen Y.; and Somorjai, G., "Studies of surface structures and compositions of polyethylene and polypropylene by IR + visible sum frequency vibrational spectroscopy." *Chem. Phys. Lett.* **1997,** 281, 394–400.

16. Sheftel, V. O. Indirect Food Additives and Polymers: Migration and Toxicology (CRC Press, 2000).

17. Carver, C. D. editor, The Coblentz Society Desk Book of Infrared Spectra, Second Edition (The Coblentz Society:Kirkwood, MO, 1982).

18. Kim, C.; Gurau, M. C.; Cremer, P. S.; and Yu, H., “Chain conformation of poly(dimethyl siloxane) at the air/water interface by sum frequency generation,” *Langmuir* **2008**, 24, 10155–10160.

Chapter Five: Reorientation-Induced Spectral Diffusion in Vibrational Sum-Frequency-Generation Spectroscopy

Adapted from: Rivera, C.A.; Souna, A. J.; Bender, J. S.; Manfred, K.; Fourkas, J. T. *J. Phys. Chem. B*, 2013, 117(49), 15875-15885.
VSFG spectroscopy research designed and conducted by: Christopher A. Rivera, Katherine Manfred, and Amanda J. Souna
Simulations performed by: Amanda J. Souna, John S. Bender, and John T. Fourkas
Authored by: Christopher A. Rivera and John T. Fourkas

5.1 Introduction

Although VSFG is typically used to study the average molecular orientation at interfaces, there is a growing appreciation that this technique can also provide information on dynamics.[8] For instance, in 2001 Wei and Shen showed that reorientation can influence the relative VSFG intensity of the free O-H stretch at the water liquid/vapor interface under different polarization conditions.[2] This effect has since been observed in other systems,[3-6] analyzed theoretically,[1,3] and quantified using molecular dynamics simulations.[7] Higher-order, surface-selective techniques have also been devised to study reorientational dynamics at interfaces more directly.[8-16]

A broadband implementation of VSFG spectroscopy can be described in terms of a vibrational coherence that is created with an infrared pulse (IR) and is later probed with a shorter-wavelength pulse via a Raman transition.[1,3,7] The IR pulse preferentially creates coherences in a subset of the interfacial molecules, based on their orientations. Previous work on the effects of reorientation on VSFG spectra has focused on how the orientational evolution of the distribution of molecules initially excited influences the signal by changing the sensitivity of the probing step.[2,3,7] The influence of reorientation on other molecular properties has not been considered in these treatments.

A vibrational mode of a high-symmetry functional group, such as a freely-rotating methyl group, has a Raman tensor that can be described in terms of an isotropic portion and an anisotropic (depolarized) portion.[15] The isotropic portion of the polarizability is independent of the orientation of the functional group, and so is not influenced by any reorientation that occurs following creation of a vibrational coherence with the infrared pulse. Thus, in the absence of other orientation-dependent effects, only the depolarized component of the Raman tensor plays a role in coupling orientational dynamics to VSFG spectra.[3,7] For a symmetric methyl stretch, the isotropic portion of the polarizability is typically significantly larger than the depolarized portion,[16-19] and so even rapid reorientation has been found to have little effect on the VSFG spectrum.[7]

In the above picture, it is assumed that the vibrational frequency of the mode of interest remains the same regardless of orientation. However, the dielectric environment often changes rapidly as a function of distance from an interface.[20] In such a situation, the vibrational frequency becomes a function of orientation for interfacial molecules. Thus, reorientation can cause the frequency of a vibration to vary as a function of time. A transition frequency that varies on a time scale that is longer than the oscillation period of the transition (λ/c) is a characteristic feature of spectral diffusion.[21,22] The orientation-dependent vibrational frequency therefore can lead to what we term reorientation-induced spectral diffusion (RISD).

Coupling between frequency and orientation has the potential to allow reorientation to have a substantial influence on VSFG spectra, because this phenomenon is operative for both the depolarized and the isotropic portions of the

Raman tensor. Here I explore the role of reorientation-induced spectral diffusion in the VSFG spectrum of a model system, liquid acetonitrile at the liquid/silica (LS) interface. Acetonitrile takes on a lipid-bilayer-like structure at this interface.[23-27] The cyanide groups in the first sublayer of molecules interact strongly with the silica surface, and molecules in this sublayer therefore undergo reorientation on a time scale that is much longer than that of vibrational dephasing. In the second sublayer the methyl groups tend to point towards the first sublayer, and are therefore in a relatively nonpolar environment.[23-27] However, some molecules in the second sublayer have methyl groups that point away from the first sublayer, and are therefore in a more polar environment. Due to the absence of hydrogen bonding in the second sublayer, reorientation is considerably faster than in the first sublayer,[27] suggesting that it could be possible to observe RISD in the contribution of the second sublayer to the VSFG spectrum of the symmetric methyl stretch.

Here I present a time-resolved, broadband VSFG study of acetonitrile at the LS interface. The shape of the peak from the symmetric methyl stretch evolves as a function of time after the infrared pulse creates a vibrational coherence. Line shape simulations based on the characteristics of the infrared and probe pulses used demonstrate that this evolution cannot be explained in terms of static spectral features. However, the essential features of the spectral evolution can be reproduced with a basic model of RISD based on an orientational distribution for the second sublayer that is derived from previous simulations.[25]

5.2. Experimental

The details of our counterpropagating VSFG spectrometer have been described in Chapter Three. For the studies reported here the probe bandwidth was narrowed to ~5 cm^{-1} (0.3 nm). The probe spectrum used for the experiments reported here was centered at 801.2 nm. For this study we are concerned primarily with the *SSP* polarization combination. At the sample, the probe pulse energy was 11 μJ, and the IR pulse energy was 8 μJ. The spectra of the probe pulse and the VSFG signal were measured using a spectrometer (Acton SP300i) with a thermoelectrically-cooled, 2D CCD array (Spec-10:100, Roper Scientific).

The sample consisted of 99+% spectroscopic grade acetonitrile (ACROS) and was held in an IR-grade quartz cell with a 1 mm path length (Hellma). The cell was rinsed, oven-dried and oxygen-plasma cleaned immediately prior to use. The SFG spectrum of gold under *PPP* polarization conditions, which is proportional to the spectrum of the IR pulse,[28] was used as a reference. The VSFG signal was divided by the gold SFG spectrum to obtain the corrected line shape. IR/probe delays ranging between 0 and 3.5 ps, with a 0.167 ps step-size, were used to collect VSFG spectra that sampled different portions of the vibrational free-induction decay (FID). Time zero was determined carefully by maximizing of the gold SFG signal using the full bandwidth of the probe pulse (which had a temporal FWHM of ~100 fs).

5.3. Results

5.3.1 The molecular origin of RISD

To illustrate the potential influence of RISD on VSFG spectra, consider a completely symmetric vibration (such as the symmetric stretch of a freely-rotating

methyl group) under *SSP* polarization conditions. In the absence of RISD, the response function for this situation is given by[7]

$$R_{xxz}^{(2)}(\tau) \propto \mu_Z' \alpha_I' \langle \cos\theta \rangle + \mu_Z' \alpha_A' \left(\frac{1}{12} \langle \cos\theta \rangle + \frac{1}{4} \langle \cos\theta \cos 2\Theta \rangle \right), \tag{5.1}$$

where τ is the time between the IR and Raman transitions, θ and Θ are the angles of the symmetry axis with respect to the surface normal at times zero and τ, respectively, μ_Z' is the component of $(\partial \boldsymbol{\mu}/\partial q)\, q_0$ along the symmetry axis (where $\boldsymbol{\mu}$ is the dipole moment, q is the vibrational coordinate and q_0 is its equilibrium value), α_I' and α_A' are the isotropic and anisotropic components of $(\partial \boldsymbol{\alpha}/\partial q)\, q_0$, respectively (where $\boldsymbol{\alpha}$ is the polarizability tensor), and the angular brackets indicate ensemble averages.

Only the term in Eq 5.1 containing the anisotropic portion of the polarizability is influenced by reorientation. To illustrate why this is the case, Figure 5.1 shows how a resonant IR field influences the dipole and polarizability tensors of molecules parallel, perpendicular, and antiparallel to the instantaneous direction of the field. We assume that if the field causes the bonds in the methyl group to stretch (here illustrated by expansion of the methyl group), then the polarizability grows as well. In the case illustrated, the anisotropic portion of the polarizability shrinks along the symmetry axis and grows perpendicular to the symmetry axis as the methyl group expands. The opposite situation occurs when the field causes the bonds in the methyl group to contract. When the methyl symmetry axis is perpendicular to the field, the dipole moment and polarizability are unaffected. The methyl groups cycle through all of these states following coherent excitation, and the phase of the oscillation on a given methyl

group depends on its initial orientation relative to the electric field direction at the time of creation of the vibrational coherence.

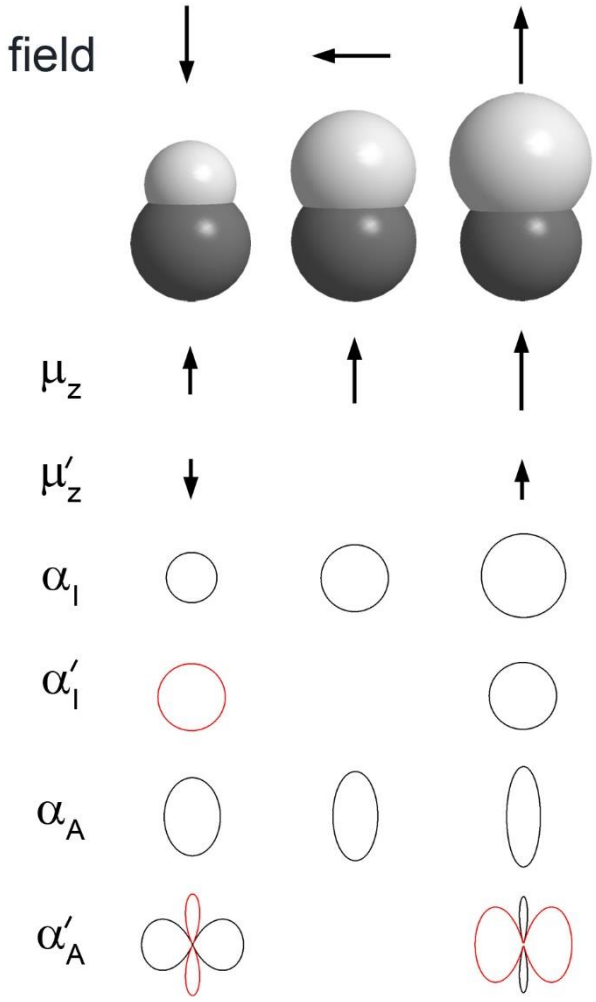

Figure 5.1. The dependence of the IR transition dipole and the isotropic and anisotropic portions of the polarizability tensor on the instantaneous direction of a resonant IR field for a totally symmetric vibrational mode as a function of initial orientation. The plots of the changes in dipole and polarizability are not on the same scale as the other plots. In the plots of changes in the portions of polarizability tensor, red denotes a negative change and black denotes a positive change.

Figure 5.2a is a schematic depiction of molecules at an arbitrary interface at the time of excitation, and Figure 5.2b is a depiction of the same molecules after enough time has elapsed for diffusive randomization of orientation to occur. Methyl groups that initially pointed towards the interface are colored red, methyl groups that initially

pointed away from the interface are colored blue, and methyl groups that were initially parallel to the interface are white. These colors can be mapped to the phase of the oscillations of the isotropic and anisotropic portions of the polarizability.

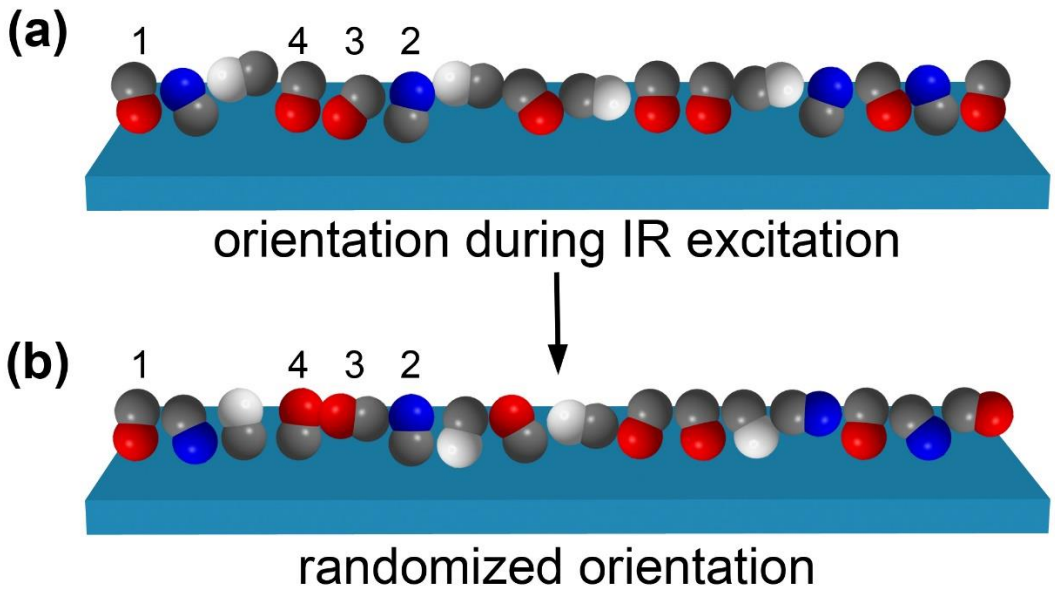

Figure 5.2. Schematic depiction of interfacial molecules with a totally symmetric vibrational mode at the initial time that a vibrational coherence is created (a) and after the molecular orientations have randomized completely via orientational diffusion (b). Red groups initially pointed toward the interface, blue groups initially pointed away from the interface, and white groups initially pointed roughly parallel to the interface. See text for a discussion of the molecules labeled 1 through 4.

First consider the case in which the vibrational frequency is independent of orientation. In this situation, the isotropic portion of the polarizability is the same regardless of the orientation of the molecules, and so its average value at the interface is determined solely by the orientations of the molecules when a vibrational coherence was created via an IR transition. Thus, the isotropic portion of the polarizability is identical in the configurations shown in Figures 5.2a and 5.2b, and so reorientation has no influence on this portion of the VSFG response. The anisotropic part of the

polarizability does depend on orientation, and so this portion of the VSFG response does differ between the configurations shown in Figures 5.2a and 5.2b. For instance, molecule 1 in Figure 5.2 has its methyl group pointing towards the interface both when the vibrational coherence is created and at the later time illustrated in Figure 5.2b, so it will contribute to the signal with the same Raman phase at both times. Molecule 2 has its methyl group pointing away from the interface in both configurations, and so will contribute with the opposite Raman phase of molecule 1 at both times. Molecule 3 has its methyl group pointing towards the interface initially, but in the second configuration it is parallel to the interface. As a result, the Raman phase of this molecule in the second configuration is opposite of its phase when the coherence was created. Indeed, the fact that the two principal axes of α'_A are always of opposite sign is responsible for the cos2Θ term in the time correlation function in Eq. 5.1. Molecule 4 points towards the interface initially, and away from the interface in the second configuration. Because the polarizability tensor is centrosymmetric, reorientation by 180° does not influence the Raman phase or the magnitude of the contribution to the anisotropic polarizability. Despite the presence of these effects for the anisotropic portion of the polarizability, the fact that the *SSP* response is considerably more sensitive to the isotropic portion of the Raman polarizability than to the anisotropic portion means that even rapid reorientation tends to have a minor effect on this VSFG response for totally symmetric modes.

Now consider a situation in which the frequency of the mode depends on the molecular orientation. Such a scenario can arise naturally at an interface, because the dielectric properties of a liquid vary as a function of distance from the interface. Under

these circumstances, both the Raman phase and frequency of oscillation of a given molecule depend on both its initial orientation and its trajectory following creation of the vibrational coherence. For instance, molecule 4 in Figure 5.2 points towards the interface at the time of creation of the coherence, but away from the interface at the time of probing. This molecule will therefore have a different frequency at the time it is probed than it did when the coherence was generated. This effect holds for both the anisotropic and isotropic portions of the polarizability. Furthermore, the phase of the vibration at the time of probing depends on its orientational history. For instance, a molecule in which the methyl group points towards the interface until just before the probing step will have a different phase than a molecule that reorients to point away from the interface immediately after creation of the coherence and remains in that orientation until the probing step. Thus, reorientation is a dephasing mechanism even for the portion of the VSFG signal that arises from the isotropic portion of the polarizability tensor in this situation.

5.3.1 RISD in a model system

To assess the potential role of RISD in a real system, we consider acetonitrile at the LS interface. As discussed above, this liquid takes on a lipid-bilayer-like structure at this interface.[23-27] The first (surface) sublayer accepts hydrogen bonds from interfacial silanol groups, and so is relatively orientationally immobile.[25,27] The organization of the second sublayer is driven primarily by interactions with the methyl groups of the molecules in the first sublayer, i.e. the methyl groups in the second sublayer tend to point towards the interface. However, there are no additional constraints on the molecules in the second sublayer, and so tumbling reorientation can

occur much more quickly than in the first sublayer.[25,27] The dielectric environment of molecules in the second sublayer that have methyl groups pointing towards the interface is dominated by other alkyl groups. On the other hand, cyanide groups make a substantial contribution to the dielectric environment for molecules in this sublayer with methyl groups that point away from the interface. The combination of relatively fast reorientation and a dielectric environment that varies substantially as a function of distance from the interface indicates that RISD could be of importance in this system.

To assess the potential impact of RISD on the VSFG spectrum of acetonitrile at the LS interface, we use the orientational distribution for the second sublayer determined in the simulations of Hu and Weeks.[25] The distribution of methyl group orientations for center-of-mass distances from the interface between 1.2 Å and 3.0 A is shown in polar form in Figure 5.3a. As expected for a lipid-bilayer-like structure, the majority of the methyl groups point towards the interface, although a significant number of methyl groups also point in the opposite direction.

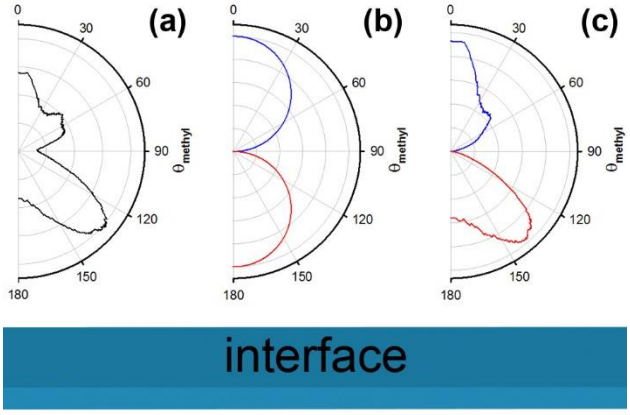

Figure 5.3. (a) Orientational distribution of methyl groups in the second sublayer of acetonitrile at the LS interface based on the simulations of Hu and Weeks, ref. 33. (b) Distribution of vibrational coherences created by a *P*-polarized excitation pulse. Red and blue denote opposite phases. (c) Product of the functions in (a) and (b), which indicates the initial distribution and phase of the vibrational coherences in the sublayer.

For an *SSP* spectrum, the initial orientational distribution of molecules with vibrational coherences is given by the product of the orientational distribution of all molecules with the $|\cos\theta|$ probability of creating a coherence. The excitation probability is shown in Figure 5.3b, and the distribution of coherences is shown in Figure 5.3c. The color coding gives the phase of the excitation/coherence, and matches that used in Figure 5.2.

The transition frequency of the symmetric methyl stretch is likely to be a continuous, monotonic function of θ. However, to assess the essential impact of RISD, we consider a simpler model in which the transition frequency depends only on whether the methyl group points toward or away from the interface. The methyl groups that point towards the interface are assumed to have a lower symmetric stretching frequency than the methyl groups that point away from the interface. The line shape for each population is assumed to be Lorentzian, so the overall VSFG lineshape is given by

$$I(\omega) \propto \left| \frac{A_1}{(\bar{\nu} - \bar{\nu}_1) + i\Gamma_1} + \frac{A_2}{(\bar{\nu} - \bar{\nu}_2) + i\Gamma_2} \right|^2, \qquad (5.2)$$

where A_n, $\bar{\nu}_n$ and Γ_n are the amplitude, center frequency and damping constant, respectively, of Lorentzian n. We use the subscript 1 to denote the methyl groups that point toward the interface and the subscript 2 to denote the methyl groups that point away from the interface.

Based on the distribution in Figure 5.3c, at the time of the creation of the vibrational coherence the ratio of amplitudes is A_1/A_2 = -1.53, where we use the convention that A_1 is positive. When orientational relaxation is complete, all memory of the orientation at the time of creation of the coherence has been lost. Thus, at this

point the populations of methyl groups that were initially pointing toward and away from the interface each take on the distribution shown in Figure 5.3a. At the time of the creation of the vibrational coherence, approximately 60% of the excited methyl groups point toward the interface. Thus, after orientational randomization, ~60% of the excited methyl groups pointing toward the interface pointed that way originally, and ~60% of the excited methyl groups pointing away from the interface pointed toward it originally. The ratio of amplitudes once orientations have randomized is thus $A_1/A_2 = 1.63$. The majority of methyl groups pointing toward the interface at any time were pointing that direction at the time of the creation of the vibrational coherence, so A_1 never changes sign. The methyl groups pointing away from the interface are initially dominated by the population that pointed that direction at the time of the creation of the vibrational coherence. Ultimately, however, the majority of the methyl groups that point away from the interface were initially pointing towards the interface. Therefore, A_2 must change sign from negative to positive as orientational relaxation proceeds.

Rather than assuming a particular orientational correlation function, we assume that A_1 and A_2 both change from their initial values to their final values with the same time dependence. The degree of relaxation of the populations can therefore be defined without implying a specific time dependence for this relaxation. The properties of the simulated line shape will be investigated as a function of this degree of relaxation.

For the simulated spectra, Γ_1 and Γ_2 were both set to 6 cm^{-1}. $\bar{\nu}_1$ was fixed at 2940 cm^{-1}, and the effect of $\Delta\bar{\nu} = \bar{\nu}_2 - \bar{\nu}_1$ on the simulated spectra was explored as a function of the degree of relaxation. Three representative cases ($\Delta\bar{\nu}$ = 1 cm^{-1}, 3 cm^{-1} and 5 cm^{-1}) are plotted in Figure 5.4. In each case, there is a clear peak shift to the blue

as the degree of relaxation increases. This shift occurs because the ratio of A_1 to A_2 becomes a larger negative number as relaxation proceeds, and then changes sign and begins to decrease when the relaxation is approximately 83% complete. There is also a clear broadening of the spectrum and an increase in its asymmetry as relaxation proceeds. The larger the value of $\Delta\bar{\nu}$, the more obvious the broadening and asymmetry become. Note that the scaled shape of the simulated spectrum depends only on the ratio of the damping constants to $\Delta\bar{\nu}$. For instance, the shape for $\Gamma_1 = \Gamma_2 = 6$ cm^{-1} and $\Delta\bar{\nu}$ = 2 cm^{-1} is the same as the shape for $\Gamma_1 = \Gamma_2 = 3$ cm^{-1} and $\Delta\bar{\nu} = 1$ cm^{-1}, but the latter spectrum is half as broad.

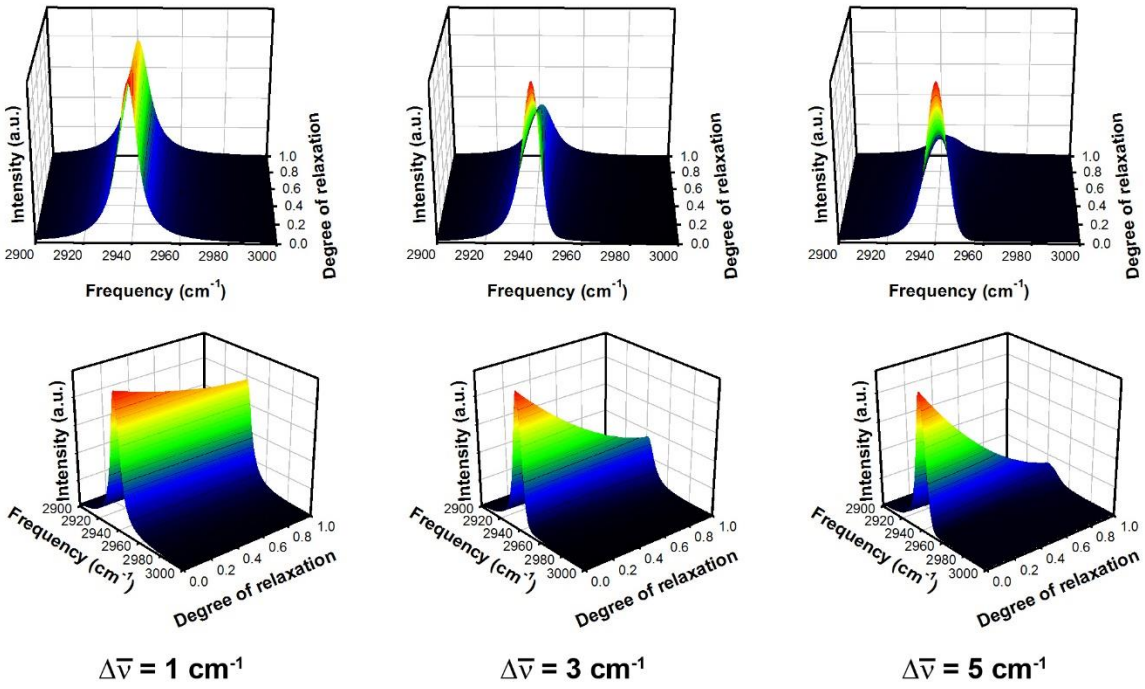

Figure 5.4. Influence of RISD on a simulated VSFG spectrum of the second sublayer of acetonitrile at the LS interface for different values of the separation between the peaks of the two Lorentzians. The top and bottom rows are different views of the same 3D plots.

To get a more quantitative sense of how the spectra vary with relaxation, the peak shift, peak height, and full width at half maximum (FWHM) are plotted in Figure

5.5 as a function of relaxation for six different values of $\Delta\bar{\nu}$ ranging from 1 cm^{-1} to 6 cm^{-1}. The peak shift is defined as $\bar{\nu}_{max} - (\bar{\nu}_2 + \bar{\nu}_1)/2$, where $\bar{\nu}_{max}$ is the frequency at which the peak reaches its maximum height. The peak height of each $\Delta\bar{\nu}$ set is scaled to the peak height in the absence of relaxation for the case of $\Delta\bar{\nu}$ = 6 cm^{-1}.

A number of interesting trends are evident in Figure 5.5. As relaxation approaches completion, the peak shifts to the blue regardless of the value of $\Delta\bar{\nu}$. However, early in the relaxation the peak shift depends strongly on $\Delta\bar{\nu}$. For $\Delta\bar{\nu}$ = 1 cm^{-1}, the shift is to the blue for all degrees of relaxation. As $\Delta\bar{\nu}$ increases, the shift is initially to the red before going to the blue. The larger the value of $\Delta\bar{\nu}$, the later in the relaxation process that the shift changes to blue. For low values of $\Delta\bar{\nu}$, the interference between the two Lorentzians is strong before relaxation occurs, and so the peak height increases with relaxation before eventually decreasing. As $\Delta\bar{\nu}$ increases the interference between the Lorentzians decreases, and so the peak height decreases monotonically with relaxation. Finally, the FWHM increases with relaxation regardless of the value of $\Delta\bar{\nu}$. However, once the ratio A_1/A_2 becomes positive, larger values of $\Delta\bar{\nu}$ lead to substantially greater broadening.

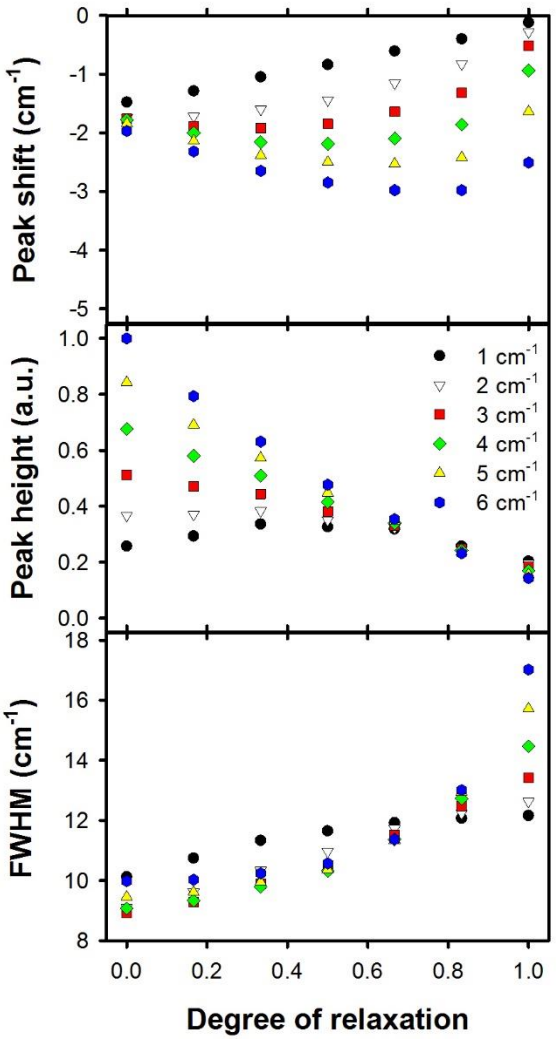

Figure 5.5. Influence of RISD on the peak shift (top), relative peak height (middle) and FWHM (bottom) for simulated VSFG spectra for the second bilayer of acetonitrile at the LS interface for different values of the separation between the peaks of the two Lorentzians.

It is clear from this basic model that RISD can have a substantial impact on the time dependence and overall appearance of the VSFG spectrum. It should be stressed that this model does not include dephasing caused by RISD, which will lead to even more broadening as relaxation proceeds. Additionally, the influence of population relaxation and other dephasing mechanisms has not been included. These effects can compete with RISD, and may in some cases limit the ability to observe some of its

effects. Nevertheless, it is clear that RISD in this system could lead to observable effects such as a time-dependent blue shift and broadening of the observed peak.

5.3.3 Experimental results for the acetonitrile LS interface

SSP VSFG spectra of neat acetonitrile at the LS interface for IR/probe delays τ ranging from 0 to 3.5 ps are shown in Figure 5.6. The spectral resolution is approximately 5 cm^{-1}. Although VSFG spectra for this system has been presented previously,[26,29] these are the first data reported that have either this high of a frequency resolution or are time-resolved. Due to the high spectral resolution and the importance of explicit consideration of the temporal delay between the IR and probe pulses, a line shape model based on a sum of two Lorentzian features is no longer adequate for fitting the spectra. Instead, a more rigorous model must be employed that takes into account the temporal overlap of the probe field with the vibrational FID. However, as an initial step it is still instructive to examine the spectral evolution in more general terms.

The spectra in Figure 5.6 are shown on both relative and normalized intensity scales. Several trends are evident in the time evolution of the line shape. The dashed red curve in the top panel of Figure 6 illustrates the time dependence of $\bar{\nu}_{max}$ and the overall intensity of the peak. As is apparent from this curve, the overall intensity of the spectrum increases over the first 0.5 ps of time delay and then decreases monotonically. The initial rise in intensity results from two different phenomena. First, the fraction of the probe pulse that arrives after the IR pulse increases as τ becomes larger. Second, oppositely-phased contributions to the peak exhibit maximum interference at zero delay time. The decrease in intensity at longer delay times arises from dephasing of the vibrational coherence. The dashed red line in the upper panel of Figure 5.6 also

reveals that there is a blue shift in $\bar{\nu}_{max}$ as τ increases. The rate of this spectral shift increases substantially at delay times greater than 2 ps. As will be seen below, a peak shift can occur in the absence of RISD, but only at relatively short delay times.

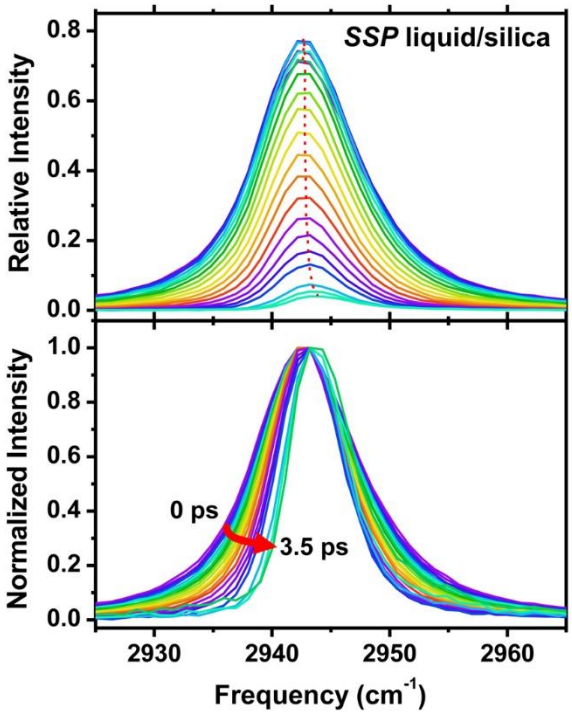

Figure 5.6. Experimental acetonitrile VSFG spectra at the LS interface with values of τ ranging from 0 ps to 3.5 ps. The spectra were obtained under *SSP* polarization conditions and are plotted with relative (top) and normalized (bottom) intensity scales. The dashed red curve in the upper panel illustrates the time dependence of the frequency at which the spectrum has its maximum intensity. There is a clear spectral blue shift of this frequency with increasing delay time.

The normalized plots in Figure 5.6 further reveal that there is significant spectral narrowing over the first 3 ps of delay. For delays greater than 3 ps a slight broadening is observed, especially on the high-frequency side of the spectrum. The overall narrowing of the line shape with increasing delay time is a consequence of the convolution of the probe pulse with the decaying molecular response. However, the spectral broadening at longer decay times is indicative of dynamic behavior in the molecular response.

Finally, the line shape develops a clear asymmetry at longer delay times. For VSFG spectra at a constant delay time, this phenomenon has previously been attributed to the line shape consisting of two Lorentzian features of opposite phase with different center frequencies and widths.[26,29] Asymmetry in VSFG line shapes has also been associated with contributions from non-resonant background (NRB).[30] NRB typically arises from an instantaneous electronic response that occurs at the time of IR excitation, and thus should have the most significant impact on line shapes at early delay times, when the IR and probe pulses have maximal overlap. Even at a zero delay time, a benefit of the counterpropagating geometry used here is that the spatial overlap in the bulk of the sample (from which the majority of the NRB arises) is greatly reduced as compared to that in a copropagating geometry. The spectra presented here have not been subjected to any background subtraction, smoothing or averaging. The fact that the baseline is independent of τ indicates that any NRB is minimal in comparison to the resonant signal, even at short delay times.

5.3.4 Modeling of time-dependent VSFG line shapes

It is clear from the data in Figure 5.6 that the VSFG line shape depends strongly on τ. At short delay times the line shape is more symmetric and broader than it is at longer delay times. A number of phenomena could contribute to the time dependence of the line shape. First, the fact that the probe pulse has a duration that is comparable to the dephasing time of the vibration leads to an inherent time dependence in the line shape, as different delays lead to spectra that effectively sample different portions of the vibrational FID.[30,31] Second, any asymmetry in the spectrum of the probe pulse

could influence the asymmetry of the line shape at longer delay times. Finally, RISD could give rise to these effects.

To distinguish among the possible contributions to the time dependence of the VSFG line shape, it is necessary to model the VSFG spectrum in terms of an underlying spectral shape that is influenced by the spectral envelopes of the IR and probe pulses, as well as by the delay time between them.[30,31] Such a model inherently accounts for the first two contributions to the time-dependent line shape discussed above. Because both the IR and probe pulses are Fourier-transform-limited in our experiments, such a model can accurately capture the contributions of these phenomena to the VSFG line shape.

We begin by defining the three time-domain optical functions: (a) the electric field of the IR excitation pulse, $E_{IR}(t)$; (b) the electric field of the probe pulse, $E_{probe}(t - \tau)$; and (c) the molecular response $R(t - \tau)$. $E_{IR}(t)$ is centered at $t = 0$, whereas the peak of the probe pulse is delayed by a time τ relative to $E_{IR}(t)$. These functions can be Fourier transformed into the frequency domain to obtain the corresponding frequency-domain representations. The magnitude squared of the frequency-domain electric field of a pulse yields the simulated spectrum. By measuring the experimental IR and probe spectra and comparing them to the modeled spectra, we are able to choose the appropriate time-domain parameters to describe each. A single Gaussian was found to reproduce the gold *PPP* spectrum accurately in the acetonitrile C-H stretching region (2900 cm^{-1} to 3000 cm^{-1}). The probe spectrum has a slight tail, and requires two Gaussian features to be represented accurately. The molecular susceptibility model consisted of one or more Lorentzian features, the parameters of which were allowed to

vary with τ. Susceptibilities were examined consisting of one, two and three Lorentzian features with varying phase, center frequency and bandwidth.

Once pulses are defined in the time domain and transformed into the frequency domain, the magnitude of the product of $R(\bar{\nu})$ and $E_{IR}(\bar{\nu})$ is back-transformed to produce the first-order polarization $P^{(1)}(t)$. This function is then convolved with the probe pulse to produce the second-order polarization $P^{(2)}(t, \tau)$. The Fourier transform of this function yields a frequency-domain field, $E_{signal}(\bar{\nu}, \tau)$, which is related to the VSFG spectral intensity by

$$I_{\text{signal}}(\bar{\nu}, \tau) \propto \left| E_{\text{signal}}(\bar{\nu}, \tau) \right|^2 . \tag{5.3}$$

When the IR and probe fields are set, $I_{signal}(\bar{\nu}, \tau)$ depends only on the input parameters of the molecular response and the delay between the IR and probe pulses. A more complete description of the equations can be found in section 2.4.2 of Chapter Two. The parameters used to model the IR pulse using equation 2.28 were: $A_{\text{IR}} = 1$, $\tau_{\text{IR}} = 60$ fs, $\nu_{\text{IR}} = 2952$ cm^{-1}. The parameters used to model the visible probe using equation 2.29 were: $E_1 = 1.0$, $\tau_1 = 2200$ fs, $\nu_1 = 12501.4$ cm^{-1} and $E_2 = 0.8$, $\tau_2 = 1100$ fs, and $\nu_2 = 12503.9$ cm^{-1}.

Construction of this simulated VSFG spectrum allows us to examine key aspects of the temporal evolution of the line shape. We can further perform fits of the experimental spectra by varying the form of the molecular response, and can also simulate the spectral evolution arising from a susceptibility that is described by a static set of parameters, such that the only time dependence arises from dephasing related to the natural line widths of the transitions.

To perform fits using the line shape model, the Levenberg-Marquardt nonlinear least-squares method[32,33] was used to determine the best fits to the experimental spectra at delays of 0.5 and 1.5 ps with a second-order susceptibility composed of either one Lorentzian peak, two Lorentzian peaks or three Lorentzian peaks. The nonlinear least-squares fits and residuals for each model, shown in Figure 5.7, clearly show that a single Lorentzian does not adequately reproduce the line shape that we observe at either delay. In the best two-Lorentzian fits, each peak has opposite phase. In the best three-Lorentzian fits, the phases of the two peaks at highest frequency are opposite to the phase of the lowest-frequency peak. Although the two- and three-Lorentzian fits are clearly superior to the single-Lorentzian fits, none of these fits reproduces the line shape well in the wings. It is further clear that asymmetry in the probe pulse cannot account for the majority of the delay-dependent spectral changes observed experimentally.

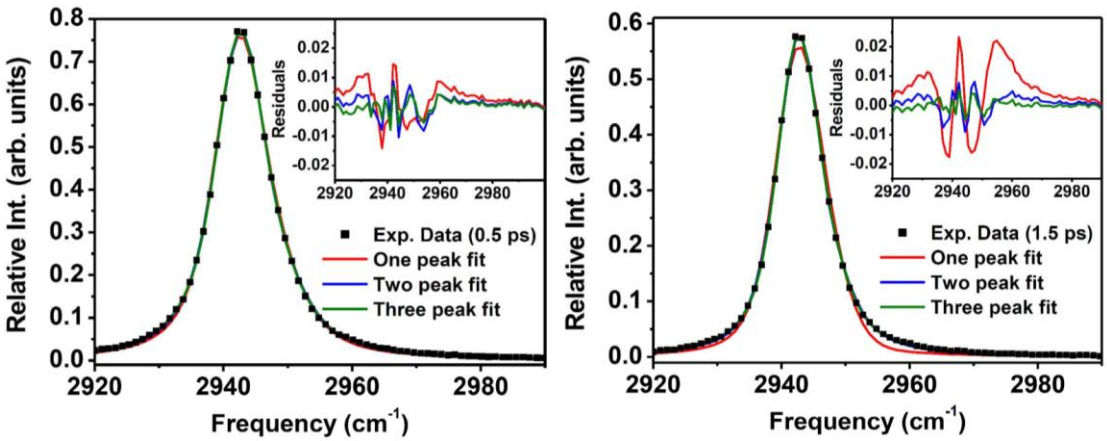

Figure 5.7. Examples of simulated fits of the 0.5 (left) and 1.5 ps (right) experimental data (black squares) using one peak (red), two peaks with opposite phase (blue) and three peaks (green) and the resulting residual plots (inset). Both the two and three peak simulated fits result in small residual values while one peak clearly fails to reproduce the experimental lineshape. The relative phases of the peaks in the 0.5-ps best fit were -, +, - while in the 1.5-ps model they were -, +, +.

This model does not include any inhomogeneous broadening, which is almost certainly present because a bilayer presents different local environments within each sublayer. The only broadening in the model comes from homogeneous processes as well as from the probe pulse. Note that changing the temporal overlap of the FID with the probe pulse also leads to spectral narrowing at large delay times.[30] Thus, fits from this model represent a lower bound for peak separation and bandwidth. Conversely, fits without the convolution give an upper bound for these parameters. For example, the best fit parameters for the 0.5-ps experimental delay to two Lorentzians give a peak splitting of 1.3 cm^{-1} and peak bandwidths of 2.9 and 2.6 cm^{-1}. A recently published, unconvolved, two-Lorentzian fit of the pure LS *SSP* spectrum at a delay time of 667 fs using a significantly broader probe spectrum yielded a splitting of ~10 cm^{-1} and peak bandwidths of 6.0 and 7.2 cm^{-1}.[29] The actual splitting and bandwidths lie somewhere between these limits.

Because both the two- and three-Lorentzian fits are of comparable quality, we examine the line shapes using only the one- and two-Lorentzian models. The fit parameters for the 0.5- and 1.5-ps fits are given in Table 5.1. Neither model provides fits that are of equal quality at both delay times using the same underlying line shape, which suggests that this line shape is dynamic. To illustrate this effect, both the one- and two-Lorentzian parameters from the 0.5-ps fits were used to generate the VSFG spectrum as a function of the IR/probe delay from 0 to 3.5 ps. The resultant normalized spectra are shown in Figure 5.8. Both simulated sets of spectra are similar. A slight blue shift with increasing τ can be observed in both cases, although the shift is more pronounced in the two-Lorentzian model. Furthermore, the shift occurs at early delay

times, as opposed to the shift at late delay times observed experimentally. This phenomenon is also apparent upon examination of the high-frequency side of the simulated line shapes. Both the one- and two-Lorentzian models decay faster on the high-frequency side of the spectrum than do the normalized experimental data in Figure 5.6.

Table 5.1. Best fit parameters for one- and two-Lorentzian line shape models of the acetonitrile LS *SSP* spectrum at IR/probe delays of 0.5 and 1.5 ps.

	one Lorentzian			two Lorentzians		
τ	$\bar{\nu}$	A	Γ	$\bar{\nu}$	A	Γ
0.5 ps	2941.8	2.3	2.4	2942.9	-4.8	2.9
				2944.2	2.3	2.6
1.5 ps	2941.6	2.1	2.9	2943.7	-6.3	3.2
				2944.4	3.6	2.4

To highlight the differences between the simulated and experimental spectra, the time dependence of the interpolated frequency of the peak maximum ($\bar{\nu}_{max}$) and the full width at half maximum (FWHM) of the peak are compared in Figure 5.9. Both the one- and two-Lorentzian models display a blue shift of $\bar{\nu}_{max}$ over the first 1.5 ps. In the two-Lorentzian model $\bar{\nu}_{max}$ is essentially constant after this time, whereas in the one-peak model $\bar{\nu}_{max}$ shifts back to the red after this time. In contrast, the experimental $\bar{\nu}_{max}$ shifts to the blue slowly at early times, and then considerably more rapidly after about 2.0 ps. The long-time blue shift observed experimentally for $\bar{\nu}_{max}$ is considerably larger than that in either model. In the case of the FWHM, for both of the models and the experimental data a similar monotonic decrease is observed over the initial 3.0 ps. At longer times the FWHM in each simulation continues its monotonic decrease, whereas in the experimental spectra the FWHM increases. It should also be noted that

although it is likely that the underlying static line shape for any real-life system is not likely to be exactly Lorentzian, the essential features of these simulations are consistent for all static line shapes that have been examined, and are likely to hold for virtually any physically reasonable static line shape.

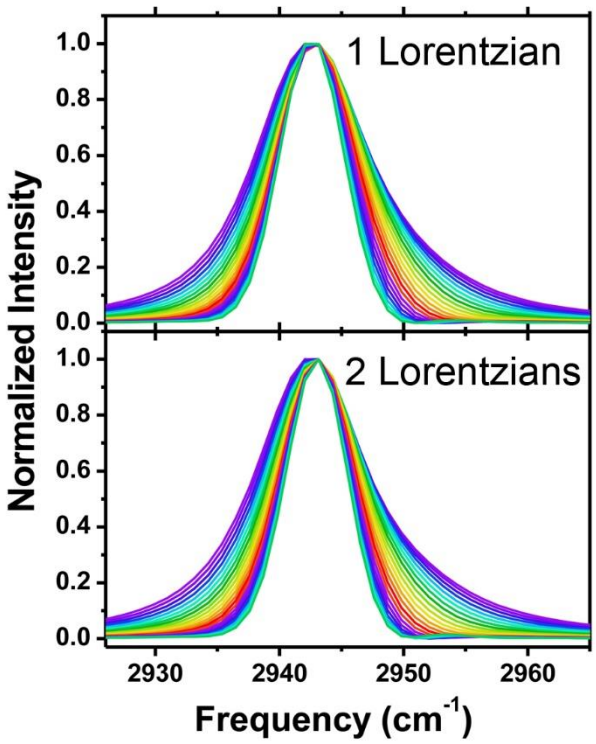

Figure 5.8. Time evolution of spectra simulated by fitting the VSFG spectrum at a 0.5 ps delay using one Lorentzian (top) and two Lorentzians of opposite phase (bottom). Other than some variation in the spectral widths, the time evolution is similar in both cases, and clearly shows that the experimental data cannot be reproduced with a static underlying spectrum.

5.3.5 Comparison of experimental data and the RISD model

Although the simulations above reproduce some of the features of the time dependence of the VSFG spectra, it is clear from Figures 5.6 through 5.9 that models with a static underlying line shape cannot reproduce all of the important aspects of the experimental data. Now consider whether the observations that cannot be explained by the simulations are consistent with the basic RISD model presented above.

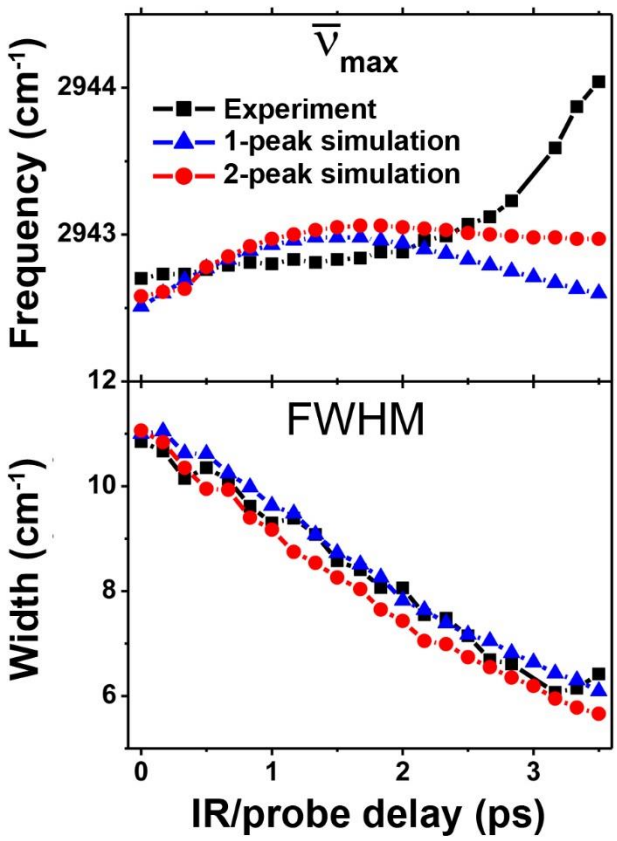

Figure 5.9. Time evolution of the frequency of the peak maximum (top panel) and the half-height frequency of the blue edge of the peak (bottom panel) for the experimental and simulated VSFG spectra of acetonitrile at the LS interface. The behavior of the experimental data at delay times greater than 2.5 cannot be reproduced using a static line-shape model.

First consider the time dependence of $\bar{\nu}_{max}$. At early delay times, $\bar{\nu}_{max}$ has a substantially smaller rate of blue shifting in the experimental data than in the simulations. As shown in Figure 5.5, when the splitting between the two peaks in our RISD model is 1/2 or more of the width of each feature, $\bar{\nu}_{max}$ shifts to the red in the early portion of the relaxation process. The interplay between the blue shift seen in simulations and the red shift predicted by the RISD model is consistent with the slower early blue shift of $\bar{\nu}_{max}$ in the experimental spectra as compared to the simulated spectra.

At longer delay times, the simulated $\bar{\nu}_{max}$ becomes constant (for 1 Lorentzian) or exhibits a slow red shift (for 2 Lorentzians), whereas the experimental $\bar{\nu}_{max}$ begins to shift strongly to the blue. This observation is also in qualitative agreement with the results presented in Figure 5.5, in which a blue shift is observed as relaxation approaches completion regardless of the magnitude of the splitting between the two features.

At early delay times, the simulated and experimental FWHMs are in excellent agreement. In this region of time delays, the spectra narrow with increasing delay due to the increased temporal overlap of the probe pulse with the FID of the vibrational coherence. At longer times, this effect continues to dominate the FWHM for the simulated spectra. Experimentally, the FWHM increases at delays greater than 3.0 ps. This observation is consistent with the substantial broadening shown in Figure 5.5 as orientational relaxation nears completion. Because RISD also induces pure dephasing that is not included in our model, the time-dependent increase in line width should be even greater than that shown in Figure 5.5. Thus, the deviation of these results from the predictions of the simulations with a static underlying line shape are in good accord with our qualitative predictions of the effects of RISD.

5.4 Discussion and Conclusions

There is a growing recognition that dynamic processes can influence line shapes in VSFG. The potential influence of reorientation on VSFG spectra has been considered previously by a number of authors,[2-6] but only in the context of the reorientation of the Raman tensor (or, equivalently, the hyperpolarizability tensor) between the excitation and probing transitions in VSFG. This phenomenon only

influences the depolarized portion of the polarizability tensor, and so for totally symmetric vibrations it is typically not a major factor in determining the VSFG line shape, especially for modes that have largely isotropic Raman tensors (such as symmetric methyl stretches).[8]

Here I have considered the influence of reorientation on VSFG spectra under circumstances in which the frequency of a vibration can depend on the molecular orientation. In this case, reorientation influences the portions of the VSFG response corresponding to both the isotropic and anisotropic portions of the Raman tensor. Here I have only considered the influence of reorientation on the isotropic portion of the Raman tensor, but an analogous phenomenon holds for the anisotropic portion of the tensor.

VSFG spectra are typically acquired either entirely in the frequency domain, in which case all excitation/probe delays are sampled, or in a hybrid time/frequency (broadband) scheme in which a fixed subset of excitation/probe delays is sampled. In either case, it is difficult to know how great a contribution RISD makes to the spectra. Thus, for the system studied here we employed time-resolved, broadband VSFG. Even in the presence of a static underlying line shape, the VSFG spectrum changes substantially with time delay. By performing careful simulations of the time dependence of the observed line shape based on different static underlying line shapes, we were able to demonstrate that the time dependence of the VSFG spectrum of the symmetric methyl stretch of acetonitrile at the LS interface cannot be described fully using a purely static underlying line shape. Furthermore, the deviations from static models are reproduced qualitatively by a simple model of RISD.

RISD is likely to play a role in the VSFG line shape when the molecules involved can reorient on a time scale that is comparable to that of other mechanisms for vibrational dephasing and are in an environment in which the transition frequency depends strongly on orientation. Under such circumstances, great care should be taken in the use of VSFG spectra to assess average orientational distributions. RISD affects the isotopic and depolarized portions of the Raman tensor in different manners, and as a result the influence of this phenomenon on VSFG spectra will be different under different polarization conditions.

The work presented here is only a first step towards understanding the influence that RISD can have on VSFG spectra. It is important to understand how RISD influences the anisotropic portion of the Raman tensor for totally symmetric modes, as well as the role it plays in the VSFG spectroscopy of vibrational modes with other symmetries. More detailed, system-specific models of RISD also must be developed before any sort of quantitative evaluation of its effect on VSFG spectra can be performed. It will be necessary to determine the form of the orientational correlation function for a given system before such an evaluation can be made. In addition to further experiments, molecular dynamics simulations may be of great value in determining the role that RISD plays on VSFG spectroscopy.

5.5 References

1. Rivera, C. A.; Fourkas, J. T. Reexamining the Interpretation of Vibrational Sum-Frequency Generation Spectra. *Int. Rev. Phys. Chem.* **2011**, *30*, 409-443.

2. Wei, X.; Shen, Y. R. Motional Effect in Surface Sum-Frequency Vibrational Spectroscopy. *Phys. Rev. Lett.* **2001**, *86*, 4799-4802.

3. Fourkas, J. T.; Walker, R. A.; Can, S. Z.; Gershgoren, E. Effects of Reorientation in Vibrational Sum-Frequency Spectroscopy. *J. Phys. Chem. C* **2007**, *111*, 8902-8915.

4. Gan, W.; Wu, D.; Zhang, Z.; Feng, R. R.; Wang, H. F. Polarization and Experimental Configuration Analyses of Sum Frequency Generation Vibrational Spectra, Structure, and Orientational Motion of the Air/Water Interface. *J. Chem. Phys.* **2006**, *124*, 114705.

5. Sung, J. H.; Kim, D. Fast Motion of the Surface Alcohol Molecules Deduced from Sum-Frequency Vibrational Spectroscopy. *J. Phys. Chem. C* **2007**, *111*, 1783-1787.

6. Malyk, S.; Shalhout, F. Y.; O'Leary, L. E.; Lewis, N. S.; Benderskii, A. V. Vibrational Sum Frequency Spectroscopic Investigation of the Azimuthal Anisotropy and Rotational Dynamics of Methyl-Terminated Silicon(111) Surfaces. *J. Phys. Chem. C* **2013**, *117*, 935-944.

7. Liu, S.; Fourkas, J. T. Orientational Time Correlation Functions for Vibrational Sum-Frequency Generation. 1. Acetonitrile. *J. Phys. Chem. A* **2012**, *117*, 5853-5864.

8. Gengeliczki, Z.; Rosenfeld, D. E.; Fayer, M. D. Theory of Interfacial Orientational Relaxation Spectroscopic Observables. *J. Chem. Phys.* **2010**, *132*, 244703.

9. Hsieh, C. S.; Campen, R. K.; Verde, A. C. V.; Bolhuis, P.; Nienhuys, H. K.; Bonn, M. Ultrafast Reorientation of Dangling OH Groups at the Air-Water Interface using Femtosecond Vibrational Spectroscopy. *Phys. Rev. Lett.* **2011**, *107*, 116102.

10. Rosenfeld, D. E.; Gengeliczki, Z.; Smith, B. J.; Stack, T. D. P.; Fayer, M. D. Structural Dynamics of a Catalytic Monolayer Probed by Ultrafast 2D IR Vibrational Echoes. *Science* **2011**, *334*, 634-639.

11. Verde, A. V.; Bolhuis, P. G.; Campen, R. K. Statics and Dynamics of Free and Hydrogen-Bonded OH Groups at the Air/Water Interface. *J. Phys. Chem. B* **2012**, *116*, 9467-9481.

12. Xiong, W.; Laaser, J. E.; Mehlenbacher, R. D.; Zanni, M. T. Adding a Dimension to the Infrared Spectra of Interfaces using Heterodyne Detected 2D Sum-Frequency Generation (HD 2D SFG) Spectroscopy. *Proc. Nat. Acad. Sci. USA* **2011**, *108*, 20902-20907.

13. Yamamoto, S.; Ghosh, A.; Nienhuys, H. K.; Bonn, M. Ultrafast Inter- and Intramolecular Vibrational Energy Transfer between Molecules at Interfaces Studied by Time- and Polarization-Resolved SFG Spectroscopy. *Phys. Chem. Chem. Phys.* **2010**, *12*, 12909-12918.

14. Nienhuys, H. K.; Bonn, M. Measuring Molecular Reorientation at Liquid Surfaces with Time-Resolved Sum-Frequency Spectroscopy: A Theoretical Framework. *J. Phys. Chem. B* **2009**, *113*, 7564-7573.

15. Koningstein, J. A. *Introduction to the Theory of the Raman Effect*; Reidel: Dordrecht, 1972.

16. Durig, J. R.; Hawley, C. W. Vibrational Assignments and Torsional Barrier Heights of Some Methylsilylchlorides. *J. Chem. Phys.* **1973**, *59*, 1-14.

17. Durig, J. R.; Hawley, C. W. Vibrational Assignments and Torsional Barrier Heights of the Dimethylhalosilanes. *J. Chem. Phys.* **1973**, *58*, 237-248.

18. Durig, J. R.; Xiao, J. Conformational Stabilities of Dimethylmethoxyphosphine and Dimethyl(methylthio)phosphine from Temperature Dependent Infrared Spectra of Rare Gas Solutions. *J. Mol. Struct.* **2000**, *526*, 373-389.

19. Bell, S.; Zhu, X.; Guirgis, G. A.; Durig, J. R. Infrared and Raman Spectra, Conformational Stability, *Ab Initio* Calculations of Structure and Vibrational Assignment of 5-fluoropent-2-yne. *Phys. Chem. Chem. Phys.* **2001**, *3*, 776-785.

20. Steel, W. H.; Walker, R. A. Measuring Dipolar Width Across Liquid-Liquid Interfaces With "Molecular Rulers". *Nature* **2003**, *424*, 296-299.

21. Fenn, E. E.; Wong, D. B.; Giammanco, C. H.; Fayer, M. D. Dynamics of Water at the Interface in Reverse Micelles: Measurements of Spectral Diffusion with Two-Dimensional Infrared Vibrational Echoes. *J. Phys. Chem. B* **2011**, *115*, 11658-11670.

22. Stein, A. D.; Fayer, M. D. Spectral Diffusion in Liquids. *J. Chem. Phys.* **1992**, *97*, 2948-2962.

23. Gulmen, T. S.; Thompson, W. H. Grand Canonical Monte Carlo Simulations of Acetonitrile Filling of Silica Pores of Varying Hydrophilicity/Hydrophobicity. *Langmuir* **2009**, *25*, 1103-1111.

24. Morales, C. M.; Thompson, W. H. Simulations of Infrared Spectra of Nanoconfined Liquids: Acetonitrile Confined in Nanoscale, Hydrophilic Silica Pores. *J. Phys. Chem. A* **2009**, *113*, 1922-1933.

25. Hu, Z.; Weeks, J. D. Acetonitrile on Silica Surfaces and at Its Liquid-Vapor Interface: Structural Correlations and Collective Dynamics. *J. Phys. Chem. C* **2010**, *114*, 10202-10211.

26. Ding, F.; Hu, Z. H.; Zhong, Q.; Manfred, K.; Gattass, R. R.; Brindza, M. R.; Fourkas, J. T.; Walker, R. A.; Weeks, J. D. Interfacial Organization of Acetonitrile: Simulation and Experiment. *J. Phys. Chem. C* **2010**, *114*, 17651-17659.

27. Cheng, L. W.; Morrone, J. A.; Berne, B. J. Structure and Dynamics of Acetonitrile Confined in a Silica Nanopore. *J. Phys. Chem. C* **2012**, *116*, 9582-9593.

28. Liebsch, A. Theory of Sum Frequency Generation from Metal Surfaces. *Appl. Phys. B* **1999**, *68*, 301-304.

29. Rivera, C. A.; Bender, J. S.; Manfred, K.; Fourkas, J. T. Persistence of Acetonitrile Bilayers at the Interface of Acetonitrile/Water Mixtures with Silica. *J. Phys. Chem. A* **2013**, DOI: 10.1021/jp4045572.

30. Stiopkin, I. V.; Jayathilake, H. D.; Weeraman, C.; Benderskii, A. V. Temporal Effects on Spectroscopic Line Shapes, Resolution, and Sensitivity of the Broad-Band Sum Frequency Generation. *J. Chem. Phys.* **2010**, *132*, 234503.

31. Bonn, M.; Ueba, H.; Wolf, M. Theory of Sum-Frequency Generation Spectroscopy of Adsorbed Molecules Using the Density Matrix Method - Broadband Vibrational Sum-Frequency Generation and Applications. *J. Phys.-Cond. Matt.* **2005**, *17*, S201-S220.

32. Levenberg, K. A Method for the Solution of Certain Non-Linear Problems in Least Squares. *Quart. Appl. Math.* **1944**, *2*, 164-168.

33. Marquardt, D. An Algorithm for Least-Squares Estimation of Nonlinear Parameters. *J. Soc. Ind. Appl. Math.* **1963**, *11*, 431-441.

Chapter 6: The Effect of Temperature on the Organization of Acetonitrile at the Silica/Liquid Interface

Adapted from: Souna, A. J.; Clark, T. L.; Fourkas, J. T. *J. Phys. Chem. C*, 2017, 121, 26432-26437.
Research designed by: Amanda J. Souna
Research conducted by: Amanda J. Souna and Tylar L. Clark
Authored by: Amanda J. Souna and John T. Fourkas

6.1 Introduction

Despite the relatively simple structure of an acetonitrile molecule, the organization of liquid acetonitrile exhibits fascinating behavior. Given the substantial dipole moment[1] of this molecule (3.92 D), acetonitrile has some propensity for dipole pairing in the bulk.[2-3] However, at a silica surface, acetonitrile takes on a remarkably different organization that in some ways resembles that of a supported lipid bilayer.[4] A planar lipid bilayer is centrosymmetric. Given that acetonitrile takes on a similar organization at the SL interface, one could image that the VSFG signal for this system would be small. However, there is actually a substantial VSFG signal for the symmetric methyl stretch of acetonitrile at the silica interface.[5-6] Two factors contribute to the incomplete cancellation of the signal from the two sublayers that make up the interfacial bilayer. First, the molecules that accept hydrogen bonds from the silanol groups on the surface (which we will designate the first sublayer) is highly ordered due to the constraints imposed by these bonds.[5, 7-9] The second sublayer, on the other hand, is considerably more disordered because it is not constrained by hydrogen bonds.[5, 7-9] There is also a slightly smaller population in the second sublayer.[5, 8] Second, because the molecules in the first sublayer accept hydrogen bonds, the symmetric methyl stretch shifts in frequency.[5]

Here VSFG is used to explore the effect of temperature on acetonitrile at the silica/liquid interface. The effect of temperature on the organization of interfacial liquids is a relatively unexplored realm in VSFG studies.[10-13] The organization of simple liquids typically does not exhibit a strong temperature dependence, and the same situation is likely to hold for many simple liquids at interfaces. Because the organization of acetonitrile at the SL is so different from that in the bulk, and because this structure is dependent in part on weak, non-polar interactions, we reasoned that the VSFG spectrum of acetonitrile might have a substantial temperature dependence. Here I explore how the intensities and positions of the methyl stretching modes depend on temperature. This information gives us insights into the microscopic organization and dynamics of the surface bilayer.

6.2 Experimental

The counterpropagating VSFG spectrometer employed for these experiments is described in detail in Chapter Three in Section 3.1-3.3. For these experiments, the probe pulse has a pulse energy of 15 μJ and bandwidth of 5.5 cm^{-1}. The sample cuvettes (Firefly type 21 cell, 2 mm pathlength, IR quartz) were prepared by rinsing sequentially with acetone, methanol, and deionized water, followed by drying in an oven and then cleaning in an oxygen plasma for 3 min. The acetonitrile used was 99+% spectroscopic grade (ACROS). The sample was placed on a thermoelectric module (TE Technology). A thin layer of thermal grease was used to ensure good thermal contact. Spectra were obtained at 25° C and 60° C. The sample was allowed to equilibrate at each new temperature for at least 20 min before spectra were measured, and the height was adjusted to maximize the signal. Measurements made by beginning at 25 °C and then

heating to 60 °C gave identical results to measurements made by beginning at 60 °C and then cooling to 25 °C. Spectra were obtained with a delay of 667 fs between the IR and probe pulses for *SSP* and *PPP* and 167 fs for the *SPS* polarization conditions (the polarizations are listed in the order signal, probe, IR). Four scans were performed for each polarization condition, with an acquisition time of 1 min for *SSP* and *PPP* spectra and 2 min for *SPS* spectra.

To measure the temperature dependence of the index of refraction, a temperature-controlled cell with a 5 mm path length was placed in either the IR beam or the probe beam. The SFG response from a ZnSe crystal was detected. A delay stage was used to measure the change in path length between an empty cell and a cell filled with acetonitrile. Published sodium D line refractive indices for acetonitrile from 15 °C to 45 °C were extrapolated to 60 °C to determine the refractive index at the signal frequency.[14]

6.3 Results and Discussion

The methyl stretching region of the *SSP* VSFG spectrum of acetonitrile at the SL interface is shown in Figure 6.1 at 25 °C and 60 °C. This polarization combination is sensitive to molecules with a projection of the IR transition dipole along the surface normal, and emphasizes the isotropic portion of the Raman tensor.[15] At both temperatures, the only mode that was observed in this spectral region was the symmetric methyl stretch, which appears at a frequency in the neighborhood of 2945 cm^{-1}. The absence of the asymmetric methyl stretch (not shown) indicates that the acetonitrile symmetry axis has a substantial projection along the surface normal. The *SSP* spectrum at 60 °C is blue-shifted by about 1.0 cm^{-1} relative to the *SSP* spectrum at

25 °C, and is notably weaker, with an apparent decrease in maximum intensity of 11%. After adjusting for the temperature variation of the Fresnel factors (*vide infra*) this decrease becomes 18%.

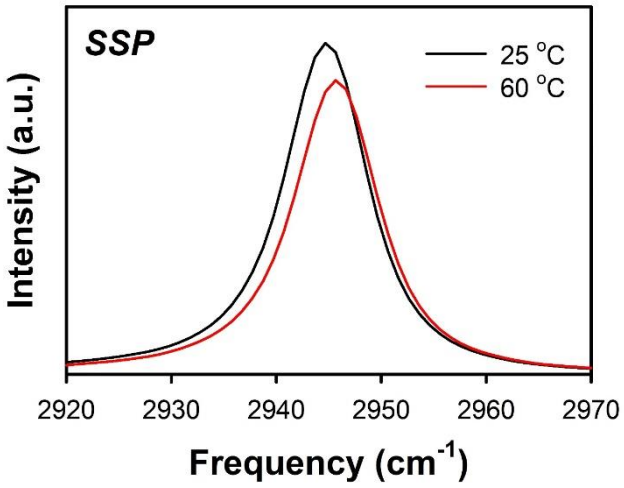

Figure 6.1 VSFG spectra of acetonitrile at the silica/liquid interface at 25 °C and 60 °C under *SSP* polarization conditions.

The VSFG spectra at 25 °C and 60 °C under *SPS* polarization conditions are shown in Figure 6.2. The primary contribution to the spectrum at both temperatures is from the asymmetric methyl stretch. This polarization combination is sensitive to IR transition dipoles that are parallel to the interface, and so observing this mode under *SPS* conditions is consistent with observing the symmetric methyl stretch under *SSP* conditions. Any contribution from the symmetric methyl stretch (not shown) is further minimized by the fact that this mode is strongly polarized,[16] whereas the *SPS* signal is sensitive only to the anisotropic portion of the Raman tensor.[15, 17] The *SPS* signal is considerably weaker than the *SSP* signal due to the rapid rotation of the acetonitrile methyl group.[18-19] These rapid dynamics are also responsible for the width of the *SPS* spectrum. As was the case for the *SSP* spectrum, the *SPS* spectrum blue-shifts and

becomes weaker at elevated temperature with an apparent decrease in maximum intensity of 26%. After adjusting for the temperature variation of the Fresnel factors this decrease becomes 31%.

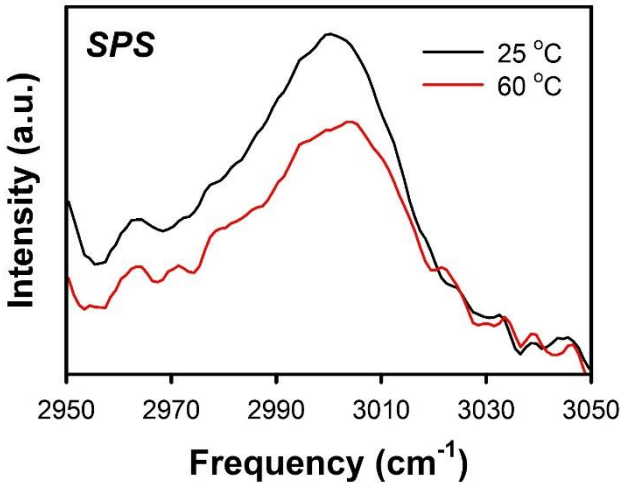

Figure 6.2 VSFG spectra of acetonitrile at the silica/liquid interface at 25 °C and 60 °C under *SPS* polarization conditions.

In Figure 6.3 are shown the *PPP* spectra of this system at 25 °C and 60 °C. The *PPP* spectrum is sensitive to IR transition dipoles that point in all directions, and tends to emphasize the anisotropic portion of the Raman tensor.[15] Accordingly, both the symmetric and asymmetric methyl stretches are observed in the *PPP* spectrum. Once again, the spectrum weakens and blue-shifts with increasing temperature. The apparent decrease in maximum intensity for the PPP configuration is 9%. We did not adjust for the temperature variation of the Fresnel factors in this case, as there is too much uncertainty in the relative contributions of the different tensor components of the susceptibility.

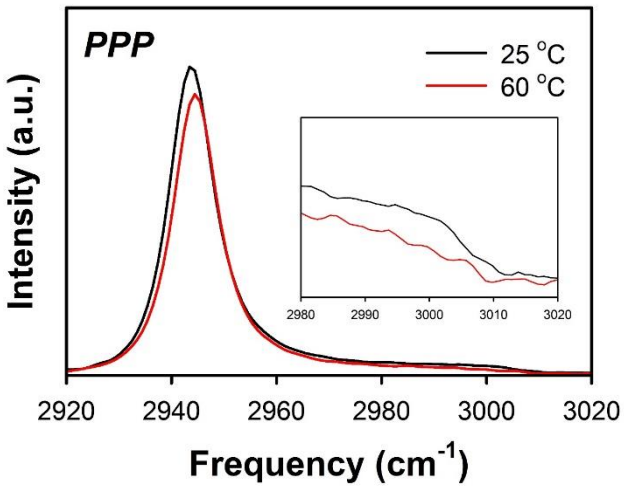

Figure 6.3 VSFG spectra of acetonitrile at the silica/liquid interface at 25 °C and 60 °C under *PPP* polarization conditions. The inset zooms in on the contribution from the asymmetric methyl stretch.

First consider the difference in the intensity of the spectra at high temperature. Given that the first sublayer of acetonitrile molecules is orientationally constrained by the silica surface, one might expect that the disorder in the second sublayer would be more sensitive to temperature. Increased disorder in the second sublayer would reduce the degree of cancellation in the VSFG signal between the sublayers, thereby increasing the signal. Any reduction in the density of the second sublayer with increasing temperature would also be expected to reduce signal cancellation. However, it is clear from the spectra presented here that these intuitive expectations are not met. What might cause this phenomenon?

One possibility is that the decrease in intensity with increasing temperature is due simply to a decrease in the vibrational lifetime. However, temperature-dependent IR absorption studies indicate that the symmetric methyl stretch lifetime is constant (at ~1.23 ps) over the temperature range studied here.[20] In agreement with this picture, the linewidths of the VSFG spectra presented here do not have a significant temperature

dependence. The orientational correlation time in the bulk liquid also decreases with increasing temperature.[21] However, the first sublayer does not undergo substantial reorientation on the time scale of vibrational relaxation.[18] More rapid orientational dynamics of the second sublayer might be expected, in the simplest picture, to lead to a more rapid loss of cancellation of the signals between the two sublayers. However, the strongly polarized nature of the symmetric methyl stretch means that the Raman transition is largely isotropic, and so reorientation is not, on its own, an effective dephasing mechanism.[22]

The VSFG intensity is proportional to the square of the effective nonlinear susceptibility. Depending on the polarization configuration employed, the effective nonlinear susceptibility is proportional to a defined tensor element or a linear combination of tensor elements. Each configuration is dependent on nonlinear Fresnel factors, which are a function of the refractive indices of the bulk media and interface as well as of the experimental geometry.[15] The effective second-order susceptibilities are given by:

$$\begin{aligned}\chi^{(2)}_{eff,SSP} &= L_{xx}(\omega_{sig})L_{xx}(\omega_{probe})L_{zz}(\omega_{IR})sin\,\theta_{IR}\chi^{(2)}_{xxz} \\ &= c_{xxz}\chi^{(2)}_{xxz}\,, \end{aligned} \tag{6.1a}$$

$$\begin{aligned}\chi^{(2)}_{eff,SPS} &= L_{xx}(\omega_{sig})L_{zz}(\omega_{probe})L_{xx}(\omega_{IR})sin\,\theta_{probe}\chi^{(2)}_{xzx} \\ &= c_{xzx}\chi^{(2)}_{xzx}\,, \end{aligned} \tag{6.1b}$$

and

$$\begin{aligned}\chi^{(2)}_{eff,PPP} &= L_{yy}(\omega_{sig})L_{yy}(\omega_{probe})L_{zz}(\omega_{IR})cos\,\theta_{sig}cos\,\theta_{probe}sin\,\theta_{IR}\,\chi^{(2)}_{yyz} \\ &+ L_{yy}(\omega_{sig})L_{zz}(\omega_{probe})L_{yy}(\omega_{IR})cos\,\theta_{sig}sin\,\theta_{probe}cos\,\theta_{IR}\chi^{(2)}_{yzy} \\ &+ L_{zz}(\omega_{sig})L_{yy}(\omega_{probe})L_{yy}(\omega_{IR})sin\,\theta_{sig}cos\,\theta_{probe}cos\,\theta_{IR}\chi^{(2)}_{zyy} \\ &+ L_{zz}(\omega_{sig})L_{zz}(\omega_{probe})L_{zz}(\omega_{IR})sin\,\theta_{sig}sin\,\theta_{probe}sin\,\theta_{IR}\chi^{(2)}_{zzz} \\ &= c_{yyz}\chi^{(2)}_{yyz} + c_{yzy}\chi^{(2)}_{yzy} + c_{zyy}\chi^{(2)}_{zyy} + c_{zzz}\chi^{(2)}_{zzz} \end{aligned} \tag{6.1c}$$

The nonlinear Fresnel factors are given by[23]

$$L_{xx}(\omega_i) = \frac{2n_1(\omega_i)\cos\beta_i}{n_1(\omega_i)\cos\beta_i + n_2(\omega_i)\cos\gamma_i}\,, \tag{6.2a}$$

$$L_{yy}(\omega_i) = \frac{2n_1(\omega_i)\cos\gamma_i}{n_1(\omega_i)\cos\gamma_i + n_2(\omega_i)\cos\beta_i}, \quad (6.2b)$$

and

$$L_{zz}(\omega_i) = \frac{2n_2(\omega_i)\cos\beta_i}{n_1(\omega_i)\cos\gamma_i + n_2(\omega_i)\cos\beta_i}\left(\frac{n_1(\omega_i)}{n'(\omega_i)}\right)^2, \quad (6.2c)$$

in which n_1, n_2, and n' are the refractive indices of medium 1 (silica), medium 2 (acetonitrile), and the interface respectively, and γ_i is the angle of the beam propagating into medium 2, as defined by Snell's law:

$$n_1(\omega_i)\sin\beta_i = n_2(\omega_i)\sin\gamma_i . \quad (6.3)$$

The β_i are the angles of incidence at the interface and are calculated using the experimental angles at the air/silica surface -58°, 61°, and -32.8° (IR, probe, signal), and Snell's law, resulting in respective β_i of -37°, 37°, and -21.9°.[24] The *yz* plane is the plane of incidence. The refractive indices for the three beams at both temperatures are given in Table 6.1, and the prefactors are given in Table 6.2. The interfacial refractive index was estimated to be the same as that of acetonitrile, but the essential conclusions below are not changed by using a model with an interfacial refractive index[23] halfway between that of the two media, or by assuming that the refractive index of the acetonitrile is 1 because we are on resonance. The temperature dependence of the refractive index of silica is so small that it can be ignored over this temperature range.[25]

Table 6.1: Refractive Indices of Acetonitrile and Silica.[26]

	ACN 25 °C	ACN 60 °C	Silica
n_{IR}	1.355	1.3352	1.409
n_{probe}	1.337	1.325	1.4533
n_{signal}	1.3412	1.326	1.4566

Table 6.2: Prefactors for the Tensor Elements of $\chi^{(2)}$ at Different Temperatures

Prefactor	25 °C	60 °C
c_{xxz}	-.72	-.75
c_{xzx}	.76	.78
c_{yyz}	-.54	-.56
c_{yzy}	.55	.56
c_{zyy}	-.29	-.30
c_{zzz}	.19	.20

For each polarization condition, the nonlinear Fresnel factors are larger at 60 °C than at 25 °C. All other things being equal, this result implies that the signal should be larger at high temperature than at room temperature, rather than smaller. Thus, the discrepancy between the signal intensities at 25 °C and 60 °C is even larger than indicated by inspection of the spectra.

These results suggest that it is important to consider how the temperature dependence of the organization in the two sublayers could influence the signal. First consider the fact that the change in intensity at high temperature is considerably greater for the *SPS* spectra than for the *SSP* or *PPP* spectra. If we ignore the possibility of molecules reorienting between the IR and Raman transitions for the moment, the expressions for the tensor elements of the second-order susceptibility relevant to the *SSP* and *SPS* spectra are, respectively[15]

$$\chi^{(2)}_{xxz} \propto \mu'_z \left(\alpha'_I - \frac{1}{6}\alpha'_A\right)\langle\cos\theta\rangle + \frac{1}{2}\mu'_z\alpha'_A\langle\cos^3\theta\rangle \qquad (6.4a)$$

and

$$\chi^{(2)}_{xzx} \propto \frac{1}{2}\left(\mu'_x\alpha'_{xz} + \mu'_y\alpha'_{yz}\right)\langle\cos^3\theta\rangle\,. \qquad (6.4b)$$

Here, μ'_z is the IR transition dipole for the symmetric methyl stretch and μ'_x and μ'_y are the transition dipoles for the doubly-degenerate asymmetric methyl stretch, α'_I and

α'_A are the isotropic and anisotropic changes, respectively, in the polarizability tensor for the symmetric methyl stretch, and α'_{xz} and α'_{yz} are the changes in the polarizability tensor for the asymmetric methyl stretch, which is a completely depolarized mode. For the acetonitrile symmetric methyl stretch, α'_I is about three times as large as α'_{yz}.[18] Thus, we expect the prefactor for $\langle \cos\theta \rangle$ in eq 6.4a to be substantially larger than the prefactor for $\langle \cos^3\theta \rangle$. The $\langle \cos\theta \rangle$ term therefore dominates the *SSP* spectrum whereas the *SPS* spectrum only has a $\langle \cos^3\theta \rangle$ term. Except at angles near 90°, $\cos^3\theta$ is steeper than $\cos\theta$, which explains why the intensity change in the *SPS* spectrum with increasing temperature is considerably greater than the change in the *SSP* spectrum. A similar argument can be made for the *PPP* spectrum.

The decrease in intensity of the VSFG spectrum under all polarization conditions indicates that the idea that the second sublayer should gain more disorder than the first sublayer with increasing temperature must be incorrect. Hu and Weeks have simulated liquid acetonitrile at the SL interface, and calculated the orientational distributions of both sublayers.[8] The second sublayer exhibits a considerably greater orientational distribution than does the first sublayer,[8] as would be expected.

The orientational dynamics in the second sublayer has also been found in simulations to be considerably faster than those in the first sublayer.[18] The small size of the acetonitrile molecule sets these lipid-bilayer-like structures apart from true supported lipid bilayers, in that the second sublayer is considerably more dynamic in the case of acetonitrile. Although static snapshots of the organization bear a strong resemblance to a lipid bilayer,[5, 8] the second sublayer should be viewed as being in

constant flux, but with its orientational dynamics biased by interactions with the first sublayer. The degree of this bias may not be so strongly dependent on temperature.

By virtue of most of its molecules being tethered to the silica surface, the first sublayer has dynamics that differ substantially from those of the second sublayer. Although there is some amount of relatively fast orientational dynamics with molecules wobbling about their hydrogen bonds, these dynamics have a relatively small amplitude.[18] The remaining orientational dynamics occur on a much longer time scale. Given the strength of the hydrogen bonds to the molecules in the first sublayer,[27] and their consequent long lifetimes,[28] it is reasonable to think of the organization as being static compared to that of the second sublayer.

These ideas lead to a picture in which the second sublayer is highly dynamic, but has an average organization that is not strongly dependent on temperature because it is already so disordered at room temperature. The first sublayer is relatively static in comparison, and so its average organization can have a stronger temperature dependence. The combination of these two effects would lead to the VSFG intensity decreasing with temperature. Because the more ordered first sublayer contributes more to the overall signal, an increase in disorder in this sublayer will decrease the intensity of the spectra.

Next consider the blue shift of the spectra with increasing temperature. In bulk acetonitrile, there is a blue shift of approximately 0.4 cm^{-1} in the symmetric methyl stretch over this temperature range.[20] This value cannot be related directly to what is seen in VSFG spectra, as the second sublayer is not in a bulk environment, but it does suggest that the contribution from this sublayer should blue-shift with increasing

temperature. The situation is less clear for the first sublayer, as its density and dielectric environment are not likely to be strongly affected by temperature. Temperature-dependent studies of hydrogen-bonded acetonitrile in MCM-41 revealed a 2 cm^{-1} redshift for the CN stretch as the temperature increased from 10 °C to 59 °C,[29] presumably due to some weakening of the hydrogen bonds due to increased orientational dynamics. As the blue shift of the CN stretch upon hydrogen bonding is reflected in a blue shift in the methyl symmetric stretch,[5] this phenomenon cannot be responsible for the observed blue shift with increasing temperature. In addition, the magnitude of any temperature-induced red shift in the methyl symmetric stretch is likely to be too small to detect over the temperature range that we have studied.

Isotropic Raman spectra of the symmetric methyl stretch of acetonitrile in solution show a substantial blue shift in going from a nonpolar solvent to a polar one.[30] It was shown in Chapter Five, by measuring time-resolved VSFG spectra, that reorientation in the second sublayer of acetonitrile at the SL interface can lead to a blue shift that increases with the time between exciting the vibrational coherence and probing it. The idea behind this phenomenon is that molecules in the second sublayer are free to undergo orientational diffusion following excitation. Methyl groups that initially point towards the silica surface can reorient so as to point into the bulk, experiencing a considerably more polar environment. The opposite can happen for methyl groups that initially point away from the surface. Because substantially more molecules in the second sublayer point toward the silica surface than away from it,[8] the net effect of RISD is to induce a time-dependent blue shift in the spectrum.

Although RISD could be time resolved at room temperature, acetonitrile reorients considerably more rapidly at 60 °C (with a single-molecule orientational correlation time of 0.71 ps in the bulk, as compared to 1.01 ps at 25 °C).[21] Thus, RISD occurs more rapidly at higher temperature, causing a faster blue shift of a spectrum, and therefore a greater blue shift at a fixed delay time. The reorientation time at 60 °C is so short that it is not practical to try to time resolve it, as other spectroscopic effects distort the shape of the signal at shorter delay times.[31]

As mentioned above, because the *SSP* spectrum of the symmetric methyl stretch is dominated by the isotropic portion of the polarizability, the evolving orientational distribution following excitation does not, in and of itself, lead to dephasing. However, the presence of RISD changes the situation by causing molecules to experience a time-dependent transition frequency. This phenomenon can act as a rapid dephasing mechanism in the second sublayer, which would lead to a loss of cancellation of signal with the first sublayer. This effect is counterbalanced to some extent by the fact that blue-shifting of the signal from the second sublayer should cause it to interfere more effectively with the contribution from the first sublayer. This effect may play a role in the decrease of the signal intensity with increasing temperature.

6.4 Conclusions

I have presented a comparative VSFG study of acetonitrile at the SL interface at 25 °C and 60 °C. Contrary to expectations based on a static picture of the lipid-bilayer-like organization of the liquid at this interface, the signal intensity decreases with temperature under all polarization conditions. This result suggests that dynamics plays an important role in determining the temperature dependence of the VSFG signal.

As the temperature is increased, the orientational dynamics of the second sublayer occur on a faster time scale than does vibrational relaxation, but apparently without causing a substantial change in the average organization. Thus, on the time scale probed by VSFG spectroscopy, it may not be appropriate to think of the second sublayer in terms of a static structure. On the other hand, the relatively static first sublayer contributes to the decrease in intensity as it becomes more disordered with temperature.

The more rapid the reorientation, the stronger the effects of reorientation-induced spectral diffusion should be as well. We believe that the influence of RISD on the second sublayer plays an important role in the blue shift of the spectra with temperature, and also in the decrease of intensity with temperature. It would be interesting to perform temperature-dependent simulations of this interface to explore these effects in greater detail.

6.5 References

1. Steiner, P. A.; Gordy, W., Precision measurement of dipole moments and other spectral constants of normal and deuterated methyl fluoride and methyl cyanide. *J. Mol. Spectrosc.* **1966,** *21* (1), 291-301.

2. Saitô, H.; Tanaka, Y.; Nagata, S.; Nukada, K., ^{13}C nuclear magnetic resonance studies on molecular association. I. Self-association of dipolar molecules. *Can. J. Chem.* **1973,** *51* (13), 2118-2123.

3. Gorbunova, T. V.; Batalin, G. I., The problem of the structure of liquid aliphatic nitriles. *J. Struct. Chem.* **1977,** *17* (3), 392-395.

4. Berne, B. J.; Fourkas, J. T.; Walker, R. A.; Weeks, J. D., Nitriles at silica interfaces resemble supported lipid bilayers. *Acc. Chem. Res.* **2016,** *49* (9), 1605-1613.

5. Ding, F.; Hu, Z.; Zhong, Q.; Manfred, K.; Gattass, R. R.; Brindza, M. R.; Fourkas, J. T.; Walker, R. a.; Weeks, J. D., Interfacial organization of acetonitrile: Simulation and experiment. *J. Phys. Chem. C* **2010,** *114*, 17651-17659.

6. Henry, M. C.; Piagessi, E. A.; Zesotarski, J. C.; Messmer, M. C., Sum-frequency observation of solvent structure at model chromatographic interfaces: Acetonitrile−water and methanol−water systems. *Langmuir* **2005,** *21* (14), 6521-6526.

7. Gulmen, T. S.; Thompson, W. H., Grand canonical monte carlo simulations of acetonitrile filling of silica pores of varying hydrophilicity/hydrophobicity. *Langmuir* **2009,** *25* (2), 1103-1111.

8. Hu, Z.; Weeks, J. D., Acetonitrile on silica surfaces and at its liquid−vapor interface: Structural correlations and collective dynamics. *J. Phys. Chem. C* **2010,** *114* (22), 10202-10211.

9. Cheng, L.; Morrone, J. A.; Berne, B. J., Structure and dynamics of acetonitrile confined in a silica nanopore. *J. Phys. Chem. C* **2012,** *116* (17), 9582-9593.

10. Fordyce, A. J.; Bullock, W. J.; Timson, A. J.; Haslam, S.; Spencer-Smith, R. D.; Alexander, A.; Frey, J. G., The temperature dependence of surface second-harmonic generation from the air-water interface. *Mol. Phys.* **2001,** *99* (8), 677-687.

11. Goh, M. C.; Hicks, J. M.; Kemnitz, K.; Pinto, G. R.; Bhattacharyya, K.; Heinz, T. F.; Eisenthal, K. B., Absolute orientation of water molecules at the neat water surface. *J. Phys. Chem.* **1988,** *92* (18), 5074-5075.

12. Goh, M. C.; Eisenthal, K. B., The energetics of orientation at the liquid vapor interface of water. *Chem. Phys. Lett.* **1989,** *157* (1-2), 101-104.

13. Nagata, Y.; Hasegawa, T.; Backus, E. H.; Usui, K.; Yoshimune, S.; Ohto, T.; Bonn, M., The surface roughness, but not the water molecular orientation varies with temperature at the water-air interface. *Phys Chem Chem Phys* **2015,** *17* (36), 23559-64.

14. Shekaari, H.; Zafarani-Moattar, M. T.; Mirheydari, S. N., Density, viscosity, speed of sound, and refractive index of a ternary solution of aspirin, 1-butyl-3-methylimidazolium bromide, and acetonitrile at different temperatures: T = (288.15 to 318.15) K. *J. Chem. Eng. Data* **2015,** *60* (6), 1572-1583.

15. Rivera, C. A.; Fourkas, J. T., Reexamining the interpretation of vibrational sum-frequency generation spectra. *Int. Rev. Phys. Chem.* **2011,** *30* (4), 409-443.

16. Quinet, O.; Champagne, B.; Rodriguez, V., Experimental and theoretical investigation of the raman and hyper-raman spectra of acetonitrile and its derivatives. *J. Chem. Phys.* **2006,** *124* (24), 244312.

17. Fourkas, J. T.; Walker, R. A.; Can, S. Z.; Gershgoren, E., Effects of reorientation in vibrational sum-frequency spectroscopy. *J. Phys. Chem. C* **2007,** *111*, 8902-8915.

18. Liu, S. L.; Fourkas, J. T., orientational time correlation functions for vibrational sum-frequency generation. 1. Acetonitrile. *J Phys. Chem. A* **2013,** *117* (29), 5853-5864.

19. Rivera, C. A.; Bender, J. S.; Manfred, K.; Fourkas, J. T., Persistence of acetonitrile bilayers at the interface of acetonitrile/water mixtures with silica. *J. Phys. Chem A* **2013,** *117* (46), 12060-12066.

20. Sugitani, A.; Ikawa, S.-i.; Konaka, S., Effect of temperature on the infrared band shapes and reorientational and vibrational relaxation of liquid acetonitrile. *Chem. Phys.* **1990,** *142* (3), 423-430.

21. Loughnane, B. J.; Scodinu, A.; Farrer, R. A.; Fourkas, J. T.; Mohanty, U., Exponential intermolecular dynamics in optical Kerr effect spectroscopy of small-molecule liquids. *J. Chem. Phys.* **1999,** *111* (6), 2686.

22. Rivera, C. A.; Souna, A. J.; Bender, J. S.; Manfred, K.; Fourkas, J. T., Reorientation-induced spectral diffusion in vibrational sum-frequency-generation spectroscopy. *J. Phys. Chem. B* **2013,** *117* (49), 15875-15885.

23. Zhuang, X.; Miranda, P. B.; Kim, D.; Shen, Y. R., Mapping molecular orientation and conformation at interfaces by surface nonlinear optics. *Phys. Rev. B* **1999,** *59* (19), 12632-12640.

24. Wang, H. F.; Gan, W.; Lu, R.; Rao, Y.; Wu, B. H., Quantitative spectral and orientational analysis in surface sum frequency generation vibrational spectroscopy (SFG-VS). *Int. Rev. Phys. Chem.* **2005,** *24* (2), 191-256.

25. Toyoda, T.; Yabe, M., The temperature dependence of the refractive indices of fused silica and crystal quartz. *J. Phys. D* **1983,** *16* (5), L97.

26. Malitson, I. H., Interspecimen comparison of the refractive index of fused silica. *J. Opt. Soc. Am.* **1965,** *55* (10), 1205-1209.

27. Curthoys, G.; Davydov, V. Y.; Kiselev, A. V.; Kiselev, S. A.; Kuznetsov, B. V., Hydrogen bonding in adsorption on silica. *J. Colloid Interface Sci.* **1974,** *48* (1), 58-72.

28. Loughnane, B. J.; Farrer, R. A.; Scodinu, A.; Fourkas, J. T., Dynamics of a wetting liquid in nanopores: An optical Kerr effect study of the dynamics of acetonitrile confined in sol-gel glasses. *J. Chem. Phys.* **1999,** *111* (11), 5116-5123.

29. Tanaka, H.; Matsumoto, A.; Unger, K. K.; Kaneko, K., Molecular mobility of hydrogen-bonded acetonitrile on surface hydroxyls of MCM-41 with Kubo-Rothschild analysis. *Stud. Surf. Sci. Catal.* **2001,** *132*, 797-800.

30. Yarwood, J.; Arndt, R.; Döge, G., Studies of molecular motions and vibrational relaxation in acetonitrile. I. Raman spectral studies of the ν_1 ν_3 and $2\nu_3$ bands in the liquid and in dilute solutions. *Chem. Phys.* **1977,** *25* (3), 387-400.

31. Stiopkin, I. V.; Jayathilake, H. D.; Weeraman, C.; Benderskii, A. V., Temporal effects on spectroscopic line shapes, resolution, and sensitivity of the broad-band sum frequency generation. *J. Chem. Phys.* **2010,** *132*, 234503.

Chapter 7: Intermolecular Vibrational Coupling in Liquid Acetonitrile at the Silica Interface

Adapted from: Souna, A. J.; Rivera, C. A.; Manfred, K. M.; Fourkas, J. T. *J. Chem. Phys.* (submitted for publication)
Research designed by: Amanda J. Souna
Research conducted by: Amanda J. Souna, Christopher A. Rivera, and Katherine Manfred
Authored by: Amanda J. Souna and John T. Fourkas

7.1 Introduction

VSFG spectra are generally interpreted within a static picture, and in terms of the spectroscopic properties of individual molecules. As discussed in earlier chapters, there is a growing recognition that dynamics can play an important role in VSFG spectra.[1] In condensed-phase systems, dynamic processes such as reorientation and energy transfer can occur on a time scale of picoseconds or less.[1] This time scale is comparable to that of the lifetimes of the vibrational coherences that are probed in VSFG spectroscopy. Thus, such dynamic processes can act as dephasing mechanisms that influence the intensity and shape of peaks in VSFG spectra. In the case of reorientation, the sensitivity of a VSFG measurement depends on the polarization configuration, the symmetry of the vibrational modes being probed, and the timing of the incident IR and probe pulses.[1, 2-5] Furthermore, reorientation can cause the same oscillator to encounter different dielectric environments on a time scale that is shorter than the vibrational coherence time, inducing a time dependence in the vibrational frequency. As described in Chapter Five, this reorientation-induced spectral diffusion (RISD) can influence VSFG spectra of vibrational modes, including modes that would not otherwise be sensitive to reorientation.[6]

Intermolecular vibrational coupling via transition dipole-transition dipole interactions can also play a role in VSFG spectra. The coupling strength, J, between two transition dipoles μ_1 and μ_2 that are separated by distance r is given by

$$J = \frac{\mu_1 \mu_2}{r^3}. \tag{7.1}$$

There are two limiting cases of such vibrational coupling that can be distinguished by the strength of the coupling relative to the vibrational linewidth, Γ. Förster transfer occurs when $J << \Gamma$, allowing an excitation to hop among oscillators. Efficient Förster transfer in the bulk generally requires molecules with large transition dipole moments, but this condition may be less important at an interface, where geometrical effects can dominate. Several groups have employed time-resolved VSFG spectroscopy to help shed light on vibrational Förster transfer at interfaces. Such experiments have made it possible to infer the time scale of energy transfer,[7] to distinguish energy transfer from other processes through isotopic dilution,[8] and to probe the surface coverage of monolayers on single crystal surfaces.[9] Because O-H groups have large transition dipoles, water exhibits intermolecular vibrational coupling that needs to be considered in the analysis of VSFG studies of this liquid.[10-12] Energy transfer between oscillators on the same molecule may also play a role in the VSFG spectroscopy of larger molecules.[8, 13]

When J becomes a sizable percentage of Γ, energy transfer occurs on the time scale of the vibrational motion.[1, 9] In this limit, the coupling is better described in terms of a vibrational exciton, in which energy becomes coherently delocalized over multiple molecules. This distinction has important implications for VSFG spectra. For example, Förster energy transfer causes dephasing and line broadening in a manner similar to

that of reorientation. As is the case for reorientation, Förster energy transfer has a greater influence on spectra of depolarized vibrational modes than on spectra of isotropic vibrational modes.[1] Excitonic coupling preserves vibrational coherence, but can influence VSFG spectra because the coherence is spread over many molecules. This phenomenon can affect VSFG measurements,[1, 11-12] but may also be mistaken for other dynamic processes.

The influence of resonance coupling on VSFG spectra is only beginning to be explored. Heterodyne-detected VSFG studies of the liquid water/vapor and ice/vapor interfaces[12, 14] observed a red shift and broadening of the O-H stretch that is associated with near-resonant coupling. These spectral changes mirror those in the bulk, but are less pronounced near an interface because molecules have fewer nearest neighbors.[12] Carbon monoxide adsorbed to ruthenium is also presumed to exhibit excitonic coupling at high enough surface coverages.[9]

In some of these situations, the *J* values alone may not seem large enough to suggest the presence of excitonic coupling. At an interface, however, other structural factors must be considered. For instance, when the distance between dipoles is closer than the distance between charge separation on the individual dipoles, coupling may be stronger than expected from a simple model.[14] Also, coupling is not necessarily only pairwise, but rather can extend over many nearest neighbors at a well-organized interface.

The liquid acetonitrile/silica interface, which has been described in detail in previous chapters, is used as a model system for exploring resonance coupling. Although evidence exists for a degree of resonance coupling of the cyano stretch of

acetonitrile in the bulk, leading to shifts among its isotropic and anisotropic Raman spectra and its IR spectrum,[23] such shifts would not necessarily be expected for the symmetric methyl stretch, as the methyl group has a smaller permanent dipole and a smaller transition dipole than does a cyano group.

Here I use VSFG spectroscopy to examine the acetonitrile methyl symmetric stretch at the acetonitrile/silica interface in mixtures with acetonitrile-d_3 over a broad range of concentrations. The dependence of the intensity and the line shape on the acetonitrile mole fraction cannot be described fully in terms of the properties of individual acetonitrile molecules, but is consistent with the presence of vibrational resonance coupling.

7.2 Experimental

The VSFG experiments were performed with a counterpropagating set-up that has been described in Chapter Three in Sections 3.1-3.3. The IR pulses had a pulse energy of 15 μJ centered at 2940 cm^{-1} with a bandwidth of 250 cm^{-1}, and the 800-nm probe pulses had a pulse energy of 15 μJ and a bandwidth of 5 cm^{-1}. The probe pulse was delayed with a motorized delay stage to arrive 667 fs after the IR pulse.

The chemicals used for the isotopically diluted acetonitrile solutions were 99+% spectroscopic grade acetonitrile (ACROS) and 99.5% (D-99.8%) acetonitrile-d_3 (Cambridge Isotope Laboratories). Concentrations ranging from 0.05 to 1 mole fraction of acetonitrile in acetonitrile-d_3 were used. All sample cuvettes were IR-grade quartz with a 1-mm pathlength (Hellma). Prior to use, the cuvettes were rinsed with acetone, methanol, and then water, after which they were oven-dried and then cleaned for 3 min in an oxygen plasma. Each sample was added to a clean cuvette, rather than performing

subsequent dilutions in the same cuvette, to avoid having any vestiges of the higher concentration mixtures remain behind, potentially influencing the subsequent measurement. Spectra were collected in the *SSP* polarization configuration. Three 60 s scans were performed at high acetonitrile mole fractions, and six 120 s scans were performed for mole fractions of 0.1 and lower. All spectra were normalized and calibrated according to the procedure described in Chapter Three, Sections 3.4-3.5.

7.3. Results and Discussion

The effect of isotopic dilution on the *SSP* VSFG spectrum of the methyl stretching region of liquid acetonitrile at the silica interface is shown in Figure 7.1(a). Spectra in this region consist of a strong peak at around 2943 cm^{-1} that corresponds to the symmetric methyl stretch. The strong signal indicates that the molecular axis has a large projection along the surface normal. The slight asymmetry is consistent with previously published results, and is believed to arise from the contribution of two oppositely phased peaks, with slightly different center frequencies and amplitudes, that correspond to the contributions from the two different sublayers of the LBL structure.[6, 16, 24-25] Upon dilution with acetonitrile-d_3, the spectrum undergoes a blue shift and narrowing, as can be seen in the normalized spectra in Figure 7.1(b). The spectra also become slightly more asymmetric upon dilution.

If the organization of the liquid remains unchanged upon isotopic dilution, then the VSFG intensity would be expected to scale with the square of the number of oscillators. Such behavior has been observed previously at the liquid/vapor interface of acetonitrile/acetonitrile-d_3 mixtures,[26] which indicates that isotopic dilution does not affect the organization of acetonitrile at this interface. In contrast, as shown in Figure

7.2(a), upon isotopic dilution the intensity at the acetonitrile/silica interface becomes larger than predicted by this model. Although the excess intensity is modest, it is clear from Figure 7.2(b) that there is a systematic trend in which the discrepancy between the observed and expected intensity grows with increasing acetonitrile-d_3 mole fraction.

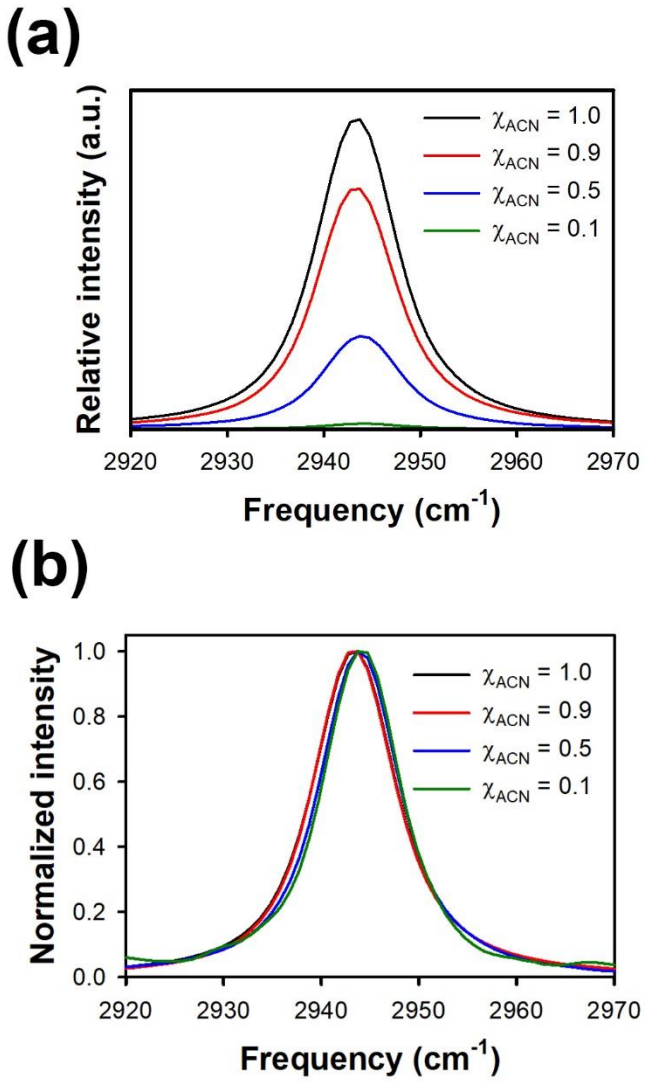

Figure 7.1. (a) VSFG spectra of liquid acetonitrile/acetonitrile-d_3 mixtures at a silica interface taken under *SSP* polarization conditions in the methyl-stretching spectral region. (b) Normalized spectra emphasize the blue shift, narrowing, and slight increase in asymmetry at low acetonitrile mole fractions.

The results from the liquid/vapor interface[26] suggest that the organization at the silica/liquid interface should not change upon isotopic dilution. As hydrogen bonds from surface silanols are accepted by the cyano groups, it is also unlikely that isotopic substitution of the methyl group influences partitioning to the silica surface. The viscosity of acetonitrile-d_3 is slightly larger than that of acetonitrile,[27] which will lead to somewhat slower orientational dynamics with increasing acetonitrile-d_3 mole fraction. However, the viscosity changes are modest, and reorientation has a minimal influence on the symmetric methyl stretch spectrum at this interface.[28] Furthermore, an increase in viscosity would also be expected to decrease the influence of RISD in the second sublayer of acetonitrile, which would decrease the VSFG intensity. Thus, we must search for another explanation for this intensity anomaly.

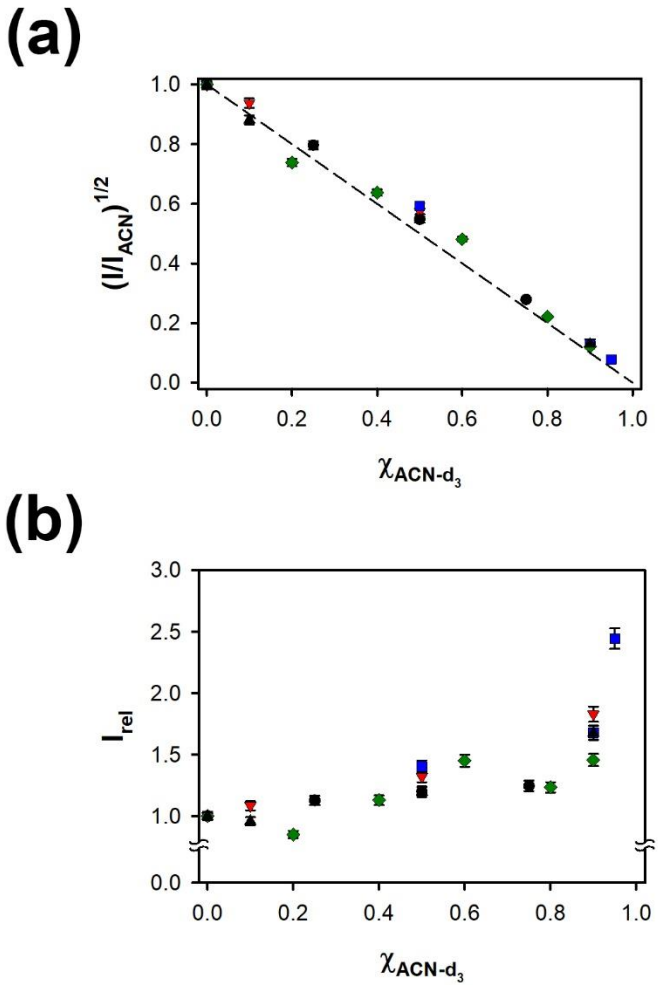

Figure 7.2. (a) The square root of the intensity, relative to that of the neat liquid, of the symmetric methyl stretch peak in *SSP* VSFG spectra of liquid acetonitrile at the silica interface as a function of mole fraction of acetonitrile-d_3. The dashed line is the result expected if the interfacial concentration mirrors that in the bulk. (b) The ratio of the observed intensity to the expected intensity. The different colors denote data obtained on different days.

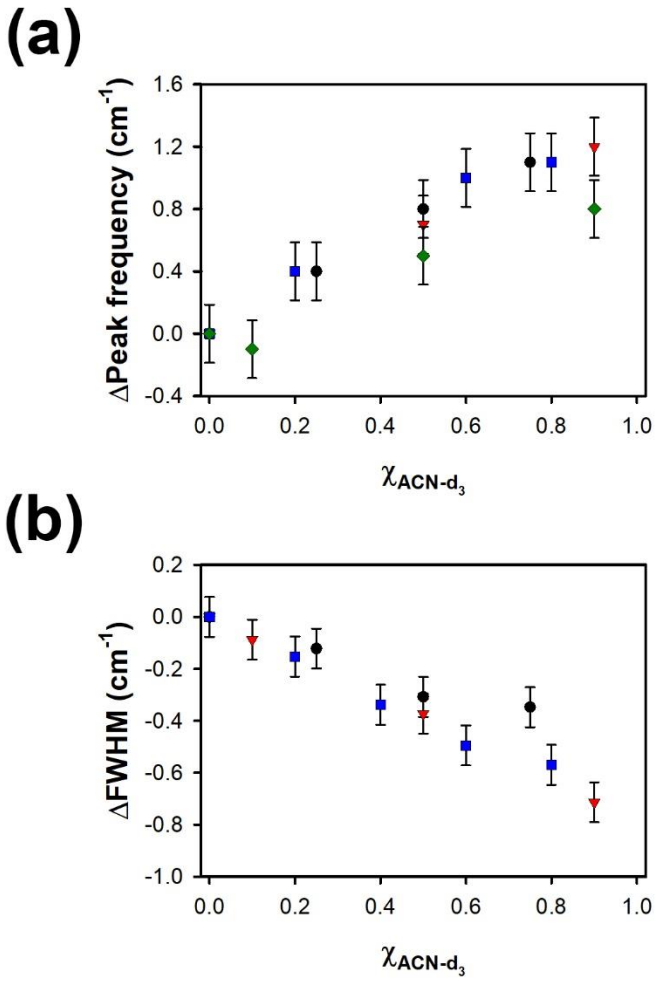

Figure 7.3. Dependence of (a) the peak frequency and (b) the linewidth of the symmetric methyl stretch peak in the VSFG spectrum of liquid acetonitrile at the silica interface as a function of the mole fraction of acetonitrile-d_3. The different colors denote data obtained on different days.

The spectral shift and line narrowing observed with increasing acetonitrile-d_3 mole fraction are quantified in Figs. 7.3(a) and 7.3(b), respectively. The overall spectral shift in going from pure acetonitrile to infinite dilution is 1.3 cm^{-1}, and the total decrease in the full width at half maximum (FWHM) is 0.7 cm^{-1} (7% of the FWHM in the neat liquid). Before considering the meaning of these observations, I first consider what is observed in the vibrational spectroscopy of the bulk mixtures.

Isotropic Raman difference spectroscopy studies of the influence of isotopic dilution on the symmetric methyl stretch of bulk acetonitrile have revealed a blue shift that is linear with concentration and reaches a value of 1.8 cm^{-1} at infinite dilution.[29-31] Isotropic Raman experiments performed on the bulk liquid indicate that the linewidth of the symmetric methyl stretch (6.0 cm^{-1}) does not change upon isotopic dilution.[32-33] At a 50% isotopic dilution, the IR linewidth for the symmetric methyl stretch has been observed to narrow slightly (from 13.4 cm^{-1} in the neat liquid to 13.1 cm^{-1}) and the depolarized Raman linewidth has been observed to decrease somewhat more substantially (from 14.0 cm^{-1} in the neat liquid to 12.2 cm^{-1}).[33]

This behavior was attributed by one group to static changes in the local dielectric environment,[29] as described by the model of Knapp and Fischer.[34] However, Raman echo experiments performed on the symmetric methyl stretch of pure acetonitrile indicated that there is negligible inhomogeneous broadening in the isotropic Raman spectrum of this mode.[35] A simple model of the extent of inhomogeneous broadening based on the spectral properties in the neat liquid and at infinite dilution supports this picture.[36] Furthermore the significantly narrower linewidth in the isotropic Raman spectrum indicates that reorientation plays a substantial role in the IR and depolarized Raman spectra, and the narrowing of these latter spectra may be the result of the abovementioned increase in viscosity.[27] Thus, it is doubtful that a static picture can account for the observed concentration dependences of the center frequency and linewidth in this system.

Another group attributed the behavior of the isotropic Raman spectrum of acetonitrile with isotopic dilution to resonant coupling.[31] To evaluate this possibility, it

is necessary to consider whether the structure of the bulk liquid promotes the proximity of methyl groups, such that the magnitude of *J* in Eq. (7.1) could be significant on average. As mentioned in early chapters, there is thought to be some propensity for acetonitrile molecules to dipole pair into antiparallel structures in the bulk liquid (Figure 7.4a).[21] The methyl groups in such structures are far enough from one another that resonant coupling would not be expected to be important. Hsu and Chandler showed that X-ray and neutron scattering data for liquid acetonitrile could be reproduced using a reference system that included only repulsive interactions.[37] They did find that liquid acetonitrile has a large degree of parallel ordering, but they attributed this ordering to the cylindrical shape of the molecule rather than dipole pairing.[37]

Pothoczki and Pusztai recently presented a sophisticated new analysis of orientational correlations in liquid acetonitrile, based on molecular dynamics simulations and reverse Monte Carlo simulations constrained by X-ray and neutron scattering data.[38] They found that the dominant conformation of antiparallel molecules at short range is not the traditional "head-to-head" dipole-paired structure, as in Figure7. 4a, but rather a "tail-to-tail" structure that brings methyl groups into close proximity (Figure 7.4b).[38] They further found that close approaches between two molecules in the liquid tend to involve hydrogen atoms.[38] This situation is the ideal for observing resonant coupling.

Based on this knowledge of the organization in bulk acetonitrile, the effects of isotopic dilution on the symmetric methyl stretch can be predicted based on equations developed to analyze the Raman noncoincidence effect (RNCE).[23, 39-40] The RNCE

refers to a shift between the first moments of the depolarized and isotropic Raman spectra of a specific mode. There is also an associated shift of the first moment of the IR spectrum of the same mode. These shifts result from different sensitivities to the angularly-dependent interaction potential that induces the vibrational frequency shift.[39-41] This interaction potential between two molecules *i* and *j* depends on the distance between and strength of the transition dipole moments, and the relative orientation of neighboring transition dipoles via[23]

$$V_{ij}^{(2)} = \frac{\mu^2}{r^3}\left[\boldsymbol{n_i}\cdot\boldsymbol{n_j} - \mathbf{3}(\boldsymbol{n_i}\cdot\boldsymbol{n})(\boldsymbol{n_j}\cdot\boldsymbol{n})\right] \quad , \tag{7.2}$$

where μ is the magnitude of the transition dipole, *r* is the distance between the transition dipoles, $\boldsymbol{n_k}$ is a unit vector along the transition dipole of molecule *k*, and $\boldsymbol{n}$ is the unit vector between the transition dipoles. The expressions for the first moments of the isotropic Raman, IR, and anisotropic Raman spectra are given by

$$\begin{aligned} M_{iso}^{(1)} &= \omega_0 + \frac{N_n}{2m\omega_0}\langle V^{(2)}P_0(\cos\theta)\rangle_{N_n} \\ M_{IR}^{(1)} &= \omega_0 + \frac{N_n}{2m\omega_0}\langle V^{(2)}P_1(\cos\theta)\rangle_{N_n} \quad , \\ M_{aniso}^{(1)} &= \omega_0 + \frac{N_n}{2m\omega_0}\langle V^{(2)}P_2(\cos\theta)\rangle_{N_n} \end{aligned} \tag{7.3}$$

where ω_0 is the bare vibrational frequency, N_n is the number of coupled oscillators, P_n is the nth-order Legendre polynomial, θ is the angle between transition dipoles, and the angular brackets indicate averaging over all pairs of molecules.

The prototypical situation in which the RNCE is observed in a bulk liquid is for species with polar functional groups that are not sterically hindered and have large transition dipole moments. A representative example is the carbonyl stretch of acetone,

for which the depolarized Raman peak and the IR absorption peak are both shifted by about 5 cm^{-1} to the blue of the isotropic Raman peak.[23]

C-H stretching modes have moderate transition dipoles that are on the order of 0.05-0.3 × 10^{-30} C-m,[42-45] as compared to on the order of 10 × 10^{-30} C-m for a carbonyl stretch. This relatively small transition dipole and the fact that methyl groups are not polar accounts for the fact that the RNCE is not usually considered for methyl groups in bulk liquids. However, even if the shifts between the isotropic Raman spectrum and IR spectrum or the depolarized Raman spectrum are small, resonant coupling can still lead to a shift in all of these spectra that will disappear with isotopic dilution.

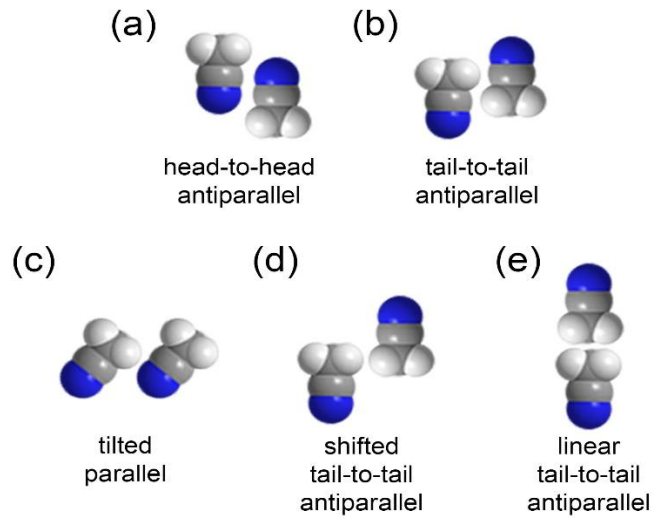

Figure 7.4. Local pair configurations of liquid acetonitrile molecules considered in the analysis of resonance coupling for the symmetric methyl stretch.

In Table 7.1 the signs and magnitudes of the various components of Eq. (7.2) and Eq. (7.3) for the symmetric methyl stretch for different local structures of pairs of molecules are shown. The predominant tail-to-tail structure is expected to cause a red shift in the isotropic and depolarized Raman spectra and a blue shift in the IR spectrum. The fact that the isotropic Raman spectrum is homogeneously broadened[35] indicates

that the vibrational lifetime is long enough that the majority of methyl groups can sample the tail-to-tail structure due to reorientation before dephasing is complete. One may conclude that the blue shift of the isotropic Raman spectrum upon isotopic dilution is due to the decreasing importance of such resonant coupling.

Table 7.1. Sizes and magnitudes of terms contributing to the shifts in Eq. (7.3) for the idealized local configurations shown in Figure 7.4.

Geometry	$\boldsymbol{n_i \cdot n_j}$	$-(\boldsymbol{n_i \cdot n}) \cdot (\boldsymbol{n_j \cdot n})$	$1/r^3$	$P_1(\cos\theta)$	$P_2(\cos\theta)$	Isotropic Raman shift	IR shift	Anisotropic Raman shift
head-to-head antiparallel	-1	+ med	small	- large	+ large	red small	blue small	red small
tail-to-tail antiparallel	-1	+ small	large	- large	+ large	red med	blue med	red med
tilted parallel	+1	- med	med	+ large	+ large	red small	red small	red small
shifted tail-to-tail	-1	~0	large	- large	+ large	red large	blue large	red large
linear tail-to-tail	-1	+ large	large	- large	+ large	blue large	red large	blue large

The influence of resonant coupling on VSFG spectra of the acetonitrile symmetric methyl stretch at the silica/liquid interface will now be considered. The expression for the $\chi^{(2)}$ tensor element of the symmetric methyl stretch that is probed in an *SSP* polarization configuration is[1]

$$\chi^{(2)}_{eff,SSP} \propto \mu_z \left(\alpha_I - \frac{1}{6}\alpha_A\right)\langle\cos\theta\rangle + \frac{1}{2}\mu_z\alpha_A\langle\cos^3\theta\rangle\,, \tag{7.4}$$

where μ is the IR transition dipole, α_I and α_A are the change in the isotropic and anisotropic component of the polarizability tensor, and θ is the angle between the transition dipole and the surface normal. As discussed above, α_I is the dominant Raman

term in the polarizability for a symmetric methyl stretch. Additionally, the two terms in Eq. (7.4) that depend on α_A are of opposite sign, further weakening the influence of the anisotropic portion of the polarizability. The VSFG spectral shift will therefore be interpreted here based on the behavior of the IR spectrum and the isotropic Raman spectrum.

The tail-to-tail structure in Figure 7.4b is not common at the silica/liquid interface, because it prevents the formation of a well-packed first sublayer. Instead, almost all of the acetonitrile molecules in this first sublayer at a silica surface have their cyano groups pointing towards the surface, and make an average angle of 40° from the surface normal.[15-16] Thus, molecules whose methyl groups are in close proximity in the first sublayer are likely to have a tilted parallel organization (Figure 7.4c). This sort of organization leads to a red shift for the isotropic and depolarized Raman spectra, as well as for the IR spectrum. However, the shifts are expected to be smaller than those for the tail-to-tail structure.

Molecules in the second sublayer are more disordered, with approximately 60% of the methyl groups pointed toward the surface and 40% pointed away.[15-16] The methyl groups that point toward the interface can form shifted tail-to-tail structures (Figure 7.4d) or even linear tail-to-tail structures (Fig 7.4e). As shown in Table 7.1, in the former case there will be a red shift of the isotropic and depolarized Raman spectra and in the latter case there should be a blue shift. There will be an opposite shift of the IR spectrum in both cases. Thus, the second sublayer should act to reduce the overall red shift that arises from the first sublayer. The effect of the second sublayer on the first sublayer should be tempered somewhat by the small frequency shift between the

methyl groups in the two sublayers.[16] This analysis is completely consistent with a red shift that is smaller than the magnitude that is observed in the bulk liquid, despite the considerably greater organization at the interface.

These results demonstrate the necessity of determining the extent of intermolecular vibrational coupling when attempting any sort of quantitative orientational analysis using VSFG spectroscopy. Surface interactions can promote both the proximity of identical functional groups and the alignment of their transition dipoles. This phenomenon is particularly important for molecules with large transition dipoles. For example, the relative strengths of VSFG signals measured with the *SPS* and *SSP* polarization configurations are commonly used to determine average orientation.[46] When probing symmetric stretches in systems with azimuthal symmetry, the *SPS* signal is sensitive to the anisotropic polarizability, whereas the *SSP* signal is dominated by the isotropic contribution. Because shifts from transition dipole coupling are larger for the isotropic first moment than for the anisotropic first moment, *SSP* and *SPS* spectra are affected differently by the resonance coupling. Similarly, *SSP* spectra may be shifted from the *PPP* because of the relative dominance of α_I for *SSP* measurements and α_A for *PPP* measurements. *PPP* spectra always require careful analysis, because they contain contributions from four different susceptibility elements, each of which has a different dependence on α_I and α_A. The analysis of any VSFG technique that employs changes in the experimental geometry to emphasize different elements should take transition dipole coupling into consideration.

7.4. Conclusions

I have presented a VSFG study of the methyl symmetric stretch of liquid acetonitrile at a silica interface for a series of mixtures of acetonitrile with its deuterated isotopologue. I was able to obtain spectra down to an acetonitrile mole fraction of 0.05, and to resolve small changes in line shape. The VSFG spectra exhibit a blue shift and a narrowing with isotopic dilution, and the intensity of the spectrum is higher than predicted, particularly at low acetonitrile concentrations. These spectral changes are consistent with the influence of intermolecular vibrational coupling, which induces a shift between the IR, the isotropic Raman, and the anisotropic Raman first moments. These results emphasize the importance of evaluating the effect of resonance coupling on VSFG spectra, particularly in samples with substantial transition dipole moments. It would be of great interest to perform similar experiments using the C-N stretch of acetonitrile as a probe of resonance coupling.

7.5 References

1. Rivera, C. A.; Fourkas, J. T., Reexamining the interpretation of vibrational sum-frequency generation spectra. *Int. Rev. Phys. Chem.* **2011,** *30* (4), 409-443.

2. Fourkas, J. T.; Walker, R. A.; Can, S. Z.; Gershgoren, E., Effects of reorientation in vibrational sum-frequency spectroscopy. *J. Phys. Chem. C* **2007,** *111*, 8902-8915.

3. Malyk, S.; Shalhout, F. Y.; O'Leary, L. E.; Lewis, N. S.; Benderskii, A. V., Vibrational Sum Frequency Spectroscopic Investigation of the Azimuthal Anisotropy and Rotational Dynamics of Methyl-Terminated Silicon(111) Surfaces. *J. Phys. Chem. C* **2013,** *117* (2), 935-944.

4. Vinaykin, M.; Benderskii, A. V., Orientational Dynamics in Sum Frequency Spectroscopic Line Shapes. *J. Phys. Chem. B* **2013,** *117* (49), 15833-15842.

5. Wei, X.; Shen, Y. R., Motional effect in surface sum-frequency vibrational spectroscopy. *Phys. Rev. Lett.* **2001,** *86*, 4799-4802.

6. Rivera, C. A.; Souna, A. J.; Bender, J. S.; Manfred, K.; Fourkas, J. T., Reorientation-induced spectral diffusion in vibrational sum-frequency-generation spectroscopy. *J. Phys. Chem. B* **2013,** *117* (49), 15875-85.

7. Sass, M.; Lobau, J.; Lettenberger, M.; Laubereau, A., Vibrational energy transfer of chemisorbed ethyltrichlorosilane at the glass/air interface. *Chem. Phys. Lett.* **1999,** *311* (1-2), 13-20.

8. Yamamoto, S.; Ghosh, A.; Nienhuys, H. K.; Bonn, M., Ultrafast inter- and intramolecular vibrational energy transfer between molecules at interfaces studied by time- and polarization-resolved SFG spectroscopy. *Phys. Chem. Chem. Phys.* **2010,** *12* (40), 12909-12918.

9. Bonn, M.; Hess, C.; Wolf, M., The dynamics of vibrational excitations on surfaces: CO on Ru(001). *J. Chem. Phys.* **2001,** *115* (16), 7725-7735.

10. McGuire, J. A.; Shen, Y. R., Ultrafast vibrational dynamics at water interfaces. *Science* **2006,** *313* (5795), 1945-1948.

11. Schaefer, J.; Backus, E. H. G.; Nagata, Y.; Bonn, M., Both inter- and intramolecular coupling of O-H groups determine the vibrational response of the water/air interface. *J. Phys. Chem. Lett.* **2016,** *7* (22), 4591-4595.

12. Smit, W. J.; Versluis, J.; Backus, E. H. G.; Bonn, M.; Bakker, H. J., Reduced near-resonant vibrational coupling at the surfaces of liquid water and ice. *J. Phys. Chem. Lett.* **2018,** *9* (6), 1290-1294.

13. Ricks, A. M.; Anfuso, C. L.; Rodriguez-Cordoba, W.; Lian, T. Q., Vibrational relaxation dynamics of catalysts on TiO_2 Rutile (110) single crystal surfaces and anatase nanoporous thin films. *Chem. Phys.* **2013,** *422*, 264-271.

14. Hirschfelder, J. O.; Curtiss, C. F.; Bird, R. B., *Molecular Theory of Gases and Liquids*. John Wiley & Sons: New York, 1954.

15. Hu, Z.; Weeks, J. D., Acetonitrile on silica surfaces and at its liquid-vapor interface: Structural correlations and collective dynamics. *J. Phys. Chem. C* **2010,** *114* (22), 10202-10211.

16. Ding, F.; Hu, Z.; Zhong, Q.; Manfred, K.; Gattass, R. R.; Brindza, M. R.; Fourkas, J. T.; Walker, R. A.; Weeks, J. D., Interfacial organization of acetonitrile: Simulation and experiment. *J. Phys. Chem. C* **2010,** *114* (41), 17651-17659.

17. Morales, C. M.; Thompson, W. H., Simulations of infrared spectra of nanoconfined liquids: Acetonitrile confined in nanoscale, hydrophilic silica pores. *J. Phys. Chem. A* **2009,** *113* (10), 1922-1933.

18. Cheng, L.; Morrone, J. A.; Berne, B. J., Structure and dynamics of acetonitrile confined in a silica nanopore. *J. Phys. Chem. C* **2012,** *116* (17), 9582-9593.

19. Mountain, R. D., Molecular dynamics simulation of water-acetonitrile mixtures in a silica slit. *J. Phys. Chem. C* **2013,** *117* (8), 3923-3929.

20. Loughnane, B. J.; Farrer, R. A.; Scodinu, A.; Fourkas, J. T., Dynamics of a wetting liquid in nanopores: An optical Kerr effect study of the dynamics of acetonitrile confined in sol-gel glasses. *J. Chem. Phys.* **1999,** *111* (11), 5116-5123.

21. Saito, H.; Tanaka, Y.; Nagata, S.; Nukada, K., ^{13}C nuclear magnetic resonance studies on molecular association. I. Self-association of dipolar molecules. *Can. J. Chem.* **1973,** *51* (13), 2118-2123.

22. Berne, B. J.; Fourkas, J. T.; Walker, R. A.; Weeks, J. D., Nitriles at Silica Interfaces Resemble Supported Lipid Bilayers. *Acc. Chem. Res.* **2016,** *49* (9), 1605-1613.

23. Giorgini, M. G., Raman noncoincidence effect: A spectroscopic manifestation of the intermolecular vibrational coupling in dipolar molecular liquids. *Pure Appl. Chem.* **2004,** *76* (1), 157-169.

24. Rivera, C. A.; Bender, J. S.; Manfred, K.; Fourkas, J. T., Persistence of acetonitrile bilayers at the interface of acetonitrile/water mixtures with silica. *J. Phys. Chem. A* **2013,** *117* (46), 12060-6.

25. Souna, A. J.; Clark, T. L.; Fourkas, J. T., Effect of temperature on the organization of acetonitrile at the silica/liquid interface. *J. Phys. Chem. C* **2017,** *121* (47), 26432-26437.

26. Kim, J.; Chou, K. C.; Somorjai, G. A., Structure and dynamics of acetonitrile at the air/liquid interface of binary solutions studied by infrared−visible sum frequency generation. *J. Phys. Chem. B* **2003,** *107* (7), 1592-1596.

27. Loughnane, B. J.; Scodinu, A.; Farrer, R. A.; Fourkas, J. T.; Mohanty, U., Exponential intermolecular dynamics in optical Kerr effect spectroscopy of small-molecule liquids. *J. Chem. Phys.* **1999,** *111* (6), 2686.

28. Liu, S. L.; Fourkas, J. T., Orientational time correlation functions for vibrational sum-frequency generation. 1. Acetonitrile. *J. Phys. Chem. A* **2013,** *117* (29), 5853-5864.

29. Asthana, B. P.; Deckert, V.; Shukla, M. K.; Kiefer, W., Isotopic dilution study of self association in (CH_3CN+CD_3CN) mixture by scanning multichannel Raman difference technique and ab-initio calculations. *Chem. Phys. Lett.* **2000,** *326* (1-2), 123-128.

30. Kamogawa, K.; Kitagawa, T., Raman difference spectroscopy of the C-H stretching vibrations: Frequency shifts and excess quantities for acetone/water and acetonitrile/water solutions. *J. Phys. Chem.* **1986,** *90* (6), 1077-1081.

31. Kamogawa, K.; Kitagawa, T., A new device for Raman difference spectroscopy and its application to observe frequency shifts due to isotope mixing. *J. Phys. Chem.* **1990,** *94* (10), 3916-3921.

32. Marri, E.; Morresi, A.; Paliani, G.; Cataliotti, R. S.; Giorgini, M. G., Isotopic and chemical dilution effects on the vibrational relaxation rate of some totally symmetric motions of liquid acetonitrile. *Chem. Phys.* **1999,** *243* (3), 323-332.

33. Morresi, A.; Ombelli, M.; Sassi, P.; Santini, S., Light and deuterated acetonitrile: An unresolved casus? *J. Raman Spectrosc.* **2002,** *33* (2), 71-79.

34. Knapp, E. W.; Fischer, S. F., The concentration dependence of the vibrational linewidth and shift in liquid binary mixtures: An analytical model. *J. Chem. Phys.* **1982,** *76* (10), 4730-4735.

35. Vanden Bout, D.; Muller, L. J.; Berg, M., Ultrafast Raman echoes in liquid acetonitrile. *Phys. Rev. Lett.* **1991,** *67* (26), 3700-3703.

36. Muller, L. J.; Vanden Bout, D.; Berg, M., Broadening of vibrational lines by attractive forces: Ultrafast Raman echo experiments in a CH_3I:$CDCl_3$ mixture. *J. Chem. Phys.* **1993,** *99* (2), 810-819.

37. Hsu, C. S.; Chandler, D., RISM calculation of the structure of liquid acetonitrile. *Mol. Phys.* **1978,** *36* (1), 215-224.

38. Pothoczki, S.; Pusztai, L., Intermolecular orientations in liquid acetonitrile: New insights based on diffraction measurements and all-atom simulations. *J. Mol. Liq.* **2017,** *225*, 160-166.

39. Logan, D. E., The non-coincidence effect in the Raman spectra of polar liquids. *Chem. Phys.* **1986,** *103* (2-3), 215-225.

40. McHale, J. L., The influence of angular dependent intermolecular forces on vibrational spectra of solution phase molecules. *J. Chem. Phys.* **1981,** *75* (1), 30-35.

41. Wang, C. H.; McHale, J., Vibrational resonance coupling and the noncoincidence effect of the isotropic and anisotropic Raman spectral components in orientationally anisometric molecular liquids. *J. Chem. Phys.* **1980,** *72* (7), 4039-4044.

42. Bertie, J. E.; Apelblat, Y.; Keefe, C. D., Infrared intensities of liquids XXV: Dielectric constants, molar polarizabilities and integrated intensities of liquid toluene at 25 °C between 4800 and 400 cm^{-1}. *J. Mol. Struct.* **2005,** *750* (1-3), 78-93.

43. Biliškov, N., Infrared optical constants, molar absorption coefficients, dielectric constants, molar polarisabilities, transition moments and dipole moment derivatives of liquid N,N-dimethylacetamide-carbon tetrachloride mixtures. *Spectrochim. Acta A Mol. Biomol. Spectrosc.* **2011,** *79* (2), 295-301.

44. Biliškov, N., Infrared optical constants, molar absorption coefficients, dielectric constants, molar polarisabilities, transition moments and dipole moment derivatives of liquid N,N-dimethylformamide-carbon tetrachloride mixtures. *Spectrochim. Acta A Mol. Biomol. Spectrosc.* **2011,** *79* (2), 302-307.

45. Keefe, C. D.; Pickup, J. E., Infrared optical constants, dielectric constants, molar polarizabilities, transition moments, dipole moment derivatives and Raman spectrum of liquid cyclohexane. *Spectrochim. Acta A Mol. Biomol. Spectrosc.* **2009,** *72* (5), 947-953.

46. Wang, H.-F.; Gan, W.; Lu, R.; Rao, Y.; Wu, B.-H., Quantitative spectral and orientational analysis in surface sum frequency generation vibrational spectroscopy (SFG-VS). *Int. Rev. Phys. Chem.* **2005,** *24*, 191-256.

Chapter 8: Probing Aprotic Electrolyte Solutions at Solid Interfaces Using the Acetonitrile/Silica Interface as a Model System: An Ion Transport and VSFG Spectroscopy Study

Adapted from: Souna, A. J.; Polster, J.; Tran, J. D.; Fourkas, J. T.; and Siwy, Z. (in preparation for publication)
VSFG spectroscopy research designed by: Amanda J. Souna
VSFG spectroscopy research conducted by: Amanda J. Souna and Jason D. Tran
Ion transport research designed and conducted by: Jake Polster
Authored by: Amanda J. Souna, Zuzanna Siwy, and John T. Fourkas

8.1 Introduction

The surface potential plays an important role in many chemical and physical processes at solid/liquid interfaces. When the liquid phase is aqueous, the surface potential is often dominated by surface charges. For instance, surfaces composed of silica or polymers that contain carboxylic acid groups tend to deprotonate in aqueous solutions, creating a negative surface potential. The situation is less clear, however, when the liquid phase is a solvent that is aprotic and/or is not a strong base. For instance, recent experiments on ion transport in electrolyte solutions in propylene carbonate or acetonitrile through nanopores composed of polycarbonate or silica have revealed an effective positive surface charge, even though the same materials would have a negative surface charge in an aqueous solution.[1] It was proposed that this positive surface charge arises from dipole ordering of the solvents at the surfaces of the nanopores.[1]

One of the motivations to determine ion and solvent organization at solid interfaces is to understand the mechanisms of electrochemical processes, especially for nanostructured materials for which surface interactions dominate. These materials often make use of lithium-based electrolytes, with the requirement that lithium ions be

highly mobile and have a stable and inert counterion.[2] A good solvent for lithium salts must have a high dielectric constant to dissolve the salts effectively, and a low viscosity to promote ion transport. The solvent should also be inert near other components.[2] Acetonitrile meets all of these requirements. It is a liquid composed of relatively simple molecules, and its interactions with electrolytes have been studied extensively in the bulk.[3-6] Therefore, acetonitrile is a good representative solvent for exploring aprotic electrolyte solutions at solid surfaces.

Here we use a combination of ion transport measurements, vibrational sum-frequency generation (VSFG) spectroscopy, and molecular dynamics (MD) simulations to develop a detailed understanding of the behavior of solutions of alkali salts in acetonitrile at silica surfaces. The electrolytes studied are commonly used in batteries and have a high solubility in acetonitrile. The role of the cations and anions is distinguished by using salts with either the cation in common ($LiClO_4$, $LiBF_4$, and $LiPF_6$) or the anion in common ($LiClO_4$ and $NaClO_4$). I demonstrate that the positive effective surface charge is a manifestation of the induced organization of the solvent. This behavior is a consequence of the intrinsic charge distribution of the organized liquid at the interface, a phenomenon that has not previously been considered in the analysis of VSFG spectra.

8.2 Background on Ion Transport Experiments

Ion current measurements are based on measuring electrokinetic transport of ions in single pores. A detailed description of these methods along with the preparation of nanopores can be found in Reference 1. Single glass pipettes with an opening of 400 nm were placed in contact with a series of electrolyte solutions of different

concentrations in acetonitrile. The observation of rectification in this experiment indicates that the pipette carries an effective surface potential, so that for one voltage polarity the tip of the pipette is electroosmotically filled with the solution of lower concentration, leading to overall lower conductance of the pipette. For the opposite voltage polarity, electroosmosis draws the more concentrated solution of higher conductivity into the pipette so that larger currents are observed. If there were no effective surface potential on the pipette inner wall, in the absence of electroosmosis, ionic concentrations in the pipette would be voltage independent and the current-voltage curve would be linear.

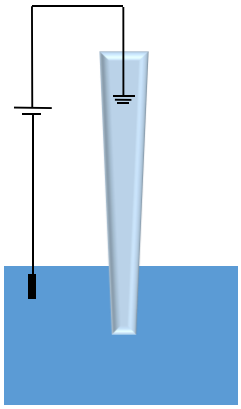

Figure 8.1. Experimental set-up for the measurement of current-voltage curves through a glass pore. The electrolyte solutions inside the 400-nm glass pipette and in the bulk solution are of different concentrations.

The direction of rectification carries information on the polarity of the effective potential. The results for $LiClO_4$ solutions are shown in Figure 8.2, where the first concentration written indicates the pipette concentration, and the second indicates the bulk concentration. For the concentration gradients 1 mM/10 mM, 10 mM / 100 mM and 10 mM / 1 M, negative currents were higher than positive currents, indicating that for negative voltages the pipette was filled with the solution in the bulk. With the

ground electrode placed in the pipette, electroosmotic flow could be directed from the bulk towards the pipette only if the surface potential was positive. The larger pipette diameter of 400 nm was chosen to assure that the screening length of the effective surface potential is significantly smaller than the pipette opening. Consequently, it can be assumed that the concentration of ions in the pore is determined by the bulk solution brought to the pore via electroosmosis. The same effect occurred when glass pipettes were replaced with polyimide (DuPont Kapton 50 HN) nanopores, which contain carboxyl groups on the pore wall. Only for the 0.1 mM/1 mM concentration gradient was rectification in the opposite direction, as shown in the inset of Figure 8.2. In contrast, the direction of rectification in $LiClO_4$ solutions in water showed the opposite of what was observed in acetonitrile for the same set of solutions, i.e. in the same electrode configurations positive currents were higher than negative currents. It should be noted that all of the results summarized here were obtained in a glove box under an argon atmosphere to avoid the deprotonation of silanol groups by residual water.

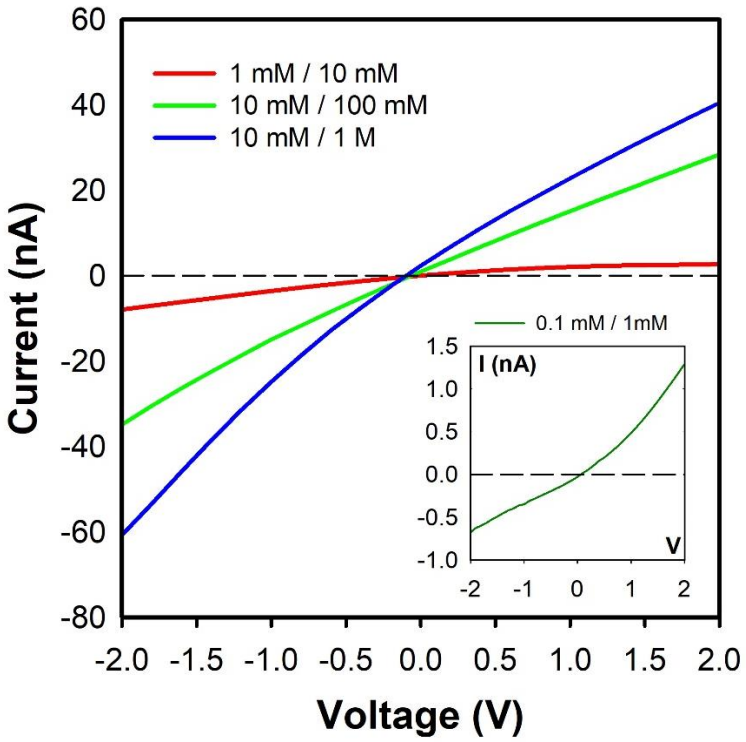

Figure 8.2. Current-voltage curves for lithium perchlorate at four concentration differentials. The designation 1 mM / 10 mM indicates that the pipette concentration is 1 mM and the bulk concentration is 10 mM. The three highest concentrations exhibit rectification showing a positive surface potential, whereas the lowest concentration (inset) shows a negative surface potential.

The degree of rectification is traditionally calculated with a value known as R, calculated as the ratio of current magnitudes at -1V and +1V. To compare the magnitudes of rectification in opposite directions (for those in which R is either < 1 or > 1), while also correcting for the higher currents at higher electrolyte concentrations, we calculated rectification direction and magnitude using quantity we call the current anisotropy, r_I:

$$r_I(V) = \frac{-(I(V)+I(-V))}{I(V)-I(-V)} \tag{8.1}$$

The current anisotropy has the same sign as the surface charge, and is zero in the absence of surface charge, in which case no rectification is observed. For all of the

experiments discussed here, we chose to use a voltage of 2 V to measure current anisotropy.

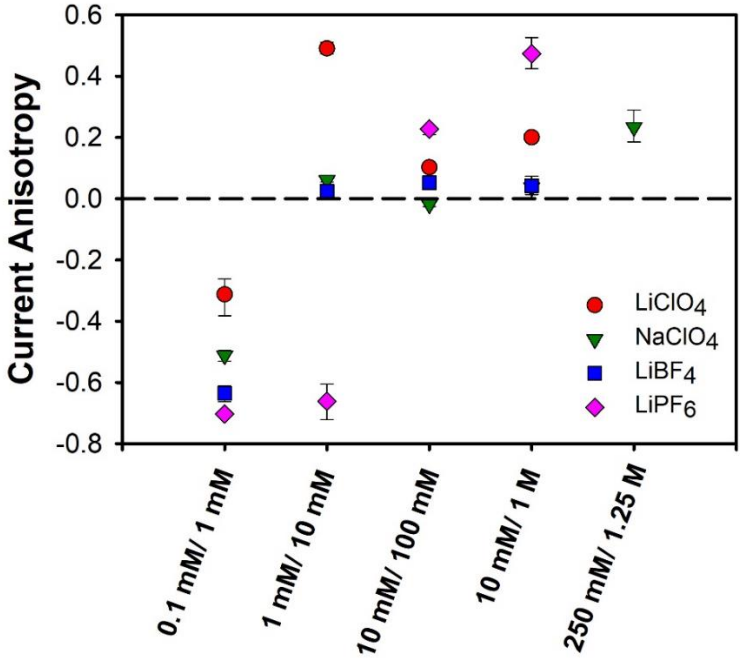

Figure 8.3. Current anisotropy for four different electrolyte solutions in acetonitrile in glass nanopores. Current anisotropy is evaluated using equation 8.1.

The current anisotropies for the ion current measurements conducted with four different electrolyte solutions are plotted in Figure 8.3. The figure shows that at 0.1 mM / 1 mM, for all salts, r_I is negative, indicating a negative surface charge. $LiClO_4$ shows the weakest rectification at this concentration gradient. At the 1 mM / 10 mM gradient, the negative surface charge disappears for all salts except $LiPF_6$. $LiClO_4$ exhibits a positive surface charge that starts to decrease somewhat at higher concentrations. $NaClO_4$ only develops a positive charge at the highest concentrations, $LiBF_4$ never exhibits a positive surface charge, and $LiPF_6$ begins to show a positive surface charge only at the highest concentrations at which point the r_I has a magnitude similar to that of $LiClO_4$ at its maximum. The origins of the differences in rectification

behavior between the four electrolytes will be identified with the VSFG results presented in the following section.

8.3 VSFG Experimental Methods

The VSFG spectra were collected with a counter-propagating VSFG spectrometer that has been described in detail in Chapter Three, Sections 3.1-3.3. All spectra were collected according to the methods described in Section 3.4. For this study, the IR pulse had an energy of 15 μJ and a bandwidth of 250 cm^{-1}. The probe pulses had an energy of 15 μJ and a bandwidth of 5 cm^{-1}. The probe pulses were delayed relative to the IR pulse by 667 fs to maximize the probe pulse's overlap with the molecular response of the methyl symmetric stretch transition.

Acetonitrile (HPLC grade, Fisher-Scientific) was distilled over calcium hydride under argon gas and stored over molecular sieves in an argon-filled glove box for at least 24 h. $LiClO_4$ and $LiPF_6$ were ≥99.99% battery grade (Sigma Aldrich). $LiBF_4$ was 98% purity, and anhydrous (ACROS Organics). $NaClO_4$ was 98.0% ACS grade (Sigma Aldrich). $LiClO_4$ came in a sealed ampoule and was used as received without further drying. All other salts were dried under vacuum at 100 °C (120 °C for $LiBF_4$) for 24 h. All solutions were prepared in the glove box using glassware that had been dried in a 165 °C oven overnight. Electrolyte solutions had concentrations that ranged from 1 nanomole to 1 mole per liter of solvent (1.27 molal) for $LiClO_4$ and $LiPF_6$, 2.54 molal for $NaClO_4$, and 3.81 molal for $LiBF_4$. (These concentrations will be denoted using molarity: 1.27 molal = 1 M). A quantity of neat acetonitrile equal to that of the solutions was also prepared as a control. Dry acetonitrile and 1 M solutions of each electrolyte were tested for water content using Karl Fischer titration (899 Coulometer,

Metrohm). Acetonitrile had a water content of 25-50 ppm, and the electrolyte solutions contained between 80-200 ppm.

Sample cuvettes were rinsed with acetone, methanol, and water, oven dried, cleaned for 3 m in an oxygen plasma, and dried overnight. Cuvettes were placed in the glove box while still hot. After they had cooled, each was filled with dry acetonitrile as a reference. All sample vials and cuvettes were removed from the glove box prior to collecting spectra. Dry acetonitrile spectra were collected within one hour of removing the samples from the glove box, during which time the cuvettes remained tightly capped. The spectra from subsequent cuvettes of dry acetonitrile remained the same, indicating that a negligible amount of ambient water entered the cuvettes and reached the silica surface. After references were collected, the neat acetonitrile and the series of electrolyte solutions that were removed from the glove box were added to each of the reference cuvettes, replacing the dry acetonitrile, after flushing twice with the new sample.

The spectra were obtained using the *SSP* polarization configuration, which is defined in Chapter Two, Section 2.1. Normalization and calibration spectra were obtained according to the method described in Section 3.4 of Chapter Three. Acquisition times for low concentrations of electrolyte solutions were 1 m. For higher concentrations, acquisition times were two to four times those of the low concentrations depending on the signal strength. All scans were repeated at least three times.

8.4 VSFG spectroscopy results

Shown in Figure 8.4 are the VSFG spectra in the C-H stretching region for solutions of $LiClO_4$, $LiPF_6$, $NaClO_4$, and $LiBF_4$ in acetonitrile at a range of

concentrations. The corresponding height-normalized spectra are shown in Figure 8.5. The *SSP* polarization combination is sensitive to modes with an infrared transition dipole that has a projection along the surface normal. At all concentrations of solutions, the only mode that appears is the symmetric methyl stretch.

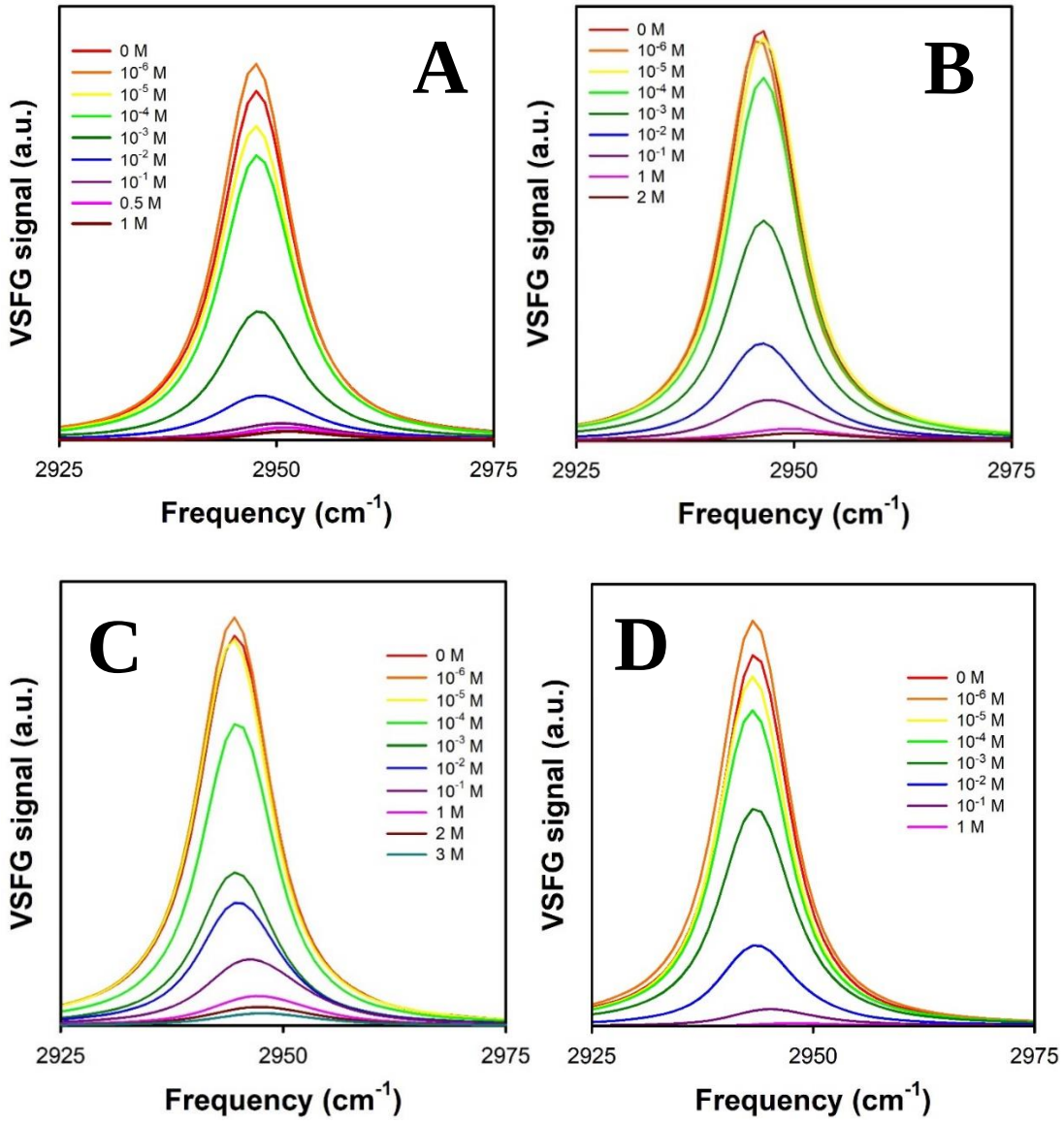

Figure 8.4. VSFG spectra of (A) $LiClO_4$, (B) $NaClO_4$, (C) $LiBF_4$, and (D) $LiPF_6$ in acetonitrile at a silica interface. The spectra were measured in the methyl symmetric stretch region.

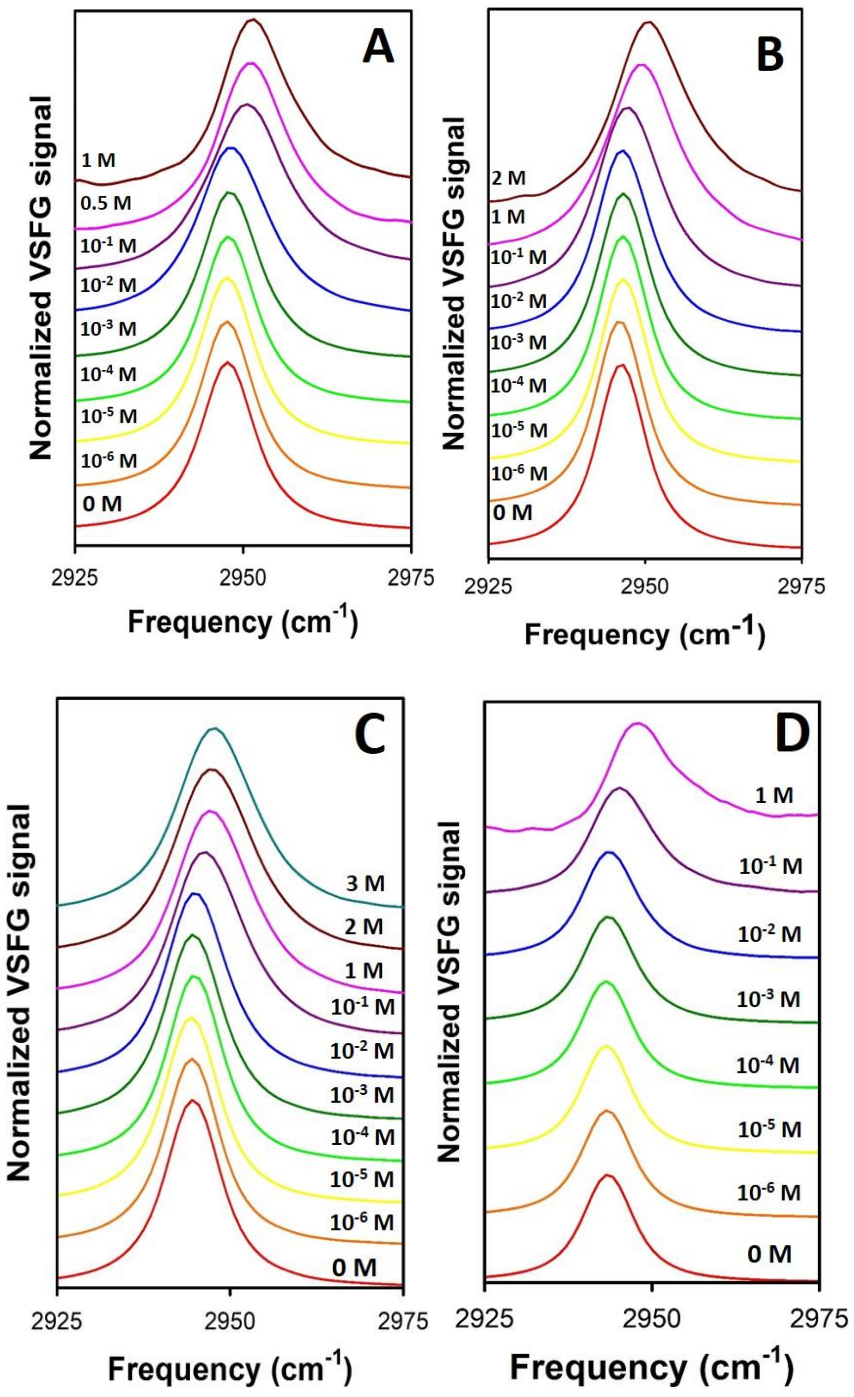

Figure 8.5. Normalized VSFG spectra of (A) $LiClO_4$, (B) $NaClO_4$, (C) $LiBF_4$, and (D) $LiPF_6$ in acetonitrile at a silica interface. The spectra were measured in the methyl symmetric stretch region.

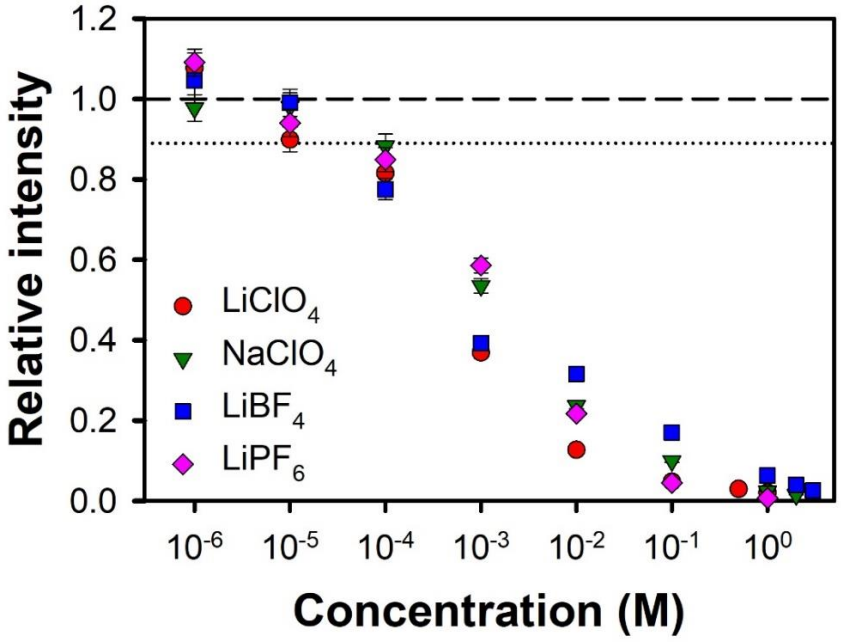

Figure 8.6. VSFG peak intensities of four electrolyte solutions in acetonitrile relative to the peak intensity of neat acetonitrile. The dotted line indicates the peak intensity of dry acetonitrile. The dashed line indicates the peak intensity of acetonitrile that was briefly exposed to ambient air while filling the sample cuvette. The electrolyte solutions were similarly exposed to ambient air, so relative intensity points are normalized to the wet acetonitrile.

The key features of the concentration dependent VSFG spectra are quantified in Figures 8.6-8.8. (In these figures, the data points from 10^{-9} M to 10^{-7} M are omitted for clarity, however, these concentrations show the same features as the 10^{-6} M samples.) Concentration regimes for each salt are defined in Table 8.1. These regimes correspond to the concentration ranges for which r_I is negative ("very low" concentration), zero or approaching zero ("low" concentration), positive ("intermediate" concentration), and positive but decreasing ("high" concentration). Each category corresponds to VSFG trends that will be described in detail in Sections 8.5.2 and 8.5.3 and illustrated in Figure 8.10. In Figure 8.6, the relative intensities of the spectra, as determined from the peak heights, are shown. The spectral intensity first

increases somewhat with the addition of electrolyte, before decreasing. The intensity is less than that of neat acetonitrile for concentrations of 10 μM and higher, with intensities of all electrolyte solutions showing the same trend until 1 mM. After this point, the $LiClO_4$ solution has a steep intensity drop at the lowest concentrations, whereas changing the cation to sodium results in a more gradual drop that eventually reaches a similar intensity to $LiClO_4$ at 1 M. $LiBF_4$ starts out with a steep drop, but at 10 mM starts to drop more gradually ending with an intensity far higher than the other salts at 1 M. The peak intensity of the $LiPF_6$ solution decreases slowly at concentrations $\leq 10^{-3}$ M, but suddenly drops to an intensity that is the lowest of all the salts. The biggest intensity difference among the electrolyte solutions is at 1 M, with the $LiBF_4$ intensity being approximately three times larger than the $LiClO_4$ intensity and the $NaClO_4$ and nine times larger than the $LiPF_6$ intensity.

Table 8.1. Concentration (c) regimes corresponding to different magnitudes and signs of r_I for $LiClO_4$, $NaClO_4$, $LiBF_4$, and $LiPF_6$.

Electrolyte	Very low concentration (negative r_I)	Low concentration (less negative or zero r_I)	Intermediate concentration (positive r_I)	High concentration (decreasing positive r_I)
$LiClO_4$	$c \leq 10^{-6}$ M	10^{-6} M < $c \leq 10^{-3}$ M	10^{-3} M< $c \leq 10^{-2}$ M	$c > 10^{-2}$ M
$NaClO_4$	$c \leq 10^{-6}$ M	10^{-6} M < $c \leq 1$ M	c >1 M	-
$LiBF_4$	$c \leq 10^{-6}$ M	$c > 10^{-6}$ M	-	-
$LiPF_6$	$c \leq 10^{-6}$ M	10^{-6} M < $c \leq 10^{-1}$ M	$c > 10^{-1}$ M	-

The full width at half maximum (FWHM) of the spectra for all of the salts, which are shown in Figure 8.7, is roughly constant until they reach 1 mM. $LiClO_4$ begins to broaden sharply at 10^{-3} M, and the FWHM begins to decrease at 500 mM and 1 M. The $NaClO_4$ spectrum is slower to broaden, but by 1 M the FWHM reaches its maximum for $LiClO_4$. The $LiBF_4$ spectra broaden more gradually, in a manner

similar to $NaClO_4$. The $LiPF_6$ spectra broaden only slightly at 10^{-2} M, and then sharply at 1 M.

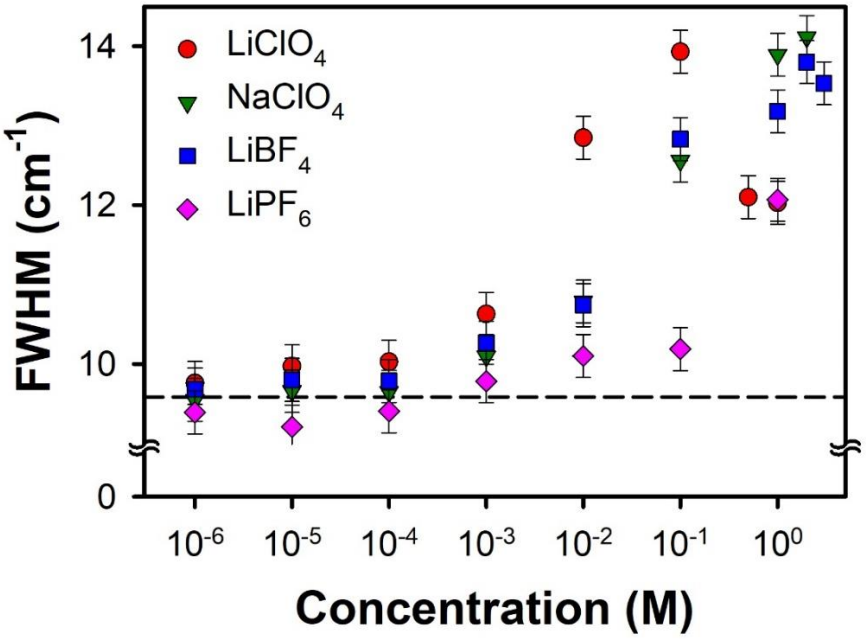

Figure 8.7. FWHM for VSFG spectra of four electrolyte solutions in acetonitrile. The black dashed line indicates the FWHM of neat acetonitrile. The FWHM does not change significantly when dry acetonitrile is exposed to ambient water.

Plotted in Figure 8.8 is the concentration dependence of the shift of the peak frequency of the VSFG spectra. There is a slight red shift for all salts with increasing concentration up to 10 μM, after which the peaks shift to the blue with increasing concentration. The peak frequency shifts similarly for all salts. However, there are some small differences among the salts. The $LiClO_4$ spectrum shifts more sharply than the spectra of the other salts at 10 mM and 100 mM. The $LiBF_4$ spectrum shifts the least. The spectrum for the $LiPF_6$ solution shifts slowly at first, and by 1 M acquires the greatest blue shift observed in this study.

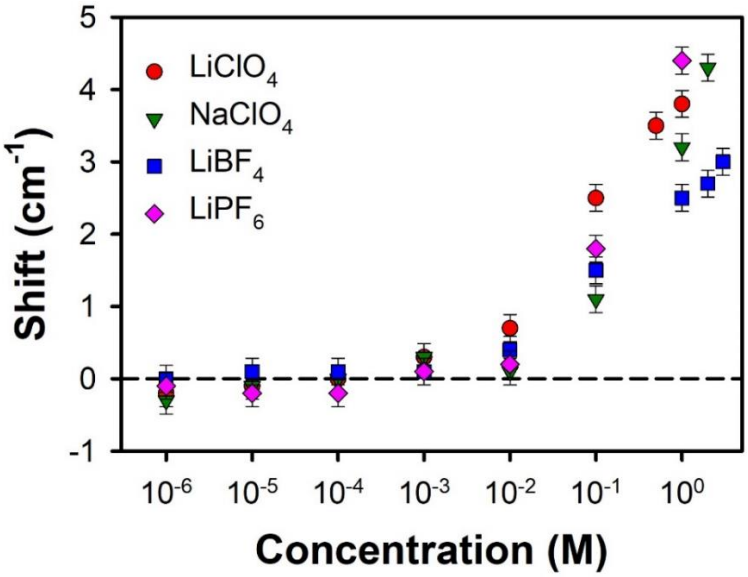

Figure 8.8. Shift in peak frequency for VSFG spectra of electrolyte solutions relative to neat acetonitrile. The peak frequency does not change significantly when dry acetonitrile is exposed to ambient water.

8.5 Discussion

8.5.1 Charge distribution at the acetonitrile/silica interface

The above observations are related intimately to the effective surface potential arising from the distribution of charges at the acetonitrile/silica interface. The unique charge distribution is not only responsible for the rectification behavior observed in the nanopore experiments, but also plays a role in the VSFG spectra. Because VSFG depends on the second-order nonlinear susceptibility ($\chi^{(2)}$), within the electric dipole approximation no VSFG signal is generated in an isotropic medium. This phenomenon is responsible for the interface sensitivity of VSFG spectroscopy. However, in the presence of a constant surface potential along the interface normal, a sum-frequency signal can also be generated by a $\chi^{(3)}$ process in both interfacial molecules and in the isotropic bulk liquid. The VSFG signal that arises from the $\chi^{(3)}$ contribution is limited to the region of the liquid in which the surface potential can be felt, but this region can

be substantially thicker than that probed by the $\chi^{(2)}$ process.[7-10] In aqueous solutions of monovalent electrolytes at low concentration, the range of the surface potential is generally assumed to be described by the linearized Poisson-Boltzmann equation.[11] It has been recognized recently that the exponential decay of the surface potential with distance from the surface leads to a complex interference between the $\chi^{(2)}$ and $\chi^{(3)}$ terms in the VSFG signal that is reflected in spectral properties that depend upon electrolyte concentration.[7, 12] Only when the electrolyte concentration is high enough does screening become efficient enough that only the $\chi^{(2)}$ contribution to the signal need be considered.

As discussed above, solid interfaces in solvents that are either protic or strong bases often become charged. In the case of an aprotic, weak base such as acetonitrile, the surface silanol groups of silica are expected to remain intact. At a silica interface, this liquid is also known to take on an organization that in some ways resembles that of a supported lipid bilayer.[13-16] Thus, the amphiphilic nature of acetonitrile is a stronger driving force for the organization of acetonitrile at this interface than are dipole-dipole interactions.

Hu and Weeks have previously reported an MD simulation of acetonitrile at a flat silica interface in which they calculated the average charge density $\rho^q(z)$, where z is the distance from the silica surface.[13] The silica surface used was fully hydroxylated, and only the surface silicon, oxygen, and hydrogen atoms were assigned partial charges. The average charge density of the acetonitrile is shown in Figure 8.9, with the charge density of the silica surface shown in the inset.

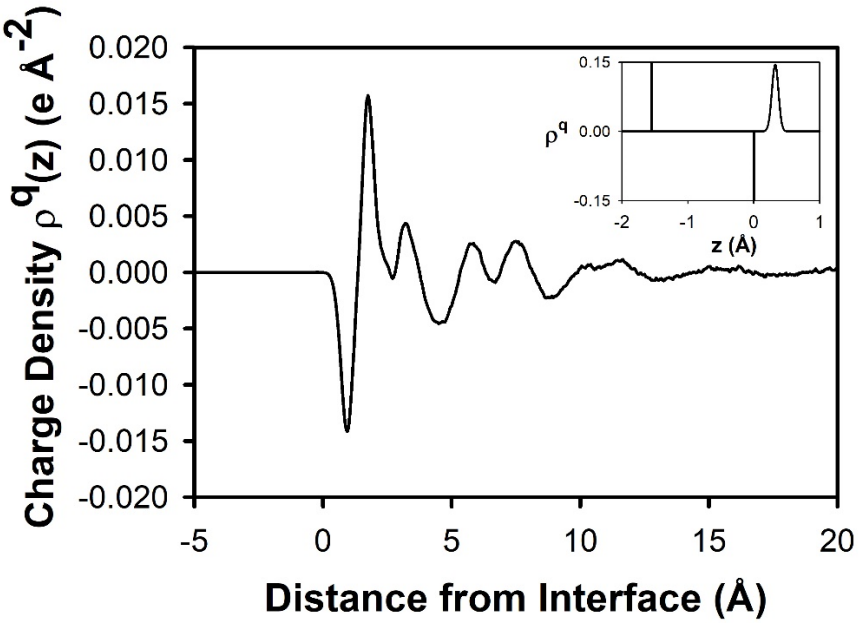

Figure 8.9. Acetonitrile charge density at a silica interface as calculated by Hu and Weeks in Reference 13. The charge density generated by the surface silicon, oxygen, and hydrogen atoms is shown in the inset. Within 1 Å of the silica surface the charge density is dominated by the partial charges on the surface atoms in the silica. Because the surface has no net charge, the charge density of the acetonitrile becomes more important at distances greater than 1 Å.[13]

The remarkable conclusion from Figure 8.9 is that for distances greater than approximately 1 Å from the surface, the distribution of charge present in the liquid itself begins to play an important role. The result is that the silica surface acts as a strong organizing force for the liquid, but the apparent surface charge is an intrinsic feature of the organized liquid rather than of the surface of the solid. This defining charge distribution can be related directly to the bilayer-like structuring in the acetonitrile at the interface. The hydrophobic regions, which are centered at approximately 2.6 Å from the surface for the first bilayer and 6.6 Å from the surface for the second bilayer, have a positive charge density from the central carbon atom in the cyano groups. The adjacent regions have negative partial charges that arise from the nitrogen atoms. It should be stressed that the charge density shown in Figure 8.9 is

for the neat liquid, and will be disrupted by the presence of ions. Nevertheless, examining the charge density of the neat liquid offers a means of developing a qualitative understanding of the results presented above.

8.5.2. Distribution of ions at the acetonitrile/silica interface

The cartoons in Figure 8.10 illustrate the partitioning of ions indicated by the VSFG spectra of $LiClO_4$ solutions. The unique organization at different electrolyte concentrations helps us to understand the ion current rectification results. The other electrolytes have related behavior and will be discussed further in Section 8.5.3. Figure 8.10A shows the bilayer structure before electrolytes are added. The cyano groups in the second sublayer, which generally point away from the interface, create an effective negative surface charge from the arrangement of negative partial charges.

Once ions are added to acetonitrile, it is important to consider the relative sizes of the species in the solution. The diameter of a lithium cation is 1.8 Å. These species are most likely to be found in regions of negative charge density, where it will associate with the nitrogen atoms of acetonitrile. The perchlorate anion, on the other hand, has a diameter of 4.5 Å, and its negative charge is highly delocalized. The most energetically favorable region for this species is likely to be in the hydrophobic regions of the bilayers. However, the size of the anions necessitates a substantial reorganization of the liquid in this region to accommodate an anion.

The bilayer structure at very low concentrations ($\leq 10^{-6}$ M) is depicted in Figure 8.10B for $LiClO_4$. The VSFG spectra show an intensity slightly higher than that of pure acetonitrile, and there is a small red shift of the spectrum. The cations cannot penetrate the surface bilayer (i.e., there is a substantial kinetic barrier), but rather sit just outside

of it. They are mobile, so at low concentrations the effective surface potential is still negative, albeit smaller than in the neat liquid, explaining the direction of ion current rectification at very low concentrations. In neat acetonitrile the second sublayer is more disordered with approximately 40% of the methyl groups pointing in the other direction.[13-14] The cations help to point the majority of the cyano groups in the second sublayer in the same direction. The greater alignment increases the contribution from the second sublayer to the VSFG signal. Because methyl groups in the second sublayer have a vibrational frequency red-shifted from that of the first sublayer, a greater contribution from this sublayer will cause a slight red shift and a slight increase in the overall intensity.

At concentrations between 10^{-6} M and 10^{-3} M (Figure 8.10C) more cations partition outside of the surface bilayer, increasing the order of the second sublayer. As a greater number of lithium ions interact with cyano groups, the vibrational frequency of the methyl group will blue shift slightly (which is analogous to the blue shift induced by cyano groups accepting hydrogen bonds). The increase in order and the blue shift lead to a modest decrease in overall peak intensity, but there is no overall peak shift or change in the FWHM yet. The higher concentration of cations will neutralize the apparent charge of the bilayer, and eventually there will be no observable rectification.

Once electrolyte solutions reach an intermediate concentration (between 10^{-3} M and 10^{-2} M), shown in Figure 8.10D, the negative apparent surface charge is neutralized. The second sublayer is less hindered than the first sublayer and can exchange with the bulk on a time scale of picoseconds,[17-18] so anions can begin to penetrate the bilayer. This insertion is expected to have three clear spectral effects.

First, the disorder associated with insertion should lead to a decrease in the VSFG signal. Second, insertion of the anions should increase inhomogeneous broadening, as different methyl groups will be in different environments. Third, the charge density in the hydrophobic region of the bilayer should go from a positive value to a substantially greater negative value arising from the anions, which should blue shift the spectrum. All three of these phenomena are indeed observed in the VSFG data.

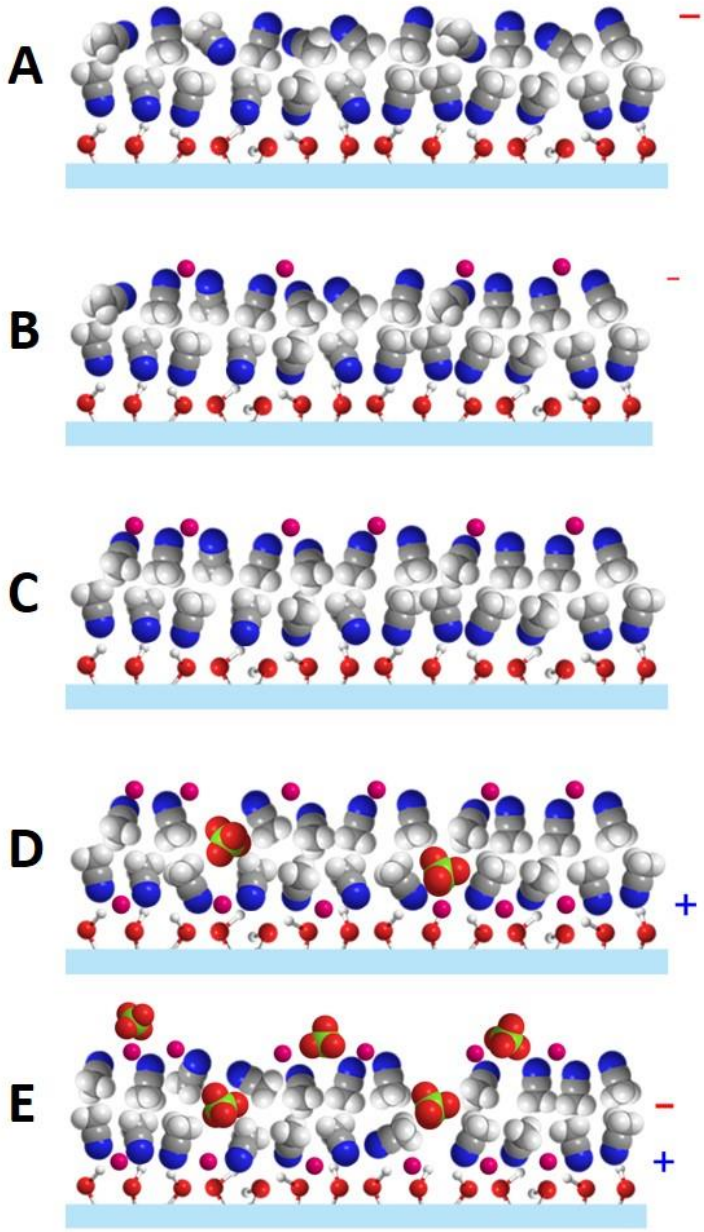

Figure 8.10. Cartoons of the organization of acetonitrile at the silica interface in different concentration regimes of lithium perchlorate: (A) neat acetonitrile (B) very low concentration ($\leq 10^{-6}$ M) (C) low concentration (10^{-6} M $\leq$ concentration $\leq 10^{-3}$ M) (D) intermediate concentration (10^{-3} M $\leq$ concentration $\leq 10^{-2}$ M) (E) high concentration ($\geq 10^{-2}$).

The anions create enough disorder that lithium cations can now partition easily to the silica surface, populating the silica surface in numbers much greater than the

population of anions in the bilayer (Figure 8.10D). Partitioning of cations to the surface causes a further decrease in VSFG intensity, which probably arises from a combination of disorder and the new DC electric field. The relative exclusion of anions from the interface at millimolar electrolyte concentrations naturally leads the interface to have a net positive charge. This phenomenon is responsible for the rectification seen in the nanopore experiments discussed above.

At high enough concentrations, the $LiClO_4$ solutions start to rectify to a lesser degree than at intermediate concentrations. Weaker rectification must be a result of a greater number of anions populating the interior of the bilayer, which is considerably patchier at this point (Figure 8.10E), and reducing the effective positive charge. The VSFG peak intensity continues to decrease and the peak frequency continues to shift, but the FWHM reaches a point where broadening reaches a maximum and starts to decrease. This decrease in inhomogeneity arises from the fact that most methyl groups now reside near an anion.

8.5.3. Explaining rectification with VSFG spectroscopy

Examining the VSFG spectra in more detail can help explain the differences in rectification between the different electrolyte solutions. The later and more gradual onset of rectification seen in $NaClO_4$ solutions compared to $LiClO_4$ can only be attributed to the different cation. Sodium ions must interact to a lesser extent with the cyano groups of the second sublayer. This weaker interaction can be attributed to the sodium ion's larger size and weaker polarizing power,[3] and is reflected in the VSFG spectra at both very low and low concentrations. At very low concentrations the intensities do not increase significantly, and at low concentrations they decrease more

gradually. A more gradual neutralization of the negative charge will delay the perchlorate ion's insertion into the bilayer, shown by the more gradual increase in FWHM. Because the larger sodium ions require greater disorder to get to the surface, the outcome is a positive current anisotropy onset at a much higher concentration than needed for $LiClO_4$ solutions.

For $LiBF_4$ the initial negative current anisotropy disappears at low concentrations, but unlike the other salts, there is never an inverse of rectification associated with a positive surface charge. This behavior is not entirely surprising given what is known about the properties of $LiBF_4$. This salt has a low conductivity and the lowest dissociation constant of all the lithium salts.[2] Based on vibrational spectroscopy and density functional theory studies, there is thought to be substantial ion pairing in this system.[6, 19] High concentrations of ion pairs will limit partitioning of the cation to the surface, which is consistent with the high intensities seen for all of the high concentrations of $LiBF_4$. The broadening of the spectrum follows a similar trend as the other salts which suggests that some ion pairs reside in the middle of the bilayer. However, the shift in peak frequency is less dramatic, which is likely because ion pairs do not interact as strongly with methyl groups within the bilayer or influence the electric field as would dissociated ions.

Initially, one of the most unexpected results was that the $LiPF_6$ solutions did not rectify at concentrations lower than the other electrolytes and, instead, did not begin to rectify until a bulk concentration of 100 mM. One would expect that the salt that had the bulkiest anion would have the greatest positive effective charge, if cations preferentially entered the bilayer and excluded the larger anion. If cations did partition

to the silica surface before the anion disrupted the bilayer, then no rectification would indicate that the anions followed the cations into the bilayer and neutralized their positive charge. But if this mechanism were operative, the VSFG spectra of $LiPF_6$ solutions would certainly exhibit an increase in FWHM at a lower concentration. The fact that neither rectification nor an increase in FWHM occurred implies that the cations are not getting to the silica surface at lower concentrations. This observation is further evidence that the anions must disrupt the bilayer before cations can populate the surface. Hexafluorophosphate ions are so large that they require both a high bulk concentration and a higher density of cations at the surface before they can penetrate the bilayer. When they do enter, they disrupt the bilayer substantially, creating the largest defects and allowing a higher relative concentration of cations to partition to the surface.

8.6 Conclusions

Debye-Hückel theory is often successful at describing the properties of low-concentration solutions of monovalent electrolytes. However, a key element of this theory is that the solvent can be treated as a featureless continuum. These results show that even for a liquid as "simple" as acetonitrile, surface-driven organization renders the assumption of a continuum solvent invalid. The behavior of solutions of electrolytes in acetonitrile at a silica surface is dominated by the organization imposed upon the liquid by the silica. The selective partitioning of cations to the surface at millimolar concentrations is driven by the lipid-bilayer-like organization of the interfacial liquid. Although the substantial diameter of the perchlorate and hexafluorophosphate anions is likely responsible for the high solubility of their associated salts in acetonitrile, the

size of these anions also causes them to be excluded from the highly organized liquid in the interfacial region. This same phenomenon is responsible for the apparent positive surface potential seen in glass nanopores in ion transport experiments with solutions of $LiClO_4$, $NaClO_4$, and $LiPF_6$ in acetonitrile.

Although the role of charged interfaces in VSFG spectroscopy has long been appreciated, our work brings to light a phenomenon that has not been considered previously, to our knowledge: liquid organization that is driven by proximity to an interface may lead to an intrinsic distribution of charge generated by the liquid that influences the distribution of ions and the resulting third-order contributions. This surface-associated charge distribution may be important at a broad range of interfaces, and should be considered in the interpretation of VSFG spectra.

8.7 References

1. Plett, T.; Shi, W. Q.; Zeng, Y. H.; Mann, W.; Vlassiouk, I.; Baker, L. A.; Siwy, Z. S., Rectification of nanopores in aprotic solvents - transport properties of nanopores with surface dipoles. *Nanoscale* **2015,** *7* (45), 19080-19091.

2. Xu, K., Nonaqueous liquid electrolytes for lithium-based rechargeable batteries. *Chem. Rev.* **2004,** *104* (10), 4303-4417.

3. Barthel, J.; Deser, R., FTIR study of ion solvation and ion-pair formation in alkaline and alkaline-earth metal salt solutions in acetonitrile *J. Solut. Chem.* **1994,** *23* (10), 1133-1146.

4. Eberspaecher, P.; Wismeth, E.; Buchner, R.; Barthel, J., Ion association of alkaline and alkaline-earth metal perchlorates in acetonitrile. *J. Mol. Liq.* **2006,** *129* (1-2), 3-12.

5. Barthel, J.; Buchner, R.; Wismeth, E., FTIR spectroscopy of ion solvation of $LiClO_4$ and LiSCN in acetonitrile, benzonitrile, and propylene carbonate. *J. Solut. Chem.* **2000,** *29* (10), 937-954.

6. Xuan, X. P.; Zhang, H. C.; Wang, J. J.; Wang, H. Q., Vibrational spectroscopic and density functional studies on ion solvation and association of lithium tetrafluorobrate in acetonitrile. *J Phys. Chem. A* **2004,** *108* (37), 7513-7521.

7. Gonella, G.; Lütgebaucks, C.; de Beer, A. G. F.; Roke, S., Second harmonic and sum-frequency generation from aqueous interfaces is modulated by interference. *J. Phys. Chem. C* **2016,** *120* (17), 9165-9173.

8. Wen, Y. C.; Zha, S.; Liu, X.; Yang, S. S.; Guo, P.; Shi, G. S.; Fang, H. P.; Shen, Y. R.; Tian, C. S., Unveiling microscopic structures of charged water interfaces by surface-specific vibrational spectroscopy. *Phys. Rev. Lett.* **2016,** *116* (1).

9. Pezzotti, S.; Galimberti, D. R.; Shen, Y. R.; Gaigeot, M. P., Structural definition of the BIL and DL: a new universal methodology to rationalize non-linear $\chi^{(2)}(\omega)$ SFG signals at charged interfaces, including $\chi^{(3)}(\omega)$ contributions. *Phys. Chem. Chem. Phys.* **2018,** *20* (7), 5190-5199.

10. Ohno, P. E.; Wang, H. F.; Geiger, F. M., Second-order spectral lineshapes from charged interfaces. *Nat. Commun.* **2017,** *8*.

11. Schoch, R. B.; Han, J.; Renaud, P., Transport phenomena in nanofluidics. *Rev. Mod. Phys.* **2008,** *80* (3), 839-883.

12. Schaefer, J.; Gonella, G.; Bonn, M.; Backus, E. H. G., Surface-specific vibrational spectroscopy of the water/silica interface: screening and interference. *Phys. Chem. Chem. Phys.* **2017,** *19* (25), 16875-16880.

13. Hu, Z.; Weeks, J. D., Acetonitrile on silica surfaces and at its liquid-vapor interface: structural correlations and collective dynamics. *J. Phys. Chem. C* **2010,** *114* (22), 10202-10211.

14. Ding, F.; Hu, Z.; Zhong, Q.; Manfred, K.; Gattass, R. R.; Brindza, M. R.; Fourkas, J. T.; Walker, R. A.; Weeks, J. D., Interfacial organization of acetonitrile: simulation and experiment. *J. Phys. Chem. C* **2010,** *114* (41), 17651-17659.

15. Cheng, L.; Morrone, J. A.; Berne, B. J., Structure and dynamics of acetonitrile confined in a silica nanopore. *J. Phys. Chem. C* **2012,** *116* (17), 9582-9593.

16. Mountain, R. D., Molecular dynamics simulation of water-acetonitrile mixtures in a silica slit. *J. Phys. Chem. C* **2013,** *117* (8), 3923-3929.

17. Loughnane, B. J.; Farrer, R. A.; Scodinu, A.; Fourkas, J. T., Dynamics of a wetting liquid in nanopores: An optical Kerr effect study of the dynamics of acetonitrile confined in sol-gel glasses. *J. Chem. Phys.* **1999,** *111* (11), 5116-5123.

18. Loughnane, B. J.; Farrer, R. A.; Fourkas, J. T., Evidence for the direct observation of molecular exchange of a liquid at the solid/liquid interface. *J. Phys. Chem. B* **1998,** *102* (28), 5409-5412.

19. Qiao, H. W.; Luan, H. L.; Fang, X. P.; Zhou, Z. M.; Yao, W.; Wang, X.; Li, J. M.; Chen, C.; Tian, Y., FT-Raman spectroscopic and density functional theory studies on ion preferential solvation and ion association of lithium tetrafluoroborate in 4-methoxymethyl ethylene carbonate-based mixed solvents. *J. Mol. Struct.* **2008,** *878* (1-3), 185-191.

Chapter 9: Conclusions

9.1 Conclusions and Future Work

Improving our knowledge of molecular organization and dynamics at liquid/solid (LS) interfaces is essential to understand the processes that take place at surfaces in countless applications. VSFG spectroscopy has allowed us to learn a vast amount of information, yet VSFG studies are dominated by analyses that assume a static structure and are based on the properties of individual molecules. I demonstrate in this thesis how VSFG spectra can be influenced by reorientational dynamics, intermolecular vibrational coupling, and local charge distributions. Importantly, these effects can occur in unexpected systems. The methyl symmetric stretch of acetonitrile is a largely isotropic mode with a relatively weak transition dipole moment. For these reasons, reorientation and intermolecular coupling would not be expected to be important. Additionally, the silica surface is not charged at the acetonitrile interface, so electric potentials may not seem to be a necessary consideration. Despite these properties of the acetonitrile LS system, the unexpected LBL organization of this interface induces effects that we may not expect otherwise.

In low viscosity liquids, molecules can reorient such that oscillators can enter a different dielectric environment on the time scale of the VSFG measurement. This change in environment induces a time dependence in the underlying vibrational response via the phenomenon known as RISD. I have presented the results of a sensitive, high-resolution, time-resolved VSFG study that has identified small wavenumber shifts at IR-probe delays out to 3.5 ps.[1] Delays of this magnitude are on

the same time scale as reorientation of the second, more dynamic, sublayer. After assessing the instrumental response and incorporating it into the fitting algorithm, spectral changes could not be reproduced with a static line shape.[1] The results of a temperature-dependent study were also consistent with the effects of RISD.[2] These results demonstrate the importance of including models for RISD for solvatochromic species in heterogeneous environments that reorient on a time scale comparable to the length of the probe pulse.

In this thesis, I also assess the influence of intermolecular vibrational coupling. Such coupling can be manifested as a shift in the first moment between the IR, isotropic Raman, and anisotropic spectra, an effect known as the Raman noncoincidence effect. I describe how these mechanisms rely on the appropriate relative alignment of oscillators. At an interface, molecules can have unique arrangements brought about by strong interactions with the surface. I discuss how this phenomenon can occur in systems with relatively small transition dipole moments, such as the symmetric methyl stretch of acetonitrile, if the distances between transition dipoles are small. Developing a method for interpreting the changes in spectra will have important implications for polarization analysis of modes that have significant anisotropic and isotropic components.

The surprising results of ion transport measurements motivated us to investigate electrolyte solutions in acetonitrile at the LS interface. The fascinating result was that VSFG spectra could not only predict rectification results, but also identify the underlying mechanism. I show how apparent positive charge at the surface of glass nanopores at millimolar concentrations arises from the preferential partitioning of

cations to the silica surface and the relative exclusion of anions. To explain the VSFG spectra, a model was used that included the influence of the intrinsic charge distribution from the organized acetonitrile molecules. The formation of regions of electric field from both ions and acetonitrile molecules influences the migration of ions as well as induces a $\chi^{(3)}$ response.

The studies described in this thesis are based on the response of the symmetric methyl stretch to various phenomena. This mode has a strong VSFG response, and pumping transitions in this spectral region is less challenging experimentally compared to regions in which atmospheric species absorb IR light. Moving forward, the next step would naturally be to examine the C≡N stretch of acetonitrile. The frequency of this mode is sensitive to its local environment, shifting 22 cm^{-1} when associated with a lithium ion[3] and 10 cm^{-1} upon forming a hydrogen bond with a silanol group.[4] Thus, the effects of RISD and interactions with ions would be expected to be more dramatic. The influence of the RNCE on this mode would also be interesting, as its stronger transition dipole could increase the magnitude of the effect, however, the different positions and configurations of the C≡N groups could change the magnitude and direction of the spectral shifts as well. MD simulations would of great value for any analysis performed on the C≡N stretch. There are a number of other species that would of interest in studying electrolyte solutions at solid interfaces. Propylene carbonate is a popular solvent in batteries and can be probed in the methyl stretch or carbonyl stretch region. Ions such as ClO_4^- can also be probed directly.

As the phenomena explored in this thesis are better understood, we can better quantify the influence of local electric fields and develop VSFG fully as a tool to

explore energy coupling and dynamical processes. Both the experimental approaches and theoretical methodology that I describe can be applied to a wide variety of systems.

9.2 References

1. Rivera, C. A.; Souna, A. J.; Bender, J. S.; Manfred, K.; Fourkas, J. T., Reorientation-induced spectral diffusion in vibrational sum-frequency-generation spectroscopy. *J. Phys. Chem. B* **2013,** *117* (49), 15875-85.

2. Souna, A. J.; Clark, T. L.; Fourkas, J. T., Effect of temperature on the organization of acetonitrile at the silica/liquid interface. *J. Phys. Chem. C* **2017,** *121* (47), 26432-26437.

3. Barthel, J.; Buchner, R.; Wismeth, E., FTIR spectroscopy of ion solvation of $LiClO_4$ and LiSCN in acetonitrile, benzonitrile, and propylene carbonate. *J. Solut. Chem.* **2000,** *29* (10), 937-954.

4. Kittaka, S.; Iwashita, T.; Serizawa, A.; Kranishi, M.; Takahara, S.; Kuroda, Y.; Mori, T.; Yamaguchi, T., Low temperature properties of acetonitrile confined in MCM-41. *J. Phys. Chem. B* **2005,** *109* (49), 23162-23169.

Bibliography

1. Rivera, C.A., **Souna, A.J.**, Bender, J.S., Manfred, K., Fourkas, J.T. Reorientation-Induced Spectral Diffusion in Vibrational Sum-Frequency-Generation Spectroscopy *J. Phys. Chem. B*, 2013, 117, 15875-15885.

2. **Souna, A.J.**, Bender, J.S., Fourkas, J.T. How Clean is the Clean Solvent You Use to Clean your Optics: A Vibrational Sum-Frequency Study? *Appl. Opt.*, 2017, 56(13), 3875-3878.

3. **Souna, A. J.**, Clark, T. L., Fourkas, J. T. The Effect of Temperature on the Organization of Acetonitrile at the Silica/Liquid Interface *J. Phys. Chem. C*, 2017, 121, 26432-26437.

4. **Souna, A. J.**, Rivera, C. A., Manfred, K. M., Fourkas, J. T. Intermolecular Vibrational Coupling in Liquid Acetonitrile at the Silica Interface *J. Chem. Phys.* (submitted for publication)

5. **Souna, A. J.**, Polster, J., Tran, J. D., Fourkas, J. T., Siwy, Z. (in preparation for publication)